October 2021

A Comprehensive Protocol for Inspection and Assessment of Aging Steel Bridges: Experiments, Computations and 3D Laser Scanning of Field Corroded Girders

Georgios Tzortzinis
University of Massachusetts Amherst

A Comprehensive Protocol for Inspection and Assessment of Aging Steel Bridges: Experiments, Computations and 3D Laser Scanning of Field Corroded Girders

Georgios Tzortzinis

A COMPREHENSIVE PROTOCOL FOR INSPECTION AND ASSESSMENT OF AGING STEEL BRIDGES: EXPERIMENTS, COMPUTATIONS AND 3D LASER SCANNING OF FIELD CORRODED GIRDERS

A Dissertation Presented

by

GEORGIOS TZORTZINIS

Submitted to the Graduate School of the
University of Massachusetts Amherst in partial fulfillment
of the requirements for the degree of

DOCTOR OF PHILOSOPHY

September 2021

Civil and Environmental Engineering

Structural Engineering & Mechanics

A COMPREHENSIVE PROTOCOL FOR INSPECTION AND ASSESSMENT OF AGING STEEL BRIDGES: EXPERIMENTS, COMPUTATIONS AND 3D LASER SCANNING OF FIELD CORRODED GIRDERS

A Dissertation Presented

by

GEORGIOS TZORTZINIS

Approved as to style and content by:

Simos Gerasimidis, Chair

Sergio F. Breña, Member

Sanjay R. Arwade, Member

Matthew A. Lackner, Member

Raimondo Betti, Member

John E. Tobiason, Department Head
Civil & Environmental Engineering

DEDICATION

To Georgios Zafeirakopoulos.

ABSTRACT

A COMPREHENSIVE PROTOCOL FOR INSPECTION AND ASSESSMENT OF AGING STEEL BRIDGES: EXPERIMENTS, COMPUTATIONS AND 3D LASER SCANNING OF FIELD CORRODED GIRDERS

SEPTEMBER 2021

GEORGIOS TZORTZINIS

DIPLOMA, UNIVERSITY OF PATRAS, GREECE

M.Sc., SWANSEA UNIVERSITY, UK

Ph.D., UNIVERSITY OF MASSACHUSETTS AMHERST

Directed by: Dr. Simos Gerasimidis

According to a recent evaluation, our nation's infrastructure has increasingly presenting signs of deterioration with some elements exhibiting significant deficiencies in conditions and functionality. Regarding the transportation network condition, from the over than 600,000 bridges which are included in the National Bridge Inventory, 46,154 of them are characterized as structurally deficient with the backlog of bridge rehabilitation needs estimated at US$125 billion. Among the many aspects of structural deficiency, corrosion is considered a common cause, both for reinforced concrete and steel bridge deterioration.

For steel bridges, corrosion has historically triggered bridge failures resulting to fatalities and injuries. To prevent similar incidents and to ensure public safety, authorities have established provisions dictating the mandatory inspection of bridges for deficiencies identification and maintenance. For girder bridges, supports constitute typical locations of corrosion induced damage due to water and occasionally deicing mixtures presence from the leaking bridge expansion joints. Depending on the severity of thickness loss, the load bearing capacity might be significantly reduced.

To address poor residual strength estimations both for rolled un-stiffened as well as plate girders, this dissertation develops tools towards a comprehensive inspection and assessment protocol. For remaining thickness quantification, 3D laser scanning is examined to tackle the shortcoming of conventional data acquisition techniques. The obtained point cloud data are post-processed to provide two-dimensional representations of the remaining section that can be integrated in inspection reports. The derived thickness contour maps can be employed both computationally and analytically for bearing capacity evaluation. Computationally, a methodology is developed to include the derived contour maps in finite element models. Analytically, simplified closed form equations are provided to describe the relation between thickness losses, beam geometry and the remaining bearing capacity. New findings are presented through a multi-step procedure including full scale experimental tests of field corroded girders, finite element modeling and sensitivity analyses to delve into the parameters that significantly affect the capacity of girders with end damage. Finally, analytical tools are developed based on the output of numerous simulated scenarios. The developed procedures are validated both experimentally and computationally providing overall improved estimations compared with the current policies.

PREFACE

Published Content:

Part I has been partially adapted from [1, 2]:

1. **Tzortzinis, G.**, Knickle, B.T, Bardow, A., Breña, S.F., Gerasimidis, S. (2021), Strength evaluation of deteriorated girder ends. I: Experimental study on naturally corroded I-beams, *Thin-Walled Structures*, 159: 107220.
   Author's contributions: Participated in experiments, analyzed data, wrote manuscript.

2. **Tzortzinis, G.**, Knickle, B.T, Bardow, A., Breña, S.F., Gerasimidis, S. (2021), Strength evaluation of deteriorated girder ends. II: Numerical study on corroded I-beams, *Thin-Walled Structures*, 159: 107216.
   Author's contributions: Performed finite element simulations, developed methodology, derived analytical formulas, analyzed data, wrote manuscript.

Part II has been partially adapted from [3]:

3. **Tzortzinis, G.**, Chengbo, A., Breña, S.F., Gerasimidis, S., Using 3D laser scanning for estimating the capacity of corroded steel bridge girders: Experiments, computations and analytical solutions, *Under review*
   Author's contributions: Participated in scans, analyzed data, developed methodology, performed finite element simulations, wrote manuscript.

Part III has been partially adapted from [4]:

3. **Tzortzinis, G.**, Breña, S.F., Gerasimidis, S., Experimental Testing, Computational Analysis and Analytical Formulation for the Remaining Capacity Assessment of Bridge Plate Girders with Naturally Corroded Ends, *Under review*
   Author's contributions: Participated in scans, analyzed data, developed methodology, performed finite element simulations, derived analytical formulas, wrote manuscript.

TABLE OF CONTENTS

LIST OF TABLES

LIST OF FIGURES

CHAPTER 1

INTRODUCTION

1.1 Opening Remarks

1.1.1 Bridge Failures Related to the Corrosion Phenomenon

The influencing effect of corrosion to the structural integrity of bridges was brought to the spotlight back in late 1960's due to the collapse of an eyebar chain suspension bridge. The Point Pleasant (Silver) Bridge, crossing the Ohio River, was in service for 36 years when it suddenly collapsed in the afternoon of December 15, 1967 causing the death of 46 people [9]. Investigations lasting almost four years revealed that the bridge failure was triggered from the brittle fracture of a single corroded eyebar.

Almost two decades later, on June 28, 1983 three people perished at the collapse of the Miamus River Bridge in the state of Connecticut. An approximately 30 m long span fell 20 m into the river due to the failure of a pin and hanger assembly. Corrosion-induced forces resulted to misalignment of the pin, increasing the developed stresses, which ultimately resulted to a crack generation and failure. According to the National Transportation Safety Board (NTSB) [10] this incident highlighted the deficiencies of the state's bridge inspection and maintenance program.

Corrosion related bridge failures have been also reported in Japan. In a research work, Ahn et al. [11] documented two bridge failures related to severe corrosion and fatigue problems. The first case describes a plate girder structure that collapsed in 2009, after 28 years of usage. Photographs capturing the damaged girders, taken after the incident occurred, depict significant section loss close to the support. The second documented collapse happened two years earlier, when a 57 years old bridge failed due to the severely deteriorated truss girders of the superstructure.

1.1.2 The Corrosion Phenomenon in Steel Bridges

The previously reported failures involved four different bridge types; an eyebar suspension bridge, a truss bridge, and two different configurations of plate girder bridges (simply supported, and with pin-hanger assembly). Even though corrosion constitutes their common characteristic, it is a complex phenomenon that appears in many forms. These forms are classified according to how the corrosion attacks metal, while an extensive description of the different types can be found in [12]. According to the same source, for steel bridges the following corrosion forms are usually found in the field:

Uniform corrosion constitutes a common form of deterioration. It is usually found along the entire or a large exposed steel surface. It is a natural process proceeding at the same rate across the damaged domain.

Crevice corrosion is the dominant corrosion form found on steel bridges. It occurs locally within gaps that can collect water, and is caused by the different environmental conditions inside and outside of the crevice, such as concentrations of ion metal cells. Crevice corrosion can be found between openings of built-up members, eyebars or even different materials such as timber and steel.

Deposit attack on bridges is a localized phenomenon that usually occurs at locations of debris deposits which harbor moisture. Grain and coal can be typical sources of debris in farm and mining areas, respectively. On the other hand, bird nests and bird excrement is a common source of acid that damages both the coating and the steel members.

Pitting corrosion is another form of localized corrosion and is attributed to chemical or physical changes in the metal, such as depositions. Morphologically, it causes deep penetrations into the steel surface and it can bee identified with the naked eye.

Stress corrosion cracking is reported for bridges located in marine or industrial areas, and occurs from the combination of tensile stresses and corrosive environment. Corrosion induced discontinuities result to stress rise leading to cracks initiation. It is worth noting that this type of deterioration results to a brittle failure even when it appears to ductile metals. In contract to the previously presented corrosion forms, stress corrosion cracking is not identified with visual observation and requires microscopic inspection.

For stringer span bridges, which constitute the bridge type that will be thoroughly investigated in the current thesis, different forms of corrosion may occur [5]. The interface between concrete deck and the top flange is a prevalent location for crevice corrosion, due to cracks allowing water to flow to the girder. The bottom flanges are vulnerable to debris accumulation and birds excrement, while the whole girder is subjected to uniform corrosion due to water spray from passing vehicles, Fig.1.1.

1.1.3 Bridge Inspection

The Silver Bridge collapse in 1967 triggered nation's reaction, and by 1971 the National Bridge Inspection Standards (NBIS) had been established. These provisions introduced the mandatory inspection of bridges to ensure public safety by identifying and maintaining deficiencies. Except for in-situ condition evaluation, the functions of bridge inspection include to report and evaluate the inspection results, as well as to maintain an inventory database.

Today, in the state of Massachusetts, the Massachusetts Department of Transportation (MassDOT) is responsible for maintaining the inventory of all bridges within the commonwealth. For this purpose, the MassDOT Bridge Inspection Handbook [13] has been introduced, to meet and in many cases exceed the NBIS Standards. According to [13], the following inspection types are used for bridge condition evaluation

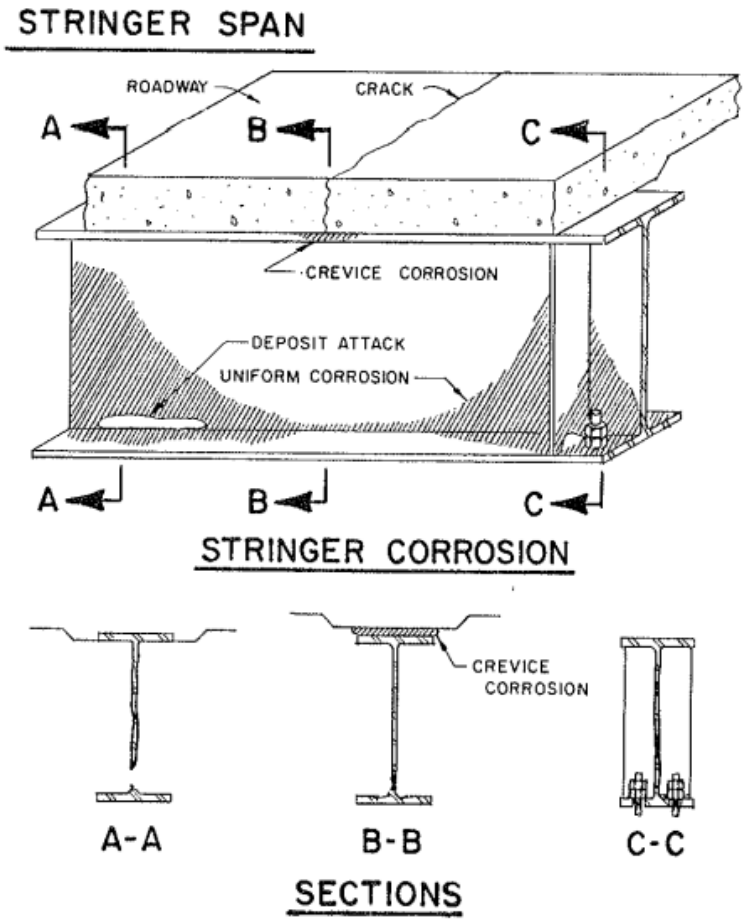

Figure 1.1: Locations and types of corrosion on girder bridges, [5].

and their frequencies are defined as follows:

Routine Inspections are "hands-on" and "in-depth" examination of the bridge which require the inspectors to be at arm's length from the structural member being inspected. Beyond visual observation, measurements are also required to determine the bridge condition. These types of inspections are performed at intervals not to exceed twenty-four months.

Fracture Critical inspections include the "hands-on" inspection of all members of a bridge that have been evaluated to be fracture critical. They usually take place at the same time with *Routine Inspections* unless reduced frequency is required.

Underwater Inspections focus on the underwater portions of bridge structures and the surrounding channel, when the depth of water exceeds three feet. *Underwater Inspections* are to be performed at regular intervals (generally 36 months), but not to exceed 60 months.

Special Member Inspections are performed on bridges that at least one of the main components (deck, superstructure or substructure) is being characterised in poor or worst condition. This type of inspection is performed on the particular elements (e.g. a girder) that are responsible for the poor condition rating of the overall item (e.g. superstructure).

All the findings from the conducted inspections are summarized in standard inspection report forms. In [13] sixteen different forms are used to provide a uniform method for querying information relevant to elements and sub-elements of a bridge. Fig. 1.2 presents the way that routine reports summarize the overall structural condition of the deck (item 58), the superstructure (item 59), the substructure (item 60) and their components. A similar format is used to evaluate the condition of the channel (item 61) as well as the traffic safety (item 36). The assigned condition rating is in the range of 0 to 9 encapsulating the severity of the observed deficiencies.

A detailed description of notable remarks then follows. This description is usually is combined with sketches or tables, demonstrating the position and the geometry of the damage. In most cases, the reports also include drawing, sketches, and plans which describe the geometry of the structure. Finally, if available, a series of photographs taken during the inspection are included at the end of the report. Fig. 1.3 presents a representative documentation way of a corroded beam end, with a sketch and a photograph.

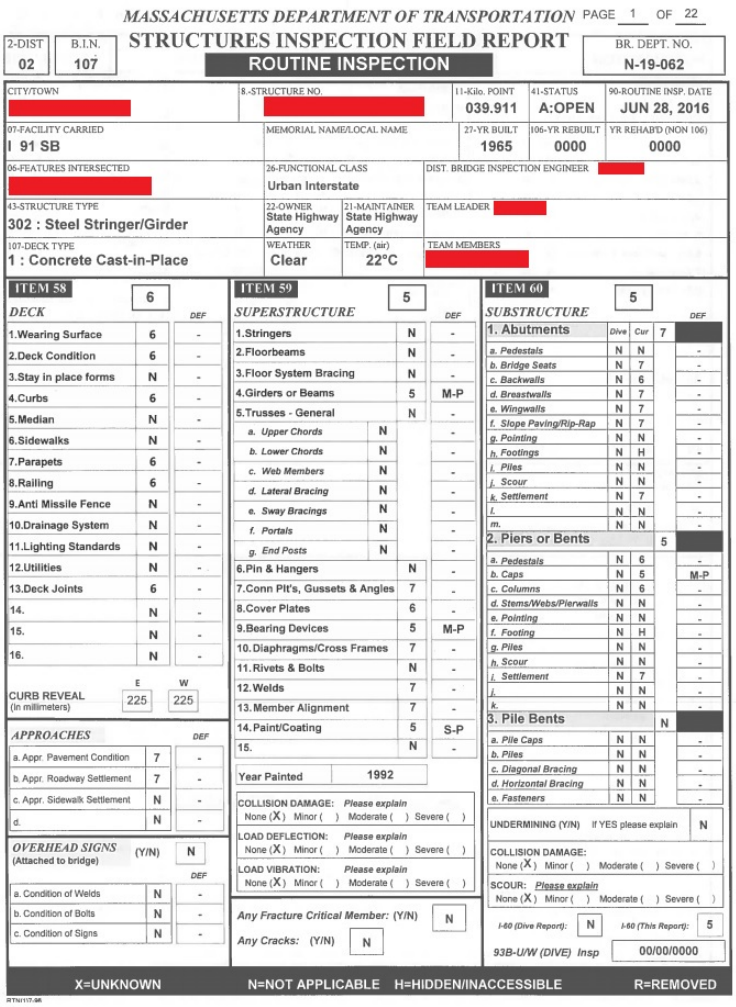

MASSACHUSETTS DEPARTMENT OF TRANSPORTATION PAGE 1 OF 22

STRUCTURES INSPECTION FIELD REPORT

ROUTINE INSPECTION

2-DIST	B.I.N.	BR. DEPT. NO.
02	107	N-19-062

CITY/TOWN	8.-STRUCTURE NO.	11-Kilo. POINT	41-STATUS	90-ROUTINE INSP. DATE
[redacted]	[redacted]	039.911	A:OPEN	JUN 28, 2016

07-FACILITY CARRIED	MEMORIAL NAME/LOCAL NAME	27-YR BUILT	106-YR REBUILT	YR REHABD (NON 106)
I 91 SB		1965	0000	0000

06-FEATURES INTERSECTED	26-FUNCTIONAL CLASS	DIST. BRIDGE INSPECTION ENGINEER
[redacted]	Urban Interstate	[redacted]

43-STRUCTURE TYPE	22-OWNER	21-MAINTAINER	TEAM LEADER
302 : Steel Stringer/Girder	State Highway Agency	State Highway Agency	[redacted]

107-DECK TYPE	WEATHER	TEMP. (air)	TEAM MEMBERS
1 : Concrete Cast-in-Place	Clear	22°C	[redacted]

ITEM 58 — DECK 6

		DEF
1.Wearing Surface	6	-
2.Deck Condition	6	-
3.Stay in place forms	N	-
4.Curbs	6	-
5.Median	N	-
6.Sidewalks	N	-
7.Parapets	6	-
8.Railing	6	-
9.Anti Missile Fence	N	-
10.Drainage System	N	-
11.Lighting Standards	N	-
12.Utilities	N	-
13.Deck Joints	6	-
14.	N	-
15.	N	-
16.	N	-

CURB REVEAL (in millimeters)	E	W
	225	225

APPROACHES

		DEF
a. Appr. Pavement Condition	7	-
b. Appr. Roadway Settlement	7	-
c. Appr. Sidewalk Settlement	N	-
d.	N	-

OVERHEAD SIGNS (Attached to bridge) (Y/N) N

		DEF
a. Condition of Welds	N	-
b. Condition of Bolts	N	-
c. Condition of Signs	N	-

ITEM 59 — SUPERSTRUCTURE 5

		DEF
1.Stringers	N	-
2.Floorbeams	N	-
3.Floor System Bracing	N	-
4.Girders or Beams	5	M-P
5.Trusses - General	N	-
a. Upper Chords	N	-
b. Lower Chords	N	-
c. Web Members	N	-
d. Lateral Bracing	N	-
e. Sway Bracings	N	-
f. Portals	N	-
g. End Posts	N	-
6.Pin & Hangers	N	-
7.Conn Plt's, Gussets & Angles	7	-
8.Cover Plates	6	-
9.Bearing Devices	5	M-P
10.Diaphragms/Cross Frames	7	-
11.Rivets & Bolts	N	-
12.Welds	7	-
13.Member Alignment	7	-
14.Paint/Coating	5	S-P
15.	N	-

Year Painted 1992

COLLISION DAMAGE: Please explain
None (X) Minor ( ) Moderate ( ) Severe ( )

LOAD DEFLECTION: Please explain
None (X) Minor ( ) Moderate ( ) Severe ( )

LOAD VIBRATION: Please explain
None (X) Minor ( ) Moderate ( ) Severe ( )

Any Fracture Critical Member: (Y/N) N

Any Cracks: (Y/N) N

ITEM 60 — SUBSTRUCTURE 5

	Dive	Cur		DEF
1. Abutments			7	
a. Pedestals	N	N		-
b. Bridge Seats	N	7		-
c. Backwalls	N	6		-
d. Breastwalls	N	7		-
e. Wingwalls	N	7		-
f. Slope Paving/Rip-Rap	N	7		-
g. Pointing	N	N		-
h. Footings	N	H		-
i. Piles	N	N		-
j. Scour	N	N		-
k. Settlement	N	7		-
l.	N	N		-
m.	N	N		-
2. Piers or Bents			5	
a. Pedestals	N	6		-
b. Caps	N	5		M-P
c. Columns	N	6		-
d. Stems/Webs/Pierwalls	N	N		-
e. Pointing	N	N		-
f. Footing	N	H		-
g. Piles	N	N		-
h. Scour	N	N		-
i. Settlement	N	7		-
j.	N	N		-
k.	N	N		-
3. Pile Bents			N	
a. Pile Caps	N	N		-
b. Piles	N	N		-
c. Diagonal Bracing	N	N		-
d. Horizontal Bracing	N	N		-
e. Fasteners	N	N		-

UNDERMINING (Y/N) If YES please explain N

COLLISION DAMAGE:
None (X) Minor ( ) Moderate ( ) Severe ( )

SCOUR: Please explain
None (X) Minor ( ) Moderate ( ) Severe ( )

I-60 (Dive Report): N I-60 (This Report): 5

93B-U/W (DIVE) Insp 00/00/0000

X=UNKNOWN N=NOT APPLICABLE H=HIDDEN/INACCESSIBLE R=REMOVED

Figure 1.2: First page of a typical Routine Inspection Report.

1.1.4 Load Rating of Bridges

According to the MassDOT Bridge Inspection Handbook [13] the live-load carrying capacity of existing bridges should be evaluated on a decade-basis unless concern occurs due to the critical condition of an asset. In that case, the inspectors can warrant a load rating request. Load ratings evaluate a series of "points of interests" along the girders and are conducted based on the plans, as built conditions and the latest bridge inspection reports.

(a) (b)

Figure 1.3: The same beam, as was described by a) sketch and by b) photograph.

Taken all together, to efficiently calculate the residual load carrying capacity of deteriorated bridges a three-steps process is required: a) deficiencies inspection, b) documentation of the findings, and c) load rating procedures. Along this procedure not only the efficiency of each is step is vital, but also the data exchange from each step to the adjacent one.

1.2 Scope and Outline of the Thesis

According to a recently published ASCE report [14], 42% of the nation's highway bridges are at least 50 years old, emphasizing the need of a systematic program for bridge preservation. According to the same source, many states have started prioritizing the preservation of decaying bridges over building new structures, by redirecting resources to the development of novel inspection, evaluation and repair techniques. For steel viaducts and bridges, aging is mainly caused by corrosion along the superstructure components, constituting one of the main causes for structural deficiency. Corrosion is primarily induced by chloride-laden water that seeps through malfunctioning deck expansion joints.

Joints are ranked as one of the most vulnerable bridge components, mainly be-

cause they are exposed to impact loads by passing vehicles as well as to environmental factors. Typically, steel bridge girder type configurations include expansion joints located above the bearings, allowing water leakage and deicing chemicals to contaminate the steel load bearing surfaces, resulting in section loss. Depending on the severity of thickness loss in the end region of steel beams, the load bearing capacity might be significantly reduced. In order to ensure public safety but at the same time avoiding posting bridges, efficient tools for capacity evaluation are required.

To efficiently calculate the residual capacity of girders with beam end corrosion, the previously mentioned three-steps process is specified as the sequence of the following actions, requiring the collaboration of people with diverse background and expertise. The first step takes place in the field, where inspectors acquire thickness measurement representative of the girders condition. The obtained measurements are later on summarized in inspection reports to provide the essential information to load rating engineers, who will use closed form equations to determine the vehicle classes allowed to cross the viaduct.

This thesis aims to facilitate and improve the three-steps process for simple span bridges with deteriorated girders ends, towards a comprehensive protocol of corrosion detection, mapping and capacity evaluation. The first part of the dissertation provides analytical tools for the remaining capacity estimation of rolled un-stiffened girders with corroded ends, and it has both experimental and computational aspects [1–3, 15, 16].

The second part focused on corrosion data acquisition and documentation making use of 3D laser scanning technology. Contour maps depicting the remaining web thickness are developed by post-processing the point cloud data. In addition, the 3D scanning data are combined through an automated procedure with finite element analysis as well as with analytical provisions to examine whether 3D scanning can

inform these two tools reasonably for accurate capacity predictions. The results provide a good agreement between experimental and predicted failure loads, paving the way for a more efficient, safe and time-saving inspection protocol.

Finally, at the third and last part of this thesis methodologies and knowledge developed at the aforementioned parts are combined to develop analytical tools for the capacity assessment of plate girders. It is worth noting that every aspect of this thesis is derived and validated on real corrosion data. For the first time, full scale laboratory testing of eight naturally corroded specimens retrieved from bridge rehabilitation projects of highway bridges, has been conducted.

PART I:

CAPACITY EVALUATION OF ROLLED GIRDERS WITH CORRODED ENDS

CHAPTER 2

LITERATURE REVIEW AND OBJECTIVES

2.1 Literature Review

One of the pioneering studies on girder capacity under patch loading was by Roberts [17], who proposed the plastic hinge failure mechanism. Kayser et al. [18] conducted one of the earliest efforts to extend the area of investigation to deteriorated bridges, by studying the effect of thickness loss to bearing capacity. Van de Lindt and Ahlborn [19] developed guidelines for deteriorated steel beam ends. Initially, damage simulations of various sizes and shapes were performed using the finite element method. Experimental work was conducted on 1 m long beam segments, with artificial web and flange thickness reduction above the bearing, validating also the FEM model. Ultimately, a deterioration factor was proposed as a simplified approach for calculating capacity reduction estimation. Design charts were introduced for the deterioration factor calculation for given damage heights, and three options of thickness losses, for one as well as two sides of web corrosion.

Beam end corrosion is an issue that has received a lot of research attention in eastern Asia, with experimental work conducted and reported from Japan and Korea. Sugimoto et al. [20] tested an actual railway deck plate girder constructed in the beginning of the twentieth century, and proposed a method for capacity reduction assessment for bending and shear failure at midspan and support area respectively.

A few computational efforts have been reported to investigate the role of corrosion to un-stiffened girders. Except for the work of Van de Lindt and Ahlborn [19] which had both experimetnal and computational aspects, Tohidi and Sharifi [21] proposed an empirical equation based on Back - Propagation Neural Network (BPNN) to predict

the residual bearing capacity of damaged beams.

There is also a wide range of repair techniques studied for corrosion-damaged girders presented in the literature. Ahn et al. [22] proposed CFRP usage due to its low weight, high strength, and its rapid and simple application. Miyashita et al. [23], using the same repair method, conducted experimental and numerical shear buckling tests on an intact, a damaged and a repaired specimen, reporting, for the case of the repaired end, recovery of load carrying capacity to the level of the intact beam. Ogami et al. [24] attached studs and rebar to the corroded girder before covering it with resin. With the proposed technique, buckling was prevented under axial compressive loading. Wu et al. [25], experimentally highlighted the impact of web section loss within the flange diffusion range for un-stiffened I-beams, while in a second study [26] specimens were strengthened by welding stiffeners on the two sides of the web and partially encasing it with high-strength grout. It was found that the patch loading resistance is restored by welding the stiffeners, and can be further improved by the encasement of high-strength grout.

Research conducted at the University of Connecticut, where another repair strategy was proposed by Zmetra et al. [27], is also worth noting. The researchers welded shear studs to the web and encased the end region of the girder in ultrahigh-performance concrete (UHPC). One third scale experiments revealed that the proposed technique managed to restore the capacity of the deteriorated girder by transferring shear and bearing forces from the girder to the UHPC panels. A series of push-out experiments was also performed to evaluate the capacity of studs embedded in UHPC [28, 29]. Finally, in order to check the durability of the proposed technique, push-out tests were performed on specimens subjected to accelerated electrochemical corrosion [30]. The mechanical performance of the headed studs was not affected by corrosion. This may be because the applied corrosion protocol prevented the pene-

tration of electrolytic solution to the base of the headed studs, consequently limiting the impressed imposed corrosion.

Researchers have approached beam end corrosion from multiple aspects, from the residual bearing capacity evaluation to innovative repair techniques. Except for the work of Sugimoto et al. [20] on railway bridges, all other efforts have artificially introduced corrosion as uniform thickness reduction on intact beams. It is quite challenging to gain access to naturally corroded beams for testing. In the real conditions of the field however, the deterioration phenomenon is non uniform, it varies significantly in topology and intensity and it is highly related to the configuration of the bearing area. Parameters like the age of the bridge, the exposure conditions, the type of bearing, the existence of a diaphragm as well as the position of the leaking deck joints directly affect the water flow resulting in a multi-variable parametric space. Thus, simulating corrosion as uniformly reduced thickness, potentially renders results that could be not realistic.

2.2 Objectives and Outline

The first part of this thesis ultimately provides a tool for bearing capacity assessment of simple span girders with un-stiffened ends. Its methodology is distinguished from other research efforts in the aspect that it emerges from real deterioration data. Full scale laboratory bending tests on six naturally corroded specimens obtained from bridge demolition projects across the state of Massachusetts are conducted. Chapter 3 details the beam selection process, the experimental and instrumentation configuration, as well as the detailed descriptions of each specimen. The measured data along with the failure modes and mechanisms are presented. Finally, the procedures currently in use are evaluated based on the experimentally obtained capacity measurements. The outcome of the conducted experiments, constitutes the base of the

computational aspect towards the improvement of current procedures that follows in Chapter 4.

In Chapter 4 the experimental data of two girders are implemented to calibrate and validate a girder-level numerical model developed to simulate the testing configuration. Subsequently, the numerical study is extended to a series of simulations conducted to investigate the performance of varying girder types under numerous geometry and corrosion scenarios.

In Chapter 5, relationships are developed for exterior pier bearing capacity estimation of corroded girders. The provided equations cover a wide range of initial web out-of-plane deviation amplitudes, capturing the variability of web condition measured on the tested specimens. The proposed provisions are based on modifications to the current methodology used by MassDOT, and are designed to capture two types of failures (buckling and crippling) creating an envelope of the computationally obtained capacities of more than 2000 scenarios. The simulated scenarios cover the whole range of simplified orthogonal shaped patterns that were identified as critical from data obtained by inspection reports in the state of Massachusetts.

CHAPTER 3

EXPERIMENTAL EVALUATION OF NATURALLY CORRODED I-GIRDERS

3.1 Experiment Design

3.1.1 Description of Corroded Specimens

Corroded beams were acquired from two steel bridges built in 1939 in the western part of the state. The bridge from site A, referred as Bridge A in this thesis, was a five span bridge which contained 33WF132 exterior and 33WF125 interior simply supported un-stiffened rolled girders for the two outer spans, spanning 15.2 m , Fig. 3.1a. A total of 8 beams were selected from Bridge A and transported for testing in the Brack Structural Testing Laboratory at the University of Massachusetts Amherst (UMass). For transportation purposes, the beams were cut in half at the site, in order to fit within the limitations of the testing facility. The bridge from site B, referred as Bridge B in this thesis, was a simple span integral abutment bridge consisting of 6 rolled 21WF59 and 21WF73 beams spanning approximately 6.1 m , Fig. 3.1b. All of the beams were sent to the testing laboratory at UMass.

The eight girders from Bridge A had only one corroded end corresponding to the end under an expansion joint. Consequently, out of the 16 acquired segments, only 8 were considered for testing. This inventory was further reduced to 3 beams, numbered as Specimens 1 to 3, due to the extensive damage and deformations of the flange of the corroded end of several beams, probably caused during removal of beams from the bridge. Regarding the 6 girders obtained from Bridge B, three of them had extensive corrosion at midspan, and their condition would likely result in flexural failure prior

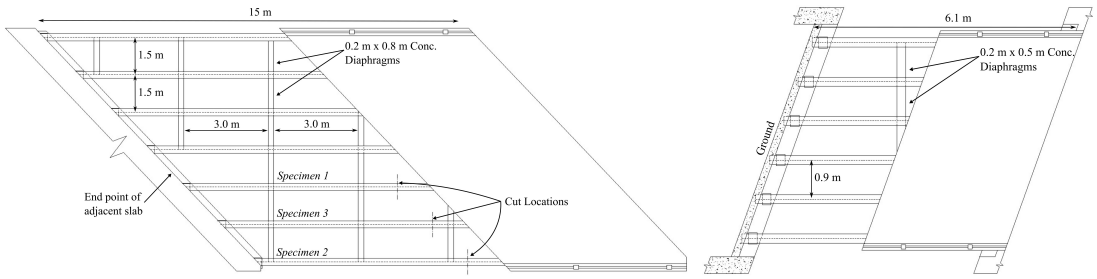

Figure 3.1: Plane view of (a) the outer span of Bridge A and (b) Bridge B.

to shear (or bearing) failure at the end. The remaining three beams were numbered as Specimens 4 to 6, and there were tested in the framework of the current thesis.

3.1.2 Specimen Geometry

While in service, the ends of the beams corresponding to Specimens 1 through 3 were embedded within a concrete diaphragm occupying approximately the top half of the beam depth, Fig. 3.2. During the bridge demolition, the concrete diaphragm was removed revealing three holes at each beam end that were drilled through the beam web to pass reinforcement within the diaphragm. The technique, of creating holes on-site to pass reinforcement within the end diaphragm for continuity, is commonly found in construction drawings of that period. Portions of steel angles used to support the diaphragm remained bolted at web mid-height. The beams were delivered to UMass with the bearing plates still welded to the beam ends. In some cases, anchors protruding from the bottom of the bearings had to be sawn off. Finally a common characteristic of all specimens obtained from Bridge A is that the top portion of the web was cut at an angle to accommodate the bridge geometry (Figs. 3.3-3.4).

Specimen 1 is a 843 cm long 33WF125 (Table 3.1) with extensive end corrosion (Fig. 3.3). The most severe section loss is noticed in the lower half of the web, with two distinct observed holes caused by corrosion. The first hole has an almost circular

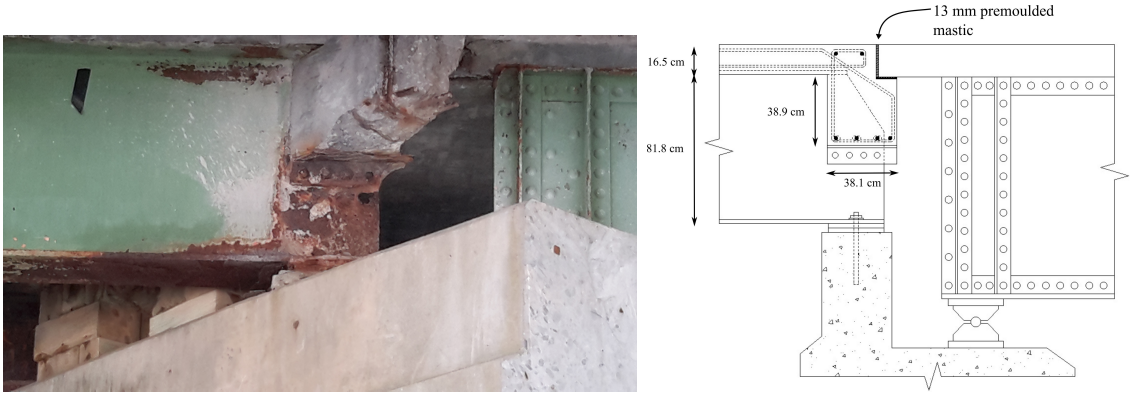

(a) (b)

Figure 3.2: (a) Typical, in service, configuration and (b) construction details for Bridge A (Specimens 1 to 3)

Table 3.1: Nominal dimensions of the tested specimens.

Beam Type	Depth d mm	Web Thick. t_{web} mm	Flange Width b_f mm	Flange Thick. t_f mm	Fillet Radius R mm
33WF125	838.2	14.5	292.1	20.4	17.8
33WF132	842.0	14.7	292.4	24.9	17.8
21WF73	539.5	11.6	210.7	18.8	12.7
21WF59	531.1	9.9	209.0	14.6	12.7

shape of 76 mm diameter and is located approximately at beam mid-depth below the remaining steel section angles (Fig. 3.3a). A second corrosion-induced hole formed longitudinally directly above the bottom flange with dimensions of 152 mm long x 13 mm high. At the inner edge of the second hole, the web had crippled for a distance of 76 mm along the longitudinal axis of the beam. Finally, the maximum out of plane web deviation from the vertical plane was 14 mm.

Specimen 2 is a 728 cm long 33WF132 beam (Table 3.1). Three different areas with extensive thickness reduction were observed above the support. The first distinct area is located parallel to the inner edge of the concrete diaphragm (Fig. 3.3b). The shape and the location of this corroded area is in agreement with inspectors witnesses

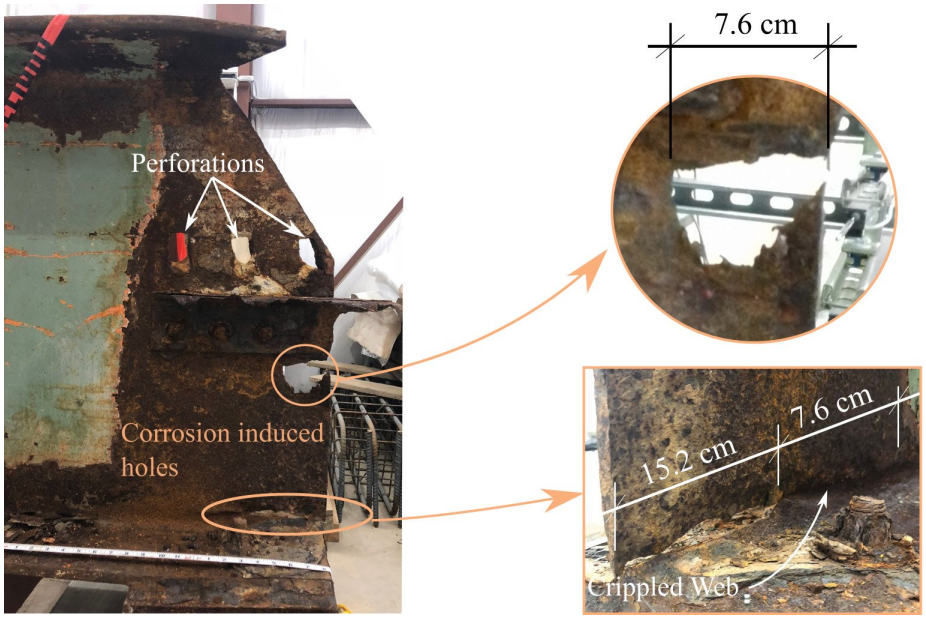

(a)

(b)

Figure 3.3: Corrosion characteristics of Specimens (a) 1, and (b) 2. Both girders are 84 cm deep obtained from Bridge A. Their defining feature is a corrosion-induced hole formed longitudinally at the base of the web, and the initial web deviation from straightness, respectively.

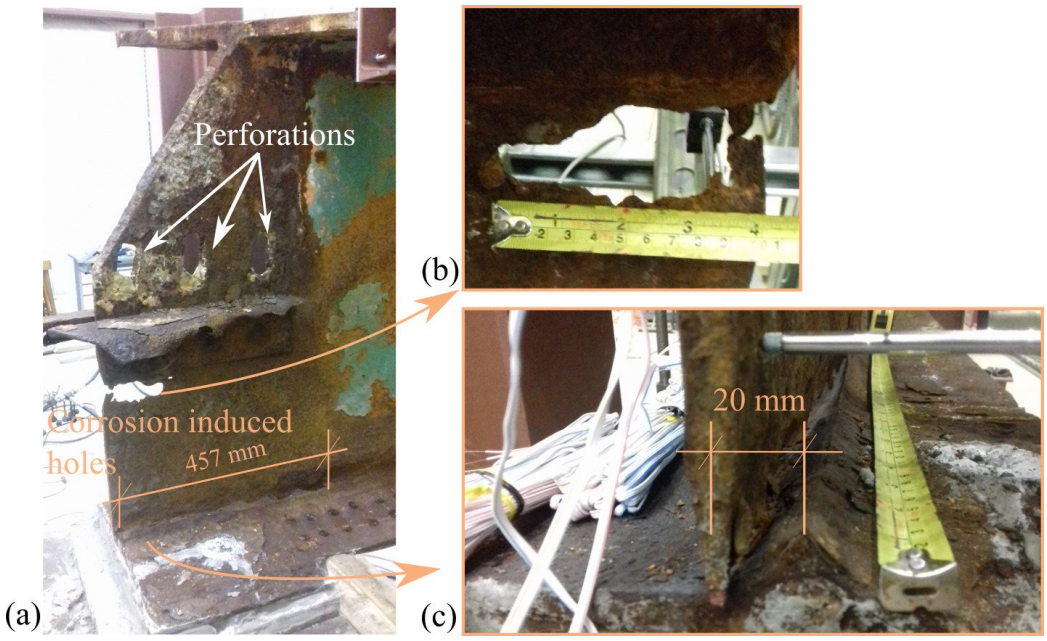

Figure 3.4: (a) Specimen 3 is a 84 cm deep girder obtained from Bridge A, with two corrosion-induced holes. (b) Hole located mid-height. (c)The hole located directly above bottom flange extends 15.2 cm beyond the bearing.

that localized section loss is observed at the boundaries between the web and the concrete diaphragms, due to increased humidity. The second area of distinct section loss extends 50 cm diagonally across the web between the steel angle sections and the bottom flange. The third distinct area is a 12.7 cm long by 2.5 cm high area at the bottom of the web. The defining feature of Specimen 2 is the significant out of plane web deformation equal to 40 mm or 2.7 times the intact web thickness at its maximum value. In addition, this specimen also had a flange hole (7.6 cm x 3.8 cm) on one side of the web just outside of the bearing area.

Specimen 3 is a 850 cm long 33WF125 girder (Table 3.1). Two corrosion-induced holes in the web could be observed at the corroded end. The first one (457 mm) was located directly above the bottom flange (Fig. 3.4a) extending 152 mm beyond the end of the bearing. The second hole is located below the steel section angles, similar to those in Specimen 1 (Fig. 3.4b). The extensive material discontinuity above the

bottom flange had allowed the web to deflect sideways while the girder was in service. The maximum out of plane deformation of the web is observed above the outer edge of the bearing and equals 20 mm or 1.4 times the intact web thickness (Fig. 3.4c).

3.1.3 Bridge B Beams

The superstructure of Bridge B consisted of beams that had a full-depth reinforced concrete diaphragm at each end, (Fig. 3.5). After the concrete diaphragms were removed, three holes made in the beam webs to pass diaphragm reinforcement were revealed. The top flange of the beams was not encased in the deck, exposing the entire beam to weather and environmental conditions. Considering that the maximum clearance between the lower face of the deck and the stream bed did not exceed 2.4 m, the bridge was located in a high moisture environment. The extensive flange section loss observed throughout the length of beams in Bridge B could be attributed to stream flooding combined with moisture exposure.

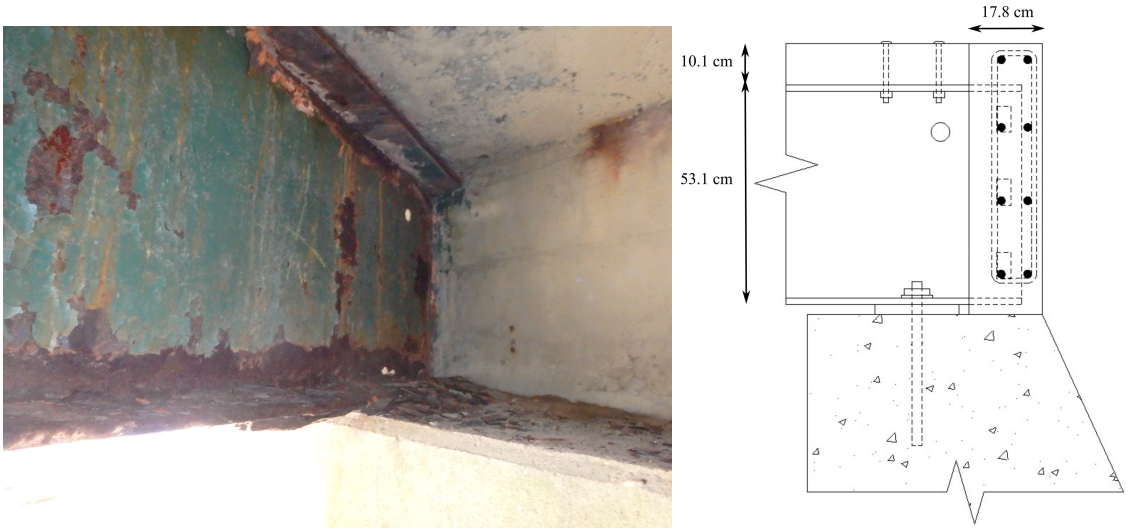

(a) (b)

Figure 3.5: (a) Typical, in service, configuration and (b) construction details for Bridge B (Specimens 4 to 6)

Except for flange corrosion, visual inspection of Specimens 4 to 6 indicated common section loss characteristics due to the in-service geometry configuration. The end region of the web that during the in-service period was concrete embedded did not undergo significant section loss, while the corrosion profile beyond this area is similar for beams in Bridge B. Finally, it is worth noting that in contrast with the beams obtained from Bridge A, despite the extensive thickness loss in the bottom flange, bottom flanges were not significantly warped during demolition.

Specimen 4 consists of a 690 long 21WF73 beam (Table 3.1) with extensive corrosion along its whole length (Fig. 3.6). The most severe web section loss is observed at the tested end. Regarding the condition of the flange, the remaining thickness of the bottom flange close to the support area, is limited to 4.3 mm (nominal flange thickness is 14.6 mm). At the interior edge of the bearing, the width of the flange decreased by approximately 25 mm from the tip on each side of the web because of corrosion. No initial out of plane deformation was observed at the bearing area. However, the specimen was heavily distorted and bent along the transverse axis of the web. Based on this observation, a level was placed along the longitudinal direction of the web, where visual inspection indicated the existence of out of plane deformation. Subsequently, a measured tape was employed to define the gap between the web and the level. The maximum lateral deflection was equal to 43 mm at a location equal to 2.1 m away from the far end. This lateral deflection generated local buckling of the flange as illustrated in Fig. 3.6b. This large lateral deformation could have been caused during demolition of the bridge.

Specimen 5 is a 613 cm long 21WF73 (Table 3.1). The beam was delivered to UMass testing facilities without the bearing plates found in other beams extracted from Bridge B. To provide a bearing surface, the test end (corroded) was supported on a 35.6 cm long plate initiating from the outer edge of the flange. However, grout

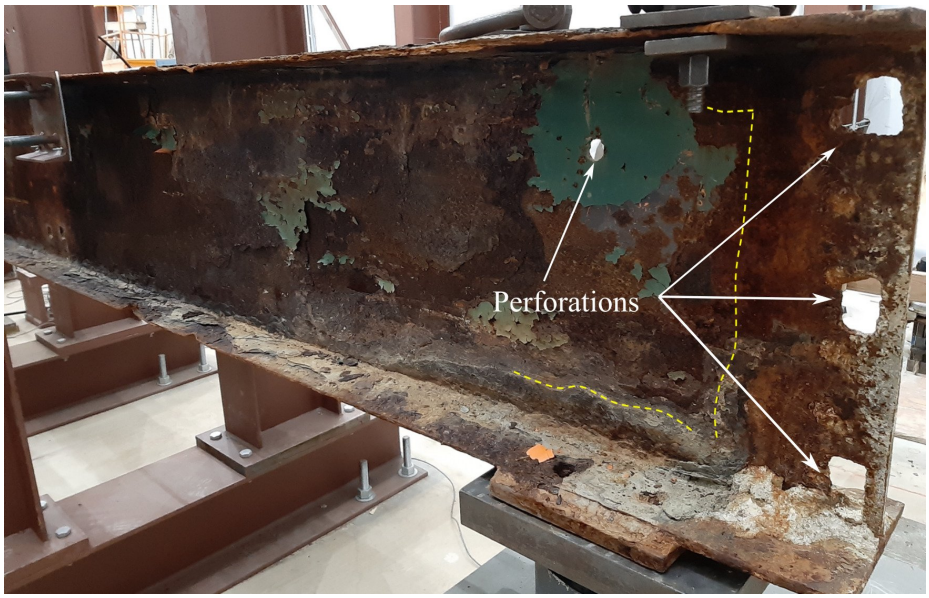

(a)

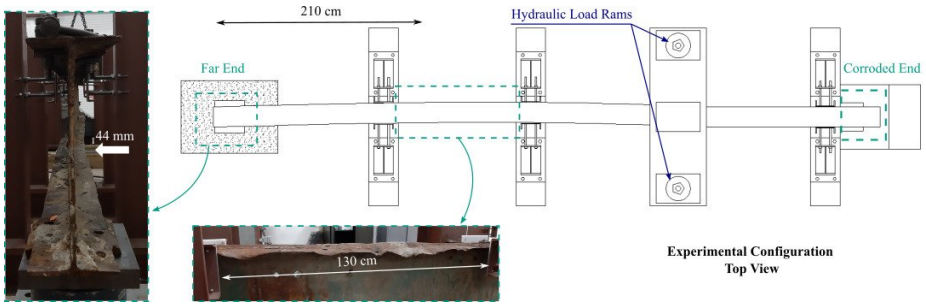

(b)

Figure 3.6: (a) Side elevation of Specimen 4, obtained from Bridge B. The yellow line highlights the areas with extensive section loss. (b) This Specimen is bent along the transverse axis of the web generating local buckling of the flange.

was applied in laboratory between the bottom flange and the support plate to provide a uniform bearing surface for testing. Regarding the corrosion, similar to all specimens obtained from Bridge B, extensive section loss was observed in the web and both flanges (Fig. 3.7). Corrosion was more pronounced in the proximity of the support where the flange widths decreased significantly. Additionally to the thickness reduction, a 15 by 51 mm^2 hole is located mid-height of the web while two more horizontal holes appear in the web. At the top of the web, a hole extends 127 mm longitudinally and up to 44 mm vertically, while at the bottom, the hole length is 203 mm.

Specimen 6 is a 612 cm long 21WF59 (Table 3.1) and similarly to Specimen 5 the bearing plates had been removed during the demolition. For the experimental process, the corroded end was supported by a 35.6 cm long plate with 3 cm overhang length. The unique characteristic of this specimen was a C-shaped opening (Fig. 3.8) formed vertically in the web along the location where the concrete diaphragm used to be, and horizontally along the web-flange connection. In detail, the gap extends 533 mm close to the bottom flange, 457 mm along the depth and 406 mm close to the top flange. This gap configuration creates a portion of web that is free along 3 edges, and which has deflected sideways up to 10 mm, as shown in Fig. 3.8b, while the end of the web, which was embedded in concrete while in service, remained unaffected. The center axes of the deflected and perfectly straight web are illustrated with a dotted and a dashed line, respectively.

3.1.4 Testing Configuration

The laboratory setup was designed to generate high shear near the most highly corroded end of each beam. All beams were tested in a simply supported condition (Fig. 3.9). By observation of inspection reports provided by MassDOT, it was noticed

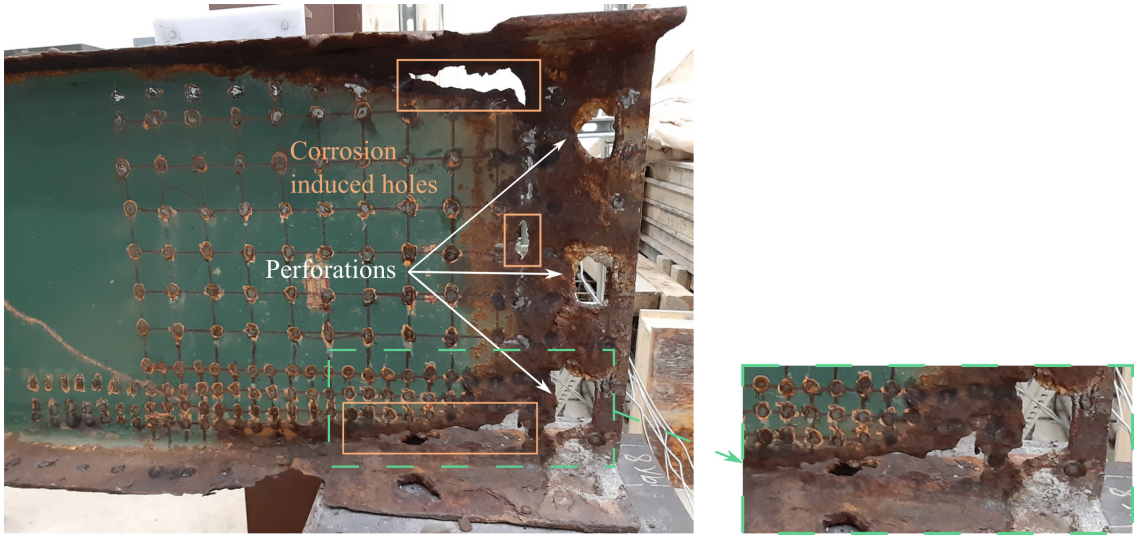

(a)

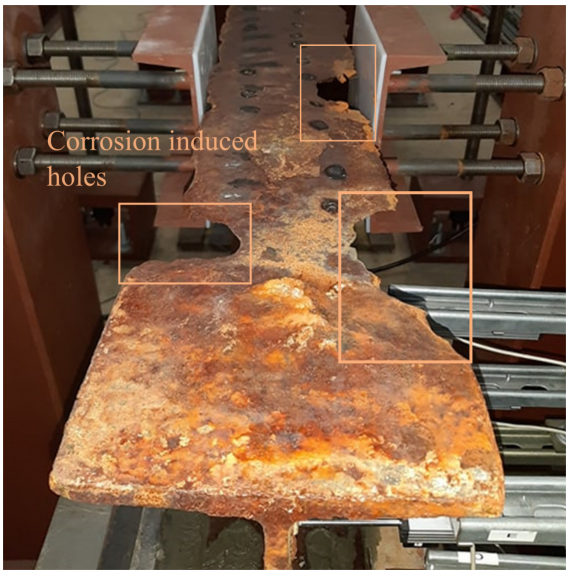

(b)

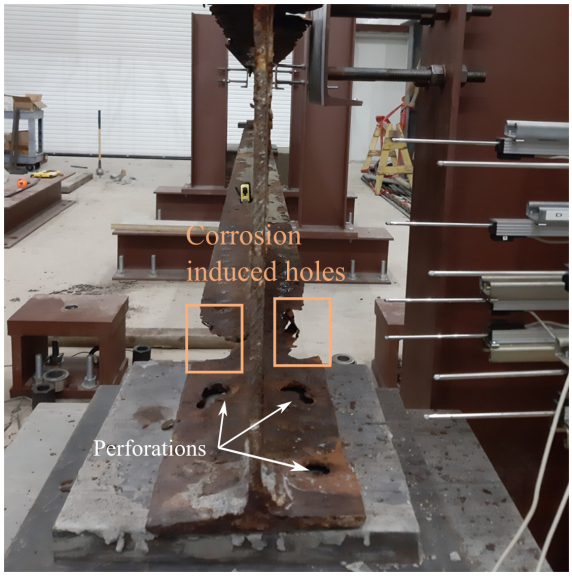

(c)

Figure 3.7: (a) Side elevation of corroded end, (b) top and (c) bottom flange condition of Specimen 5. This specimen is a 54 cm deep girder obtained from Bridge B, with extensive section loss along both flanges.

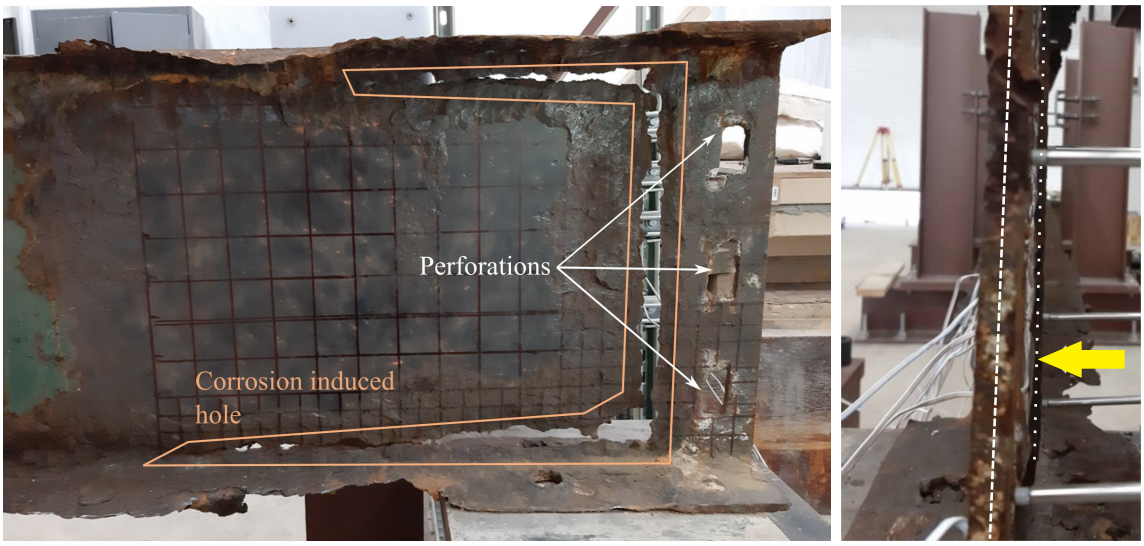

(a) (b)

Figure 3.8: (a) Side elevation of corroded, and (b) web sideways deflection of the 53 cm deep Specimen 6, obtained from Bridge B.

that the majority of the state's structurally deficient bridges were built between 1940 to 1980. According to the construction drawings of these bridges, the steel beams were typically not designed as composite with the concrete deck. Shear studs are not implemented to promote interaction between the steel beam and the concrete deck, although at the in-service configuration of Bridge A the top flanges of the beams were encased in the deck. This encasement covered just the thickness of the top flange and it is therefore controversial how much composite action can be developed. Based on the non-composite design assumption, a deck slab was not cast onto the girders prior to testing. The top flange was laterally supported to prevent lateral-torsional buckling from becoming the governing failure mode; cantilevered braces were placed every 152 cm along the length of the specimen as shown in Fig. 3.9.

Loading was accomplished using two 60-ton through-hole jacks, placed in parallel, applying load to the specimen's top flange through a cross beam. The cross beam was anchored to the strong floor of the lab using two high strength threaded rods

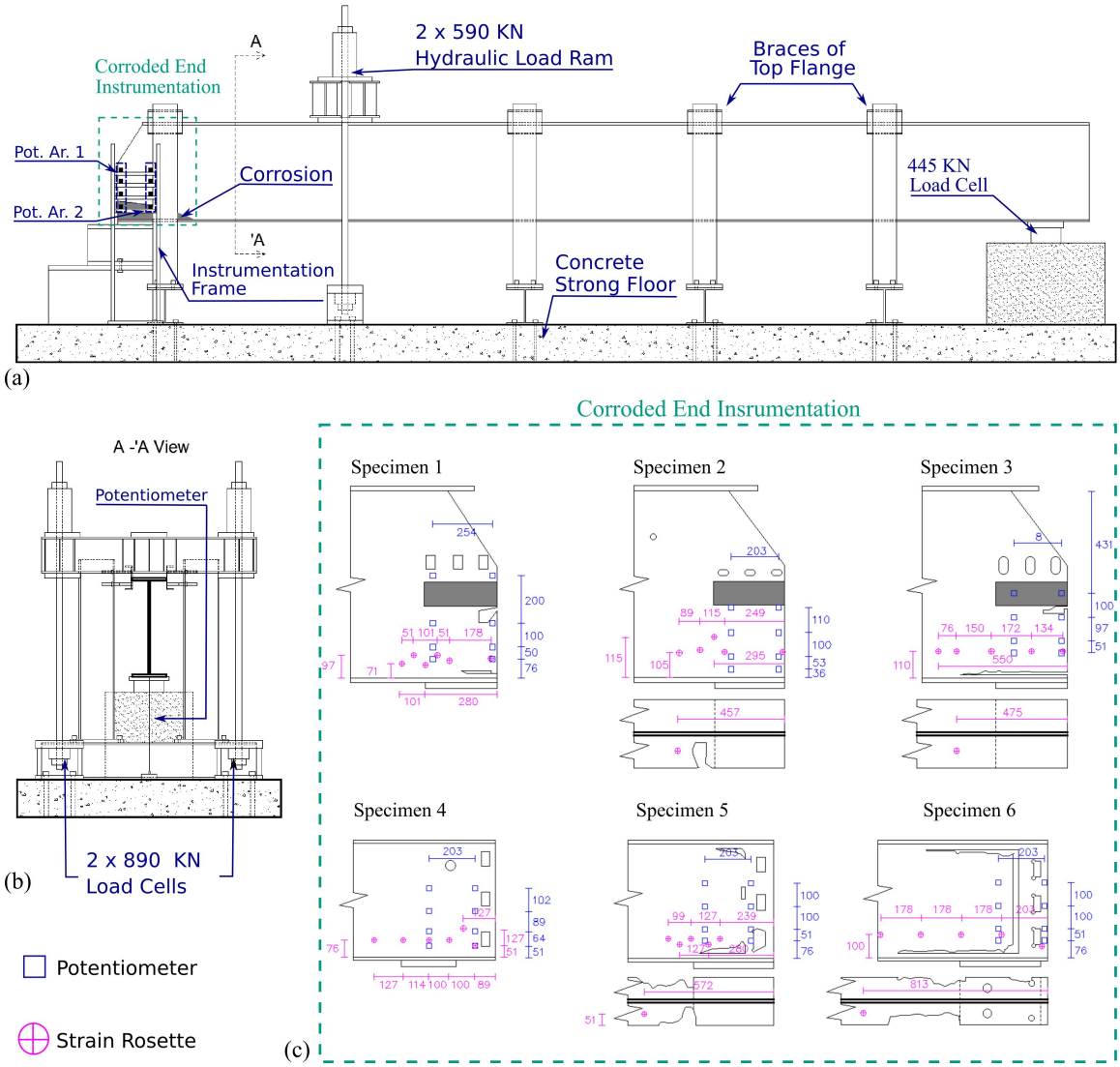

Figure 3.9: (a) Side and (b) front view of the experimental and instrumentation configuration. The load is applied to the top flange, which is restrained every 152 cm to prevent failure modes related to lateral torsional buckling. (c) Detailed representation of the potentiometer and strain rosette configurations for each specimen, the displayed dimensions are in mm.

attached to base blocks (Fig. 3.9). In terms of this thesis, the beam end closer to the applied load is referred to as the tested end while the other end is the far one. The configuration in these tests allowed for a more realistic representation of actions occurring near the end of beams supporting a deck in contrast with specimens subjected to compression forces applied directly to the web.

3.2 Instrumentation

All specimens were instrumented to record loads and deformations. In order to measure the applied load, two 890 kN load cells were placed at the lower point of the threaded rods. A load cell, with 445 kN capacity, was installed beneath the far end to record the reaction force. A pressure transducer was installed to measure pressure of the hydraulic fluid in the hose downstream of the hydraulic pump as a backup system to determine load.

Nine displacement potentiometers were implemented to record vertical as well as lateral deflections of the beam during testing. A potentiometer (Fig. 3.9b) was used to measure the maximum vertical beam deflection. This potentiometer has a 127 mm measuring capacity and it was installed on the outer face of the bottom flange beneath the point of load application. Eight potentiometers were used to measure the out of plane displacements of the web at the corroded end. These potentiometers were installed on a frame, forming an arrangement of two columns and four rows (Fig. 3.9a). This configuration was chosen in order to record two different sets of out of plane displacements taken over the height of the web. The first array of instruments was placed close to the end region of the web (Pot. Ar. 1) and the second (Pot. Ar. 2) above the inner edge of the corroded end bearing, with measuring capacity of 102 mm. Finally, at each specimen, six strain rosettes were bonded to the corroded web and flange to measure the strains during loading to help identify changes in the strain

(and stress) field.

3.3 Cross Section Loss Measurements

Detailed thickness measurements were performed in the corroded region of the beams to determine the section loss data throughout the corroded ends using a thickness gauge with a resolution of 0.025 mm, by GE Inspection Technologies [31]. This equipment is widely used by MassDOT inspectors, and its operation is based on measuring the speed of an ultrasonic sound pulse which travels through the material. To ensure reliable readings, coating and rust must be removed prior to application of a coupling layer at the measurement location. Thickness measurements were taken at approximately 200 points; at each point a measurement was taken twice, and their average reading was recorded. For reference to the thickness loss data, a grid was drawn at each beam of interest (Fig. 3.8a), covering the full depth of the web and at least two feet along the length of the beam. The grid was drawn at a closer spacing near the bottom of the beam where corrosion was typically most severe. Contour maps illustrating the extent of the thickness reduction for each specimen are shown in Fig. 3.10.

3.4 Material Properties

Tensile tests were conducted to determine the material strength of the girders. Four 56 cm x 13 cm steel plates were cut from each of Specimens 1 and 4 from which dogbone shape coupons were machined. The material properties from one beam were considered representative of all the beams belonging to the same span in the bridge. The 8 plates were cut at several different locations in the beams in order to check variability of the material properties throughout the specimen. These locations where

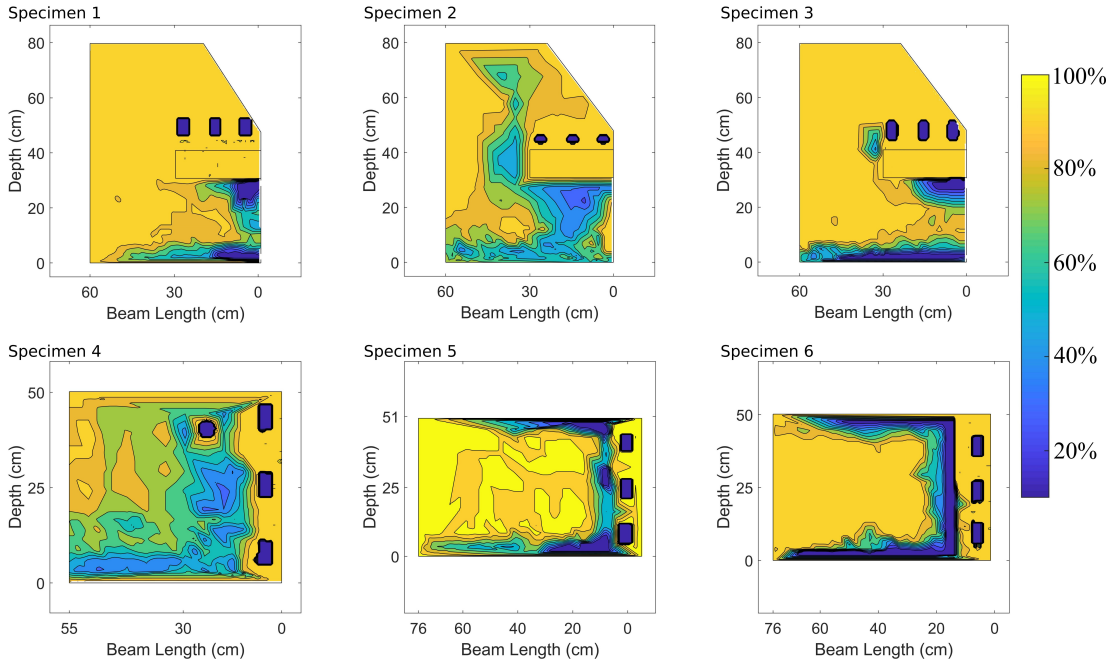

Figure 3.10: Contour maps showing the remaining thickness along the 6 studied ends. The solid blue colored areas denote both the perforations and the corrosion induced holes.

Table 3.2: Material properties of Specimens 1 (Bridge A) and 4 (Bridge B).

Specimen	Location	Young's Modulus	Yield Stress	Ultimate Stress
		GPa	MPa	MPa
Specimen 1	Bottom Flange	200	262	427
Specimen 4	Top Flange	200	241	386

coupons were taken were selected based on two factors. The condition of the steel, and the developed stress field. In detail, areas without signs of corrosion and far from regions were chosen that could have acquired permanent deformations after the completion of the experimental procedure, e.g. bearings. Tension coupon tests were conducted in accordance with ASTM Standard E8 [32]. The minimum yield stress as well as the corresponding location, for each specimen, is presented in Table 3.2. Regarding the Young's Modulus, the experimentally obtained values were slightly varying around the nominal (200 GPa) properties during the experimental testing.

3.5 Evaluation

3.5.1 Experimental Results

The failure mechanism of the six tested specimens is described through Figs. 3.11 - 3.13. Fig. 3.11 presents the total applied load load versus the vertical displacement of the bottom flange below the load application area. In order to investigate how the clear span length, and consequently the uplift is changing during testing, the applied load distribution between the supports was calculated experimentally and analytically. The ratio of the reaction force developed at the far end to the total applied load is estimated using the load cell recordings at the far end and the loading rams ("Experiment" in Fig. 3.11). Analytically, the ratio of far-end reaction and applied load was calculated using statics based on the undeformed configuration of the beam prior to testing (labeled as "Statics"). The experimentally obtained stiffness is calculated at the initial linear response of each specimen by comparing the applied load with the vertical displacement of the bottom flange beneath the area of loading. The analytically determined stiffness is also calculated, accounting for both flexural and shear components based on a no section loss assumption according to Eq. (1).

$$K_{anal} = \frac{1}{\frac{(L-a)a}{L}\left(\frac{(L-a)2a}{6EI} + \frac{1}{k_s AG}\right)} \tag{1}$$

where a is the distance from the load application area to the corroded end, A the cross section area, G the shear modulus and k_s the shear coefficient which is considered equal to the ratio of the web to the cross section area.

Fig. 3.12 presents the measured lateral displacements of the web using the potentiometer arrays on the corroded end for two different loads, 0.75 and 1.0 F_u, where F_u is the peak load measured in each specimen. These instruments recorded dis-

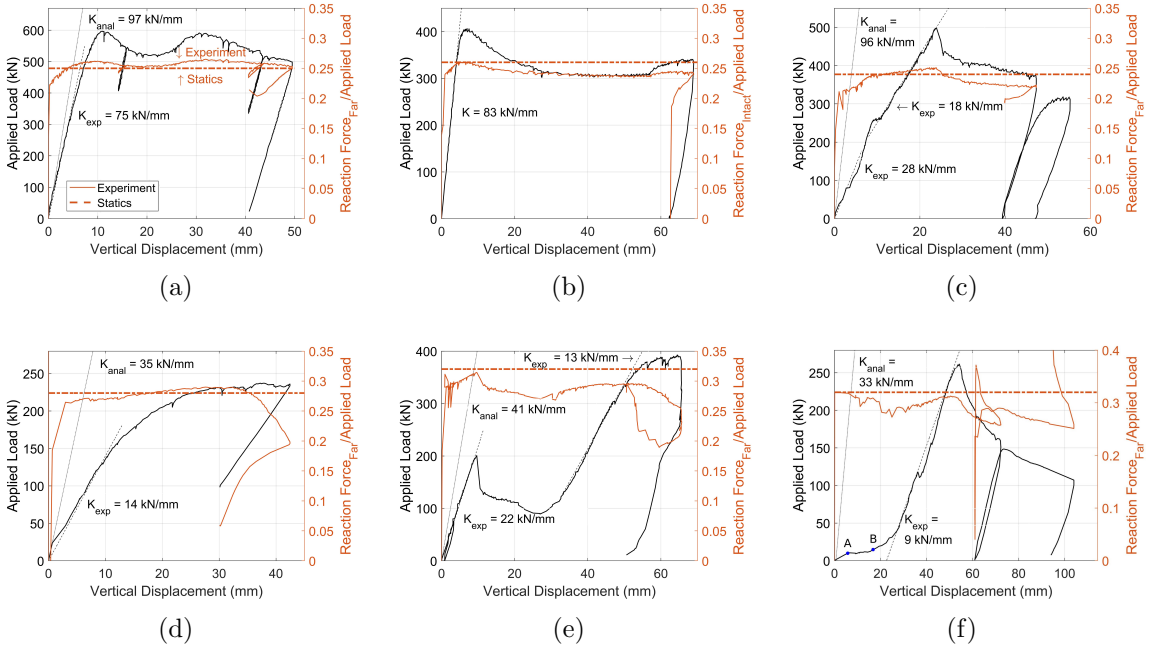

Figure 3.11: Applied load, and its distribution to the far end versus vertical displacement for Specimens (a) 1, (b) 2, (c) 3, (d) 4, (e) 5, and (f) 6. The experimentally (K_{exp}) and analytically (K_{anal}) calculated stiffness for each specimen are also included.

placements after loading initiation and thus, the initial imperfection of the beam was not captured; the black vertical line illustrates the web position assuming no initial lateral displacement. In some cases, the deformed shape lines are not connected to web bounds in order to show the discontinuous web profile due to holes. Finally, Fig. 3.14 presents the principal strain directions determined from strain rosette data on the web of Specimen 1. The condition of each corroded end of the specimens at the end of testing is presented in Fig. 3.13.

The failure of Specimen 1 is shown in Fig. 3.13a. This beam failed by web buckling at an applied load of 596 kN and vertical displacement of 11 mm as shown in Fig. 3.11a. The reaction at the corroded end at failure is 440.4 kN and the initial stiffness of Specimen 1 is equal to 75 kN/mm. Considering the relatively undamaged web and flange condition at midspan, the discrepancy between the experimentally and

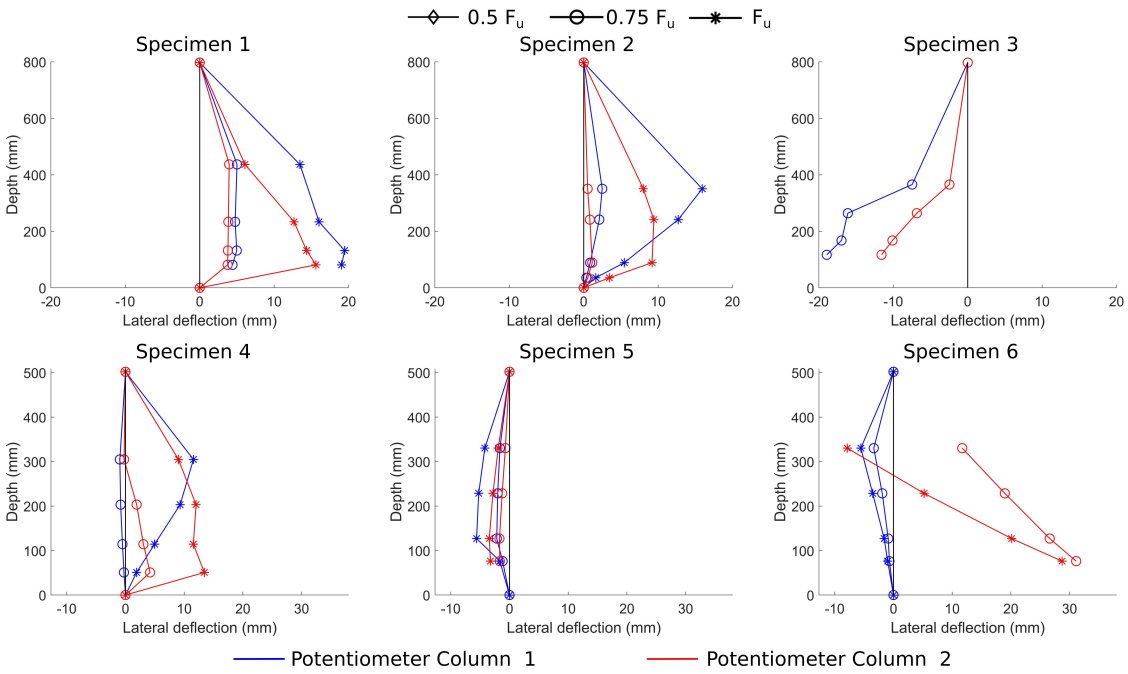

Figure 3.12: Lateral displacement profiles as were recorded from the potentiometer configuration in Fig. 3.9. The profiles are captured for two different loads, 0.75 and 1 Fu, where Fu is the peak load measured in each specimen.

the numerically calculated rigidities is mainly due to shear stiffness reduction.

With loading initiation, discrepancy is also observed between the estimated ratio of the reaction force developed at the far end and the measured data. This behavior can be attributed to the distorted bottom flange geometry at the bearing which affects the effective span length. The continuously varying ratio is associated with the uplift observed at the bearings while the applied load was increasing. The uplift did not evolve in the same way at both supports, resulting in a continuously varying effective span length as well as, ratio of the distances between the supports and the loading area.

Regarding the failure mode of Specimen 1, Fig. 3.12 shows that the web lateral deformation concentrated near the bottom. A buckling wave was created at the bottom of the web with maximum magnitude at the outer edge of the web of the

beam just above the bearing. The post peak behavior of Specimen 1 is characterized by a progressive loss of stiffness at increasing displacements, both vertical and lateral. At a vertical deflection equal to 20 mm, an increase in stiffness was observed when the upper web edge of the bottom hole began bearing against the flange. Increased load was carried by the specimen as illustrated by the second peak observed in the load-deflection curve (Fig. 3.11a), corresponding to approximately 591.2 kN. The test was terminated when the top flange was about to lose contact with the lateral support. The vertical deflection at this point was almost 50.8 mm.

Specimen 2 failed from web buckling at applied load of 406.6 kN and vertical displacement of 7 mm, Fig. 3.11b. The load on the corroded end, obtained by subtracting the far end reaction from the applied load was equal to 300.7 kN. The failure mode was governed by the initial web imperfection (Fig. 3.3b) which defined the lateral deflection profile (Fig. 3.12).

The initial stiffness of Specimen 2 is 83 kN/mm. Similar to Specimen 1 the observed discrepancy from the analytical rigidity (115 kN/mm) is attributed to the section loss at the beam ends. Once again at the post buckling regime, sudden collapse or failure was not observed. The applied load remained approximately constant (311.4 kN) between displacements of 30 and 55 mm. After web buckling was initiated, the bottom flange experienced extensive uplift at the end of the beam because of the rotation induced as the web folded around the area of extensive thickness loss which extended diagonally across the lower half of the web (Fig. 3.3b). Unexpectedly, the specimen gained stiffness at a vertical displacement of 56 mm. This behavior is attributed to the onset of web bearing on the top of the anchor protruding from the bottom flange (Fig. 3.13b). It should be also noted that, compared to Specimen 1, the bottom flange uplift was significantly higher during the whole experiment. The experiment was terminated when the limit of the lateral support was reached, at a

vertical deflection around 71 mm.

For Specimen 3, immediately after loading initiation, the existing gap between web and bottom flange was closed and the web started bearing against the flange. This enabled load to be transferred into the support through bearing between the web and flange. Ultimately, 500 kN were applied to the girder for vertical displacement of 24 mm (Fig. 3.11c). The load on the corroded end, obtained by subtracting the far end reaction from the applied load was equal to 375 kN. Up to peak load, three distinct segments with varying stiffness are observed. At the first segment, the stiffness is equal to 28 kN/mm and it reduces up to 18 kN/mm prior failure. It is also worth noting, that all segments are almost linear, denoting that this behavior does not result from local yielding, but rather is influenced by the geometry of deformation due to sliding of the web on the flange along the web-flange gap present in this beam. At 80.1 kN applied load, longitudinal displacement occurred instantly and is captured with a straight line in Fig. 3.11c, point A. Contrary to point B for 258 kN which is the result of two discrete actions: in addition to the web sliding on the flange, instability phenomena took place in a narrow region above the upper web hole that had experienced 50% section loss (Fig. 3.10). Large deformations were observed within this region throughout the test, Fig. 3.13c.

The lateral displacement profile at peak load, was not captured because some of the potentiometers had to be removed prior to test completion to avoid damage to the instruments after the beam entered large deformations. However, the recordings for 0.5 and 0.75 F_u reveal a concentration of lateral displacements within the lower half of the web, and as it can be seen in Fig. 3.13c the web bent around a line that extends from the inner edge of the upper corrosion hole to the inner edge of the long bottom hole.

The peak load of Specimen 4 was 237.1 kN corresponding to a vertical displace-

ment of 38 mm (Fig. 3.11d). The initial imperfection of the beam (Fig. 3.6b) influenced the deformation during testing, with lateral displacements initiating at mid-span and ultimately leading to a global instability mode along the longitudinal axis, preventing the corroded end of the beam from reaching its capacity. Nevertheless, it is worth noting the load redistribution, which took place for vertical displacement greater than 33 mm. For a modest 2.3% rise in the applied load (from 230.9 kN to 236.2 kN) toward the end of the test, the fraction of load transferred to the far end is decreased from 29% to 19% (Fig. 3.11d).

Local instability of the region around the corroded end was not observed during the test. However, visual inspection of the final beam condition revealed that crippling had occurred along the longitudinal axis at the narrow strip region with limited remaining thickness, highlighted with a yellow line in Fig. 3.6a. Even though the initial stiffness of the specimen which is estimated equal to 14 kN/mm dramatically decreased after the yielding load (155.7 kN) at which the local buckling occurred, it is not clear if the observed instability phenomenon results from the bearing load or it is second order phenomenon due to the extensive mid-span lateral and torsional deflection. The final condition of Specimen 4 is presented in Fig. 3.13d.

Two peak loads are observed for Specimen 5, at 200.6 kN and 392.8 kN, (Fig. 3.11e). Based on the load distribution between the supports, the reaction forces developed at the corroded end are 137.5 kN and 292.2 kN at the two peak loads. The significant damage observed at the corroded end of the beam (corrosion and holes), controlled the failure of the specimen. At 137.5 kN bearing load, a brittle failure was observed at the narrow material strips, with width 38 mm each, located at the outer web part, Fig. 3.7a. The web uniformly translated out of plane. The potentiometer recordings at peak load depict a buckling wave formed at the region measured by Pot. Ar. 1 (Fig. 3.9a,c), while an almost linear displacement profile was captured by Pot.

Ar. 2. The sudden failure observed during testing was accompanied by a sudden 30% load loss.

The extensive flange section loss that was observed throughout the length of beams in Bridge B, in addition to their shallow depth, increased the harmful reduction of flexural stiffness, resulting in increased discrepancy from the analytically calculated values at loading initiation. At the post-buckling regime, the continuously reducing stiffness, following the initial branch with 22 kN/mm, continued up to applied load equal to 89.4 kN (56% reduction compared to peak load), where the protruding web began bearing on the bottom flange. The system gained stiffness (13kN/mm) and began retaining additional load up to the total load of 392.8 kN where a global system failure mode initiated. The extensive lateral displacements at the corroded end distorted the member's center line from straight, Fig. 3.13e. This condition could have triggered the long wave instability mode which resulted in the lateral translation of the corroded end. The experiment was terminated due to the distortion of the experimental support configuration under the corroded end.

For Specimen 6, after the loading initiation, the web had limited contribution to specimen's stiffness due to the hole configuration. The initial plateau observed at the load displacement curve (point A in Fig. 3.11f) captures mainly the flange action and is characterized by rapidly increasing deformations. Once the total deflection of the unrestricted web reached 15 mm (point B in Fig. 3.11f), it began bearing against the flange, at which point the system gained stiffness and started retaining additional load. The non-restricted web continued experiencing large deformations, following the initial imperfection profile (Fig. 3.12), while the stiff part of the web (blue line) was deflecting along the opposite direction. Finally, at 261.5 kN applied, the bottom of the web bearing on the flange remained almost at constant position compared to 0.75 Fu, while the top part translated 20 mm to the left (Fig. 3.12). The post peak

regime is characterized by rapidly reducing stiffness and extensive uplift, with the unloading - loading curve at 160.1 kN, following an almost identical path.

One of the expected challenges, that is addressed in Chapter 4, is the simulation of the bearing area and in particular the interaction between the bottom flange and the bearing plates. Consequently, the strain rosettes configuration was mainly chosen to shed light on the bearing behavior. The main points of interest are the loading path to the support as well as the reaction force development along the bearing length. The recordings revealed forces were developed along the whole bearing, which were progressively gathered towards the inner bearing edge, reflecting the uplift development. A clear pattern emerging from Fig. 3.14 is that the web beyond the bearing edges is subjected to shear strain deformation. Most of the specimens had holes along the web of the corroded end affecting the load path as well as the strain rosettes recordings. However, data from Specimen 1 reveal that the web above the bearing plate is subjected to direct compression, prior to uplift initiation (Fig. 3.14).

In general, each specimen represents a unique case due to the combination of beam geometry and deterioration level. However, the deeper sections of Specimens 1 to 3, obtained from Bridge A, resulted in higher capacities compared to Specimens 4 to 6, obtained from Bridge B. The failure modes of Specimens 3, 5 and 6 were governed by the corrosion holes at the bearing area. For Specimens 3 and 6, the failure load was reached with the top edge of a web hole making contact with the bottom flange, bearing load. For both cases, the web was sliding on the flange, resulting to large deformations. For Specimen 5, a second post buckling peak (Fig. 3.11) was observed due to the same mechanism, which initiated after the initial web failure. It is worth noting that, for Specimen 1, deformations were generated close to the web domain that had already crippled while the girder was in service. The extensive web deviation from straightness defined the failure mode of Specimen 2. Finally, the initial imperfection

Figure 3.13: Final condition of Specimens (a) 1 to (f) 6. The hole closed during the experiments for Specimens 1, 3, 5 and 6. The failure mode of Specimen 2 was governed by the initial web deviation from straightness. Crippling was observed for Specimen 4. Figure obtained from [1]

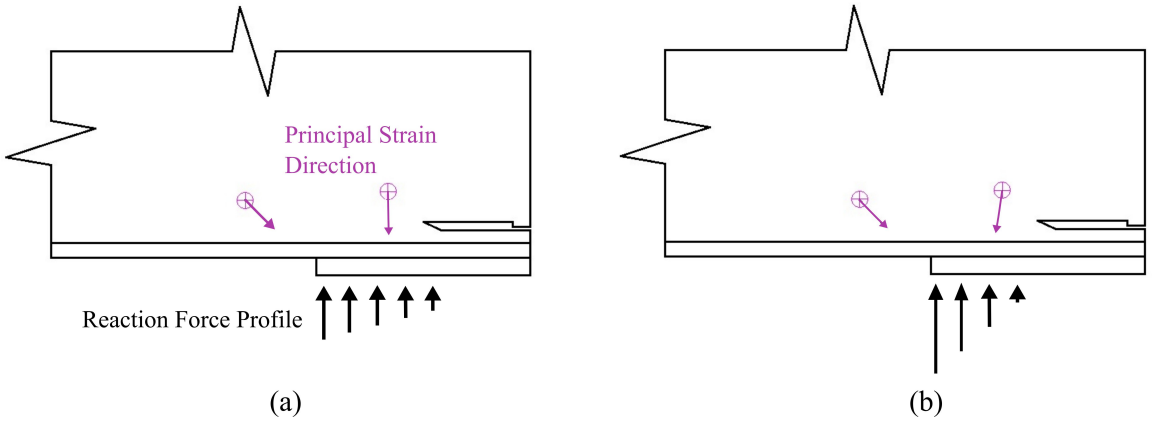

Figure 3.14: Principal strain directions for Specimen 1, and estimated reaction force profile at (a) 146.8 kN and (b) 458.2 kN applied load. While the uplift evolves the reaction forces are concentrated towards the inner bearing edge. Beyond that edge the web is subjected to shear strain deformation.

of Specimen 4 resulted to a long-wave instability mode and localized failure at the web bottom, above the support.

A common observation for all specimens is the continuously varying effective span length throughout the experimental procedure, mainly due to the evolving uplift at the bearings. For beams with relatively undamaged web and flange condition at midspan, the discrepancy between the experimentally and the numerically calculated rigidities is mainly due to the shear stiffness reduction. For specimens with extensive section loss throughout their length, the harmful reduction of flexural stiffness was increased, resulting to increased discrepancy from the analytically calculated values for intact beams.

3.5.2 Strength Evaluation According to Current Procedures

In MassDOT's Bridge Manual [7] the nominal resistance of un-stiffened corroded steel beam ends subjected to patch loading is calculated on the basis of the yielding and crippling capacities. Based on the geometric support configuration of the specimens, the nominal yielding capacity for beams with overhang less than $5k$ (Fig. 3.15)

is calculated as follows:

$$R_{n,yield} = \ f_y \ t_{ave} \ (2.5k + N) \tag{2}$$

and the crippling capacity is given by Eqs. (3) and (4):

$$R_{n,crip} = \ 0.4t_{ave}^2 \ [1 \ + \left(\frac{4 \ (N - H)}{d} - 0.2\right) (\frac{t_{ave}}{t_f})^{1.5}]\sqrt{\frac{EF_y t_f}{t_{ave}}}, \text{ when N/d} > 0.2 \tag{3}$$

$$R_{n,crip} = \ 0.4t_{ave}^2 \ [1 \ + 3 \left(\frac{(N - H)}{d}\right) (\frac{t_{ave}}{t_f})^{1.5}]\sqrt{\frac{EF_y t_f}{t_{ave}}}, \text{ when N/d} \leq 0.2 \tag{4}$$

where k is the distance from outer face of flange to web toe fillet, N is the bearing length and d is the depth of the steel section, f_y is the yield stress, and t_f the flange thickness. The effect of deterioration is encapsulated in the form of t_{ave}, which is defined as:

$$t_{ave} = \ \frac{(N + 2.5k - H) * t_w}{N + 2.5k} \tag{5}$$

where t_w is the remaining web thickness within the area at the bottom 10 cm of the web with length equal to $N + 2.5k$, and H is the length of hole within the same domain. Within the area of interest, the total length of both corrosion induced holes and perforations is considered, as shown in Fig. 3.15. A detailed description of the location and the corresponding length of each hole is given in Paragraph 3.1.2. For Specimen 4, where the overhang past the bearing is more than $5k$, the $2.5k$ term in Eqs. (2) and (5) is substituted with "$5k$". In order to calculate the failure load of the tested specimens according to the current procedures, the average of the conducted thickness measurements is used to estimate the remaining thickness (t_w) within the area of interest. Material properties are determined by previously presented tensile tests (Table 3.2). According to MassDOT's Bridge Manual [7], the minimum yield

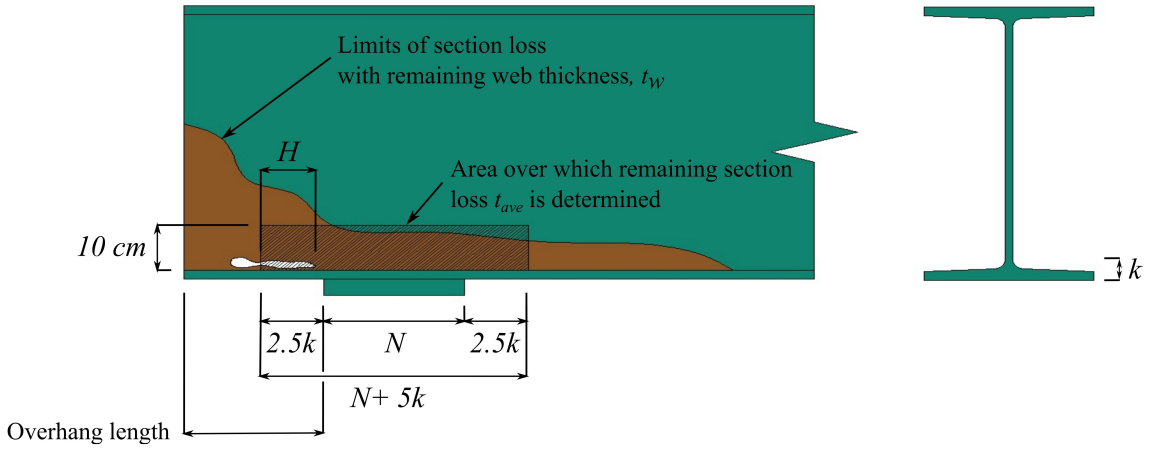

Figure 3.15: Parameters involved in the MassDOT evaluation procedures.

Table 3.3: Comparison between experimental and predicted bearing failure loads.

Specimen	N	L_0	t_{loss}	H	Failure Load	
	mm	mm	t_{web}	mm	Experimental	Calculated
					kN	kN
1	305	0	32%	152	440.8	214.4
2	300	0	40%	0	300.7	467.1
3	305	0	30%	401	375	0
4	241	171	45%	36	190.4	401.2
5	356	0	30%	254	137.5	77.4
6	356	0	10%	338	181.9	26.7

strength is considered, if there located within the area of interest. Corrosion metrics as well as the predicted capacities based on Eqs. (2) through (5) are listed in Table 3.3, where L_0 is the overhang length past the bearing.

Specimens 1, 3, 5 and 6 were all underestimated by current procedures. These specimens had web holes as a common characteristic. Specimen 2, whose failure mode was strongly affected by the initial lateral web imperfection, was the only case where the ultimate load was overestimated by the provisions. This type of imperfection is not currently considered in the Manual procedures and potentially is the reason for the discrepancy between the estimated and the actual bearing failure load. It is worth

noting that the nominal capacity of Specimen 3 equals zero due to the hole extending along the whole area of interest used for capacity estimation, and consequently t_{ave} in Eq. (5) tends also to zero.

CHAPTER 4

COMPUTATIONAL EVALUATION OF CORRODED GIRDERS

4.1 FEM Validation

The outcome of Chapter 3 allows development of a a robust finite element model, capable of accurately predicting the failure load and mode of deteriorated girders. The developed model is initially calibrated based on the experimentally obtained data of Specimen 1. Subsequently, it is implemented to simulate Specimen 2 and to validate the experimentally obtained results.

4.1.1 Mechanical Model

4.1.1.1 Geometry

The exact geometry of the two simulated specimens, as well as the experimental configuration have been presented in Paragraphs 3.1.2 and 3.1.4, respectively. However, the primary challenge for a realistic geometric representation of the tested specimens is the simulation of the irregular corrosion damage, regarding dimensions and section loss. Areas with 100% section loss can be easily surveyed and included in the model; however, the uneven thickness reduction requires a more detailed approach. Prior to laboratory testing, a grid was drawn at each tested end (Fig. 3.3b), covering the full depth of the web and at least two feet along the length of the beam. Moving from top to bottom, the grid increases in resolution, as visual inspection indicated the section loss to be most severe towards the bottom flange. A total of 201 and 193 measurements were performed along the web and flange of Specimens 1 and 2, respectively, using a thickness gauge with a resolution of 0.025 mm.

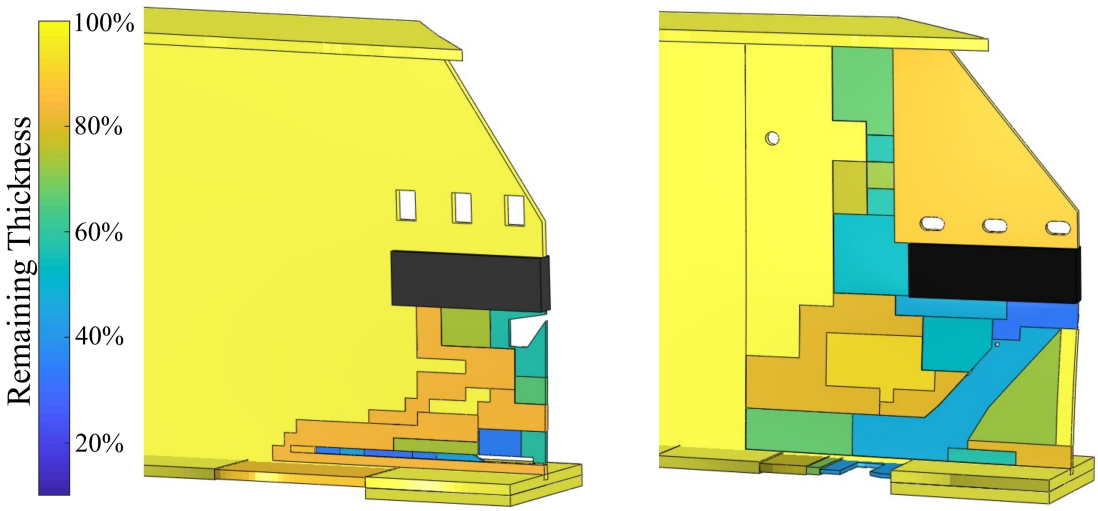

Figure 4.1: (a) Modeled remaining thickness for Specimen 1; (b) and Specimen 2, normalized with respect to the nominal cross section properties of each girder. For Specimen 2 there is an significant existing lateral deformation of the web.

In order to replicate the thickness reduction distribution, points with common or similar thickness loss were grouped together forming areas with uniform thickness reduction. These areas were included in the computational model by partitioning the corresponding web and flange faces. The simulated section loss profile is presented in Fig. 4.1. The remaining steel section angle located at the web's mid-height is simulated with increased thickness (38 mm).

In addition to section loss, corrosion results to disturbance of the members alignment. Consequently, imperfections are introduced in the model based on the eigenmodes shapes. Each model is initially solved using an eigenvalue buckling analysis algorithm. Then the eigenmode that better matches the web shape of the actual beam is introduced as an initial geometric imperfection for the quasi-static analysis, scaled to the measured maximum lateral deviation of the web.

For Specimen 1, the part of the web that extends beyond the red dashed line (Fig. 4.2a) is free at the three edges. The web is not supported at the top due to the

(a) (b)

Figure 4.2: Comparison between the actual and the modeled imperfect geometry for Specimen 1; (b) and Specimen 2. For Specimen 1, the part of the web that extends beyond the red dashed line is free at the three edges due to the skewed cut and the corrosion-induced hole.

skewed cut, and at the bottom a hole is located parallel to the flange. This lack of constraints results in uniform, along the web depth, deviation from plumbness with peak amplitude up to 14 mm. On the other hand, none of the eigenmodes managed to capture the uniform deviation profile, underestimating the condition of the web at its lower part. Fig. 4.2a displays the chosen eigenmode which is characterized by a half buckling wave that forms along the whole depth.

For Specimen 2, the maximum initial web lateral deviation is observed at mid-height and equals 40 mm. The eigenmode which was closer to the shape of the actual beam, overestimates the web condition where the bolted steel sections are located, Fig. 4.2b.

4.1.1.2 Material Properties

The material properties of steel were determined by performing tensile tests on coupons extracted from Specimen 1. Both girders were part of a unique span, constructed at the same period of time. Based on this observation, material properties from one beam are considered representative for all the beams belonging to the same

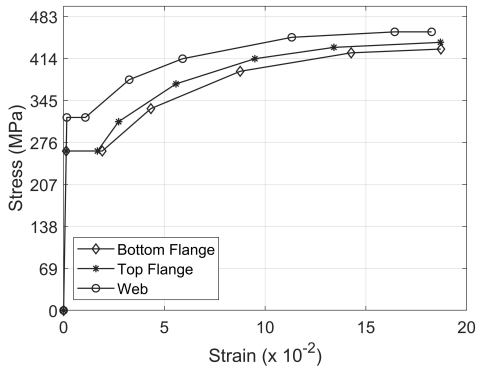

Figure 4.3: Backbones of stress strain curves of tested coupons considered for the finite element analysis of Specimens 1 and 2.

group. Consequently, common material properties are used for both modeled specimens. Simplified backbone curves (Fig. 4.3), formulated by several linear branches each, are defined based on the experimentally obtained stress strain relationship for the web and the flanges. The coupon testing revealed discrepancy in yield and ultimate stress of the steel at web and flange which can be attributed the manufacturing process of these W sections at that time. However, the curves for the top and bottom flange are similar, thus the results are considered satisfactory.

4.1.2 Finite Element Model

The commercial finite element software ABAQUS [33] is utilized for simulation and analysis of the laboratory experiments. Shell elements are employed to approximate a three-dimensional continuous body with a surface at the middle of the section. The actual thickness is taken into account, and assigned as a parameter to the corresponding elements. The two dimensional assumption is considered valid due to the significantly smaller thickness of the beam's components compared to the other two dimensions.

Based on a sensitivity study on mesh size, type, and section points number, the

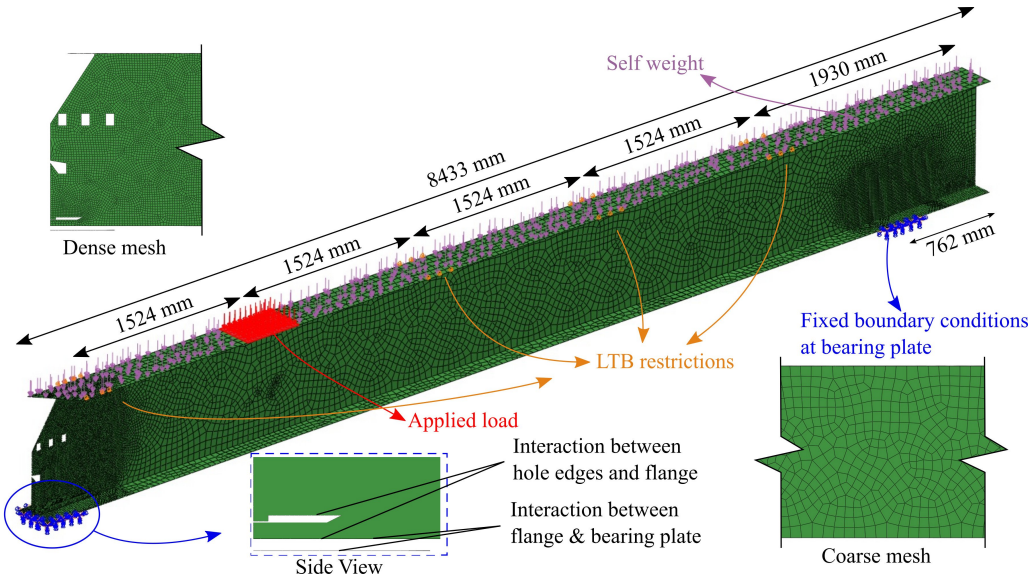

Figure 4.4: Developed finite element model for the experimental configuration of Specimen 1. Dense mesh is defined at the bearings and coarse towards the midspan. Interaction properties along the normal and the tangential direction are introduced to accommodate contact between the bearings, the bottom flange and the hole edges.

four-node linear element S4R is preferred. S4R contains a unique integration point in plane, and five section points through the shell thickness are chosen, capturing bending, and stretching effects. At the beam ends, where stress concentration and the failure are expected to occur, a dense mesh area defined, Fig. 4.4. This area covers the full height of the web and its length exceeds the corrosion length by 12.7 cm. For this area the element size is 1.3 cm. At midspan the element size is set equal to 5.1 cm.

Significant effort was made towards the accurate simulation of the experimentally observed behavior of the bearing area. Strain rosettes installed close to the support revealed reaction force development along the whole bearing length. The reaction was progressively concentrated towards the inner bearing edge, as uplift at the outer edge occurred for increasing applied load.

In the finite element model, both the bearing plate as well as the girder are sim-

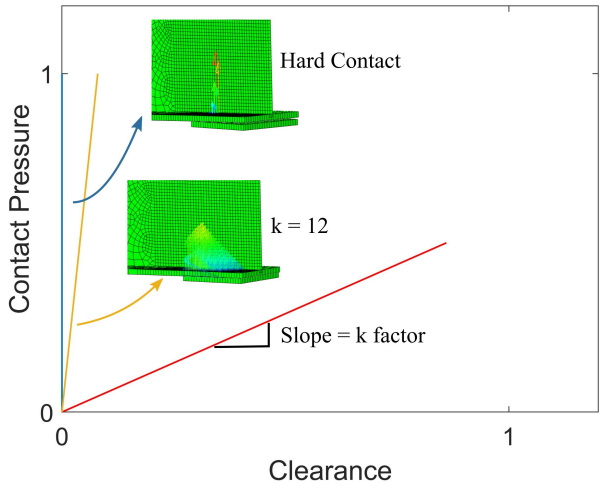

Figure 4.5: The interaction between the bearing plate and the bottom flange is described with "softened contact", where the pressure overclosure relationship is defined by the value of the "k" factor.

ulated with shell elements in contact, which enables the definition of the interaction between the two surfaces along the normal and the tangential direction. An infinitesimally stiff interaction ("hard contact") along the normal direction, instantly results in a hinge formulation along the inner bearing edge (Fig. 4.5), deviating from the actual behavior. Thus, a stiff but "softened contact" is preferred. The interaction is defined using a linear contact pressure - overclosure relationship, which is defined by the stiffness "k" of the linear relationship. The "k" value has been calibrated using the experimental data from Specimen 1.

A "hard contact" constraint is used for the normal contact behavior between the web edge nodes and flange surface in case of a hole. This formulation eliminates the penetration of the slave nodes (web) into the master one (flange). Except for contact properties defined in the normal direction between the bottom flange and the bearing plate, friction is also defined to simulate the interaction between the bottom flange and the bearing plate in the tangential direction. In order to define a friction coefficient value, a sensitivity analysis is performed. Analysis are consecutively performed for

friction coefficients in the range of 0.5 to 0.9 with 0.05 intervals. The beam capacity seemed to be only slightly affected by the contact friction coefficient variation, as the maximum divergence among the results is 1.2%. A contact coefficient equal to 0.74 [34] is selected to simulate the steel to steel interaction for the rest of the work.

In the analytical model, the load is applied as uniform pressure, which covers the whole flange width and extends 46 cm along the top flange, replicating the loading plate dimensions. Out of plane displacement is not allowed at the locations of LTB supports, and the bottom flange of the girder is supported on two steel bearing plates, which are considered fixed.

Quasi-static analysis is performed to simulate the applied load of the experimental configuration. This type of analysis terminated once instability phenomena occur, as post-buckling behavior is beyond the scope of the current thesis.

4.1.3 FEM Calibration

The only remaining parameter that requires calibration is the contact factor "k". Based on the experimentally obtained results from Specimen 1, the "k" value is set equal to 12 to mach the applied load - vertical displacement relationship presented in Fig. 4.6a. Regarding the peak load, the numerical model predicts failure at 575.4 kN of applied load, while the experimental value equals 596.5 kN (underestimated by 3.5%).

A detailed comparison of the lateral displacements recorded from the potentiometers and the associated nodal out of plane translations from the FEM model is shown in Fig. 4.7a. The location of the potentiometer for each graph is illustrated with a rectangle. It should be mentioned that there is a small source of error, considering that a potentiometer measures the lateral displacement at a fixed location in space because the instruments were attached to a fixed frame as loading was applied on the

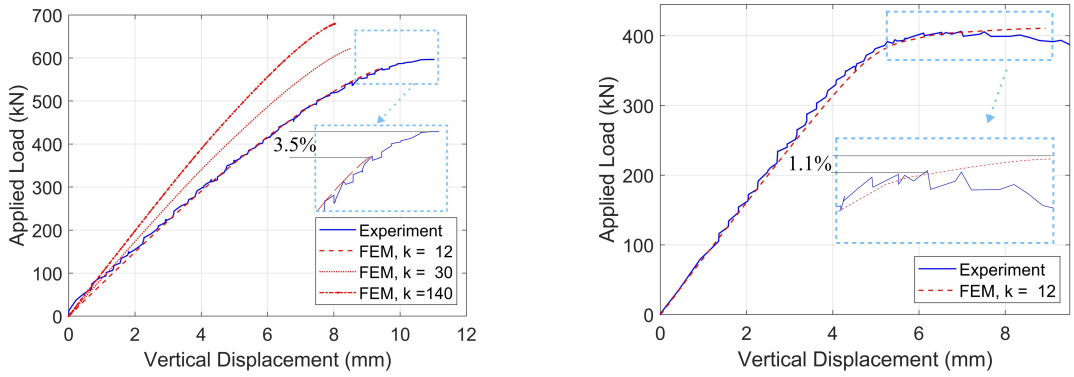

Figure 4.6: (a) Calibration of the finite element model for the selection of the 'k' factor based on experimental data from Specimen 1. The Specimen's behavior is accurately captured for 'k'= 12. (b) Validation based on experimental data from Specimen 2 and 'k'= 12 captures the experiment accurately as well.

beam specimen. The corresponding nodal value in the finite element analysis (FEA) refers to the node that in the model initially (before loading) was located at the same location with the potentiometer (this node in the FE model translates during loading of the beam in the model).

The general picture emerging from Fig. 4.7a is that the model satisfactorily captures the failure mode. However, the accuracy varies among different potentiometers. A possible interpretation of this discrepancy is the initial applied geometric imperfection. In detail, at mid-height locations where the imported imperfection managed to satisfactorily represent the actual web shape, the numerical data is consistent with the experimental one. An increasing discrepancy is observed for potentiometers placed lower in height, where the initial uniform deflection was not reproduced accurately by the eigenmode.

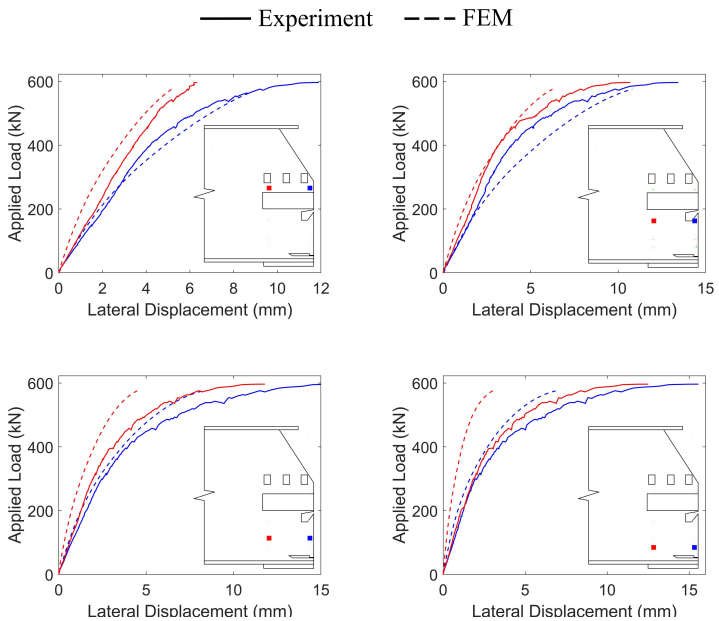

(a)

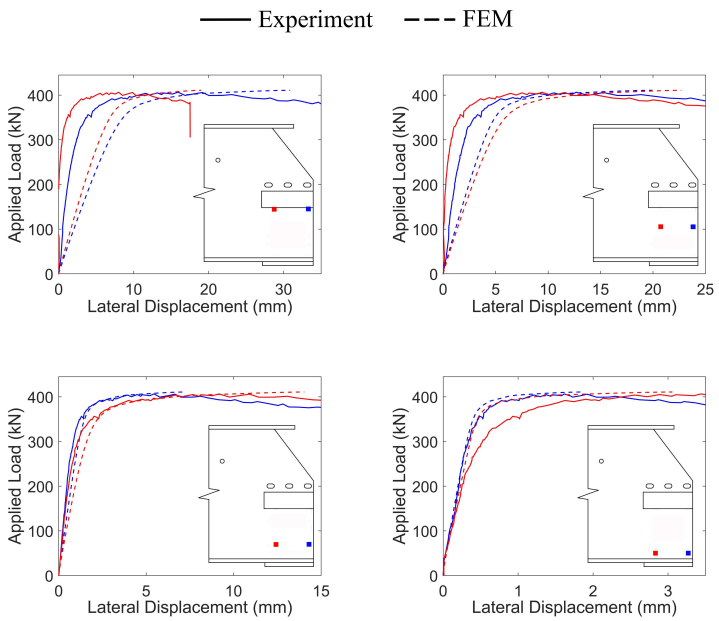

(b)

Figure 4.7: Comparison of the lateral displacements recorded from the potentiometers and the associated nodes from the FE model for (a) Specimen 1 and (b) Specimen 2. The numerical model provides increased efficiency at locations were the applied eigenmodes managed to accurately capture the real imperfect shape.

4.1.4 FEM Verification

Following the procedure previously described, Specimen 2 was also simulated and analyzed using k = 12. Both the stiffness and the peak load depict an excellent agreement between the experimental and numerical results. The numerically captured applied failure load overestimates the actual one by only 1.1% (Fig. 4.6b). Regarding the potentiometer recordings (Fig. 4.7b), the experimental data from the four bottom instruments is very consistent with the numerical one. On the other hand, for the instruments placed mid-height, where the simulated initial imperfect geometry overestimates the web condition, large displacements are numerically obtained, and consequently reduced stiffness compared to the potentiometer recordings is captured. This behavior can be attributed to the existence of the steel section angles from the diaphragm, which at the numerical model, were considered by increasing the applied thickness at the corresponding area. The results indicate that the model slightly underestimates the stiffness of the web's portion where the steel sections are bolted on it. Taken all together, stiffness variation between the numerically and experimentally obtained stiffnesses is related to the representation of the initial out of plane displacement and not to the contact factor k value.

Based on the presented results for Specimens 1 and 2, the model is considered valid and capable to capture the stiffness, the failure load as well as the failure mode of the corroded specimens.

4.2 Parametric Analysis

Having validated a finite element model, the next goal is to establish a fundamental understanding of the deterioration impact on the I-beams bearing capacity. Initially, the design space of the parametric analysis is identified. Subsequently, the developed

girder-level numerical model is employed in a series of simulations within this design space to explore the parameters which significantly affect the bearing strength of corroded rolled girders.

4.2.1 Analysis Set-up

4.2.1.1 Damage Scenarios

In a previous study, the author studied the deterioration condition of 93 steel bridges in the state of Massachusetts [35]. Initially the problem was categorized through the development of general corrosion shapes, able to describe the vast majority of the deterioration topologies observed at the available inspection reports. Summary sheets were created to include information regarding thickness loss, corroded area dimensions, and locations, in compliance with the developed general shapes. These sheets were populated with the necessary descriptive information for 808 corroded beam ends, sourced from all the inspection reports. Post processing of the data defined the range of variation of the parameters involved in describing the general shapes.

The bounds of the most common corrosion patterns were quantified and reported in two broad categories; beams with and without diaphragms above the bearing. Fig. 4.8 visualizes the bounds of the corrosion patterns, for beams falling under the second category. Patterns 1 to 5 describe areas with thickness reduction, while patterns 6 and 7 describe hole areas projected on the the thickness reduction patterns that where most commonly reported with, based on the conducted analysis.

In this thesis, corrosion patterns 1, 2, and 3, are employed to investigate the effect of section loss, while pattern 6 is used to investigate the effect of holes on the bearing capacity. For each one of the chosen patterns, the associated parameters for web corrosion and their bounds are defined in Fig. 4.8 and Table 4.1 respectively.

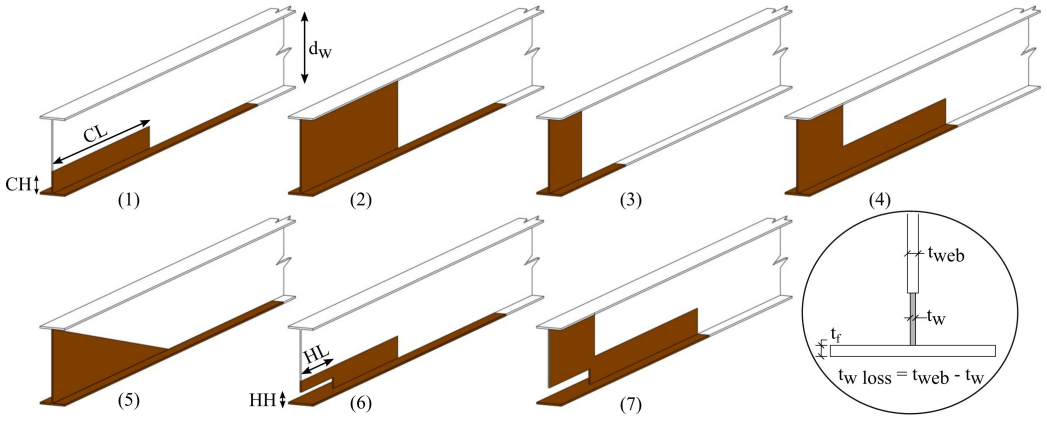

Figure 4.8: The most common corrosion patterns for beams without diaphragms above bearing. The range of variation for the parameters describing patterns 1, 2, 3, and 6 are given in Table 4.1.

The investigation focuses on these four patterns, on the grounds that they describe the majority of the reported corroded ends (171 out of 284 cases) for beams without diaphragms above the bearing. Additionally, all other patterns are subsets of the upper geometrical bounds of the analyzed patterns. To study the effect of web corrosion on girder capacity and to gain a better understanding of the mechanics at the bearing area, flange corrosion has been provisionally excluded from the simulations. For each one of the four examined patterns, a series of scenarios which covers a wide range of variability of the employed parameters is simulated and analyzed under the assumption of uniform section loss.

Table 4.1: Analytical description of the examined corrosion patterns, nomenclature is defined in Fig. 4.8.

Pattern No.	(1)	(2)	(3)	(6)
CH (d_w)	(0, 0.3]	1	[0.15, 1]	(0, 0.3]
CL (d_w)	(0, 1.5]	[1, 1.5]	(0, 0.5]	(0, 1.5]
HH (d_w)	-	-	-	(0, 0.15]
HL (d_w)	-	-	-	(0, 0.5]
$\frac{t_w}{t_{web}}$	[0.2, 0.8]	[0.8, 0.6]	[0.8, 0.6]	[0.2, 0.8]

At this point it should be mentioned that the corrosion height (CH in Fig. 4.8) of the deterioration scenarios is expressed as a fraction of the web depth (d_w in Fig. 4.8). However, the developed numerical model simulates the girder with shell elements at the middle of each section. This approach unavoidably results in a deeper web section equal to half of the flange thickness (t_f) the top and bottom parts of the web, where the web simulated surface intersects with the flanges related surfaces. In order to maintain the corrosion height proportional to the numerically simulated depth (d_n), d_w in Table 4.1 is substituted by d_n, where:

$$d_n = d_w + t_f \tag{6}$$

4.2.1.2 Material Properties

The material properties employed for the parametric analysis are determined based on the conducted tensile tests presented in Fig. 4.3. In detail, a bi-linear elastoplastic constitutive model with hardening is used, with 400 MPa ultimate stress, Fig. 4.9.

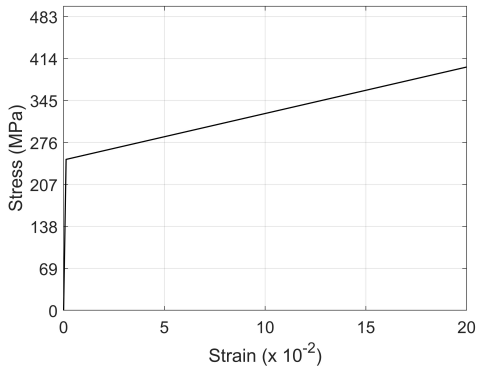

Figure 4.9: Bi-linear elastoplastic constitutive model considered for the parametric analysis.

4.2.1.3 Boundary and Loading Conditions

The numerical model developed in Paragraph 4.1 is slightly modified to replicate the in-service conditions of full length un-stiffened single span beams. Initially, the displacement restrictions at the top flange sections are extended along the whole flange surface to account for the deck contribution. Additionally to the translational degree of freedom, rotations along the longitudinal axis of the beam is also restricted.

Concerning the support area, the bearing plate typically rests on a concrete abutment. The plate is anchored to the concrete, with anchor bolts going through the bottom flange and the plate. However, several of the inspection reports have recorded that anchor bolts are either completely missing or they are severely corroded or bent. To account for the worst case, it was decided that the set of boundary conditions would not include the anchor bolts. Consequently the constraint coming from these bolts is not included in the model.

A dead load equal to 19 kN/m is considered representative of both the self weight of the beam as well as the contribution of the overlying deck, according to tributary areas. Under the condition that dead load is fully applied without corroded end's failure, live loads are based on the HL-93 load check. The HL-93 consists of a three-

axle truck (HS20), or a design tandem, placed for maximum shear, plus the design lane load that is equal to 9.3 kN/m. The lane load is applied as a uniform pressure on the top flange, similarly to the dead load. The truck load tire contact areas cover the full flange width and 51 cm longitudinally. Live load is sequentially increased until the loading carrying capacity of the deteriorated end is reached.

4.2.2 Analysis Results

4.2.2.1 Effect of Initial Imperfection on Load Carrying Capacity

Experiments presented in Chapter 3 revealed that in service deteriorated beams do not necessarily have perfect geometry. The cross section may deviate laterally from the ideal shape as well as from the member's center line from straight. The experimental results highlighted the impact of the initial out of straightness of the web and triggered a detailed numerical investigation to explore the effect of its magnitude to the bearing capacity.

For the numerical simulations the out of straightness of the web is considered by introducing and scaling imperfections into the model based on the eigenmodes shapes. This is consistent with plate theory as imperfection mode shapes are considered among the most deleterious of all imperfection shapes. Each model is initially solved using the eigenvalue buckling analysis algorithm, and the eigenmode that appears at the deteriorated end (the zone of interest) is introduced as an initial geometric imperfection for the quasi-static analysis.

To evaluate the influence of the initial imperfection amplitude (the maximum web deviation magnitude from straightness), corrosion scenarios with varying section loss and corrosion height are employed. Fig. 4.10 shows the relationship between the imperfection amplitude and the bearing capacity for two different corrosion heights. The nominal capacity based on current procedures [7] is also included for a comparison

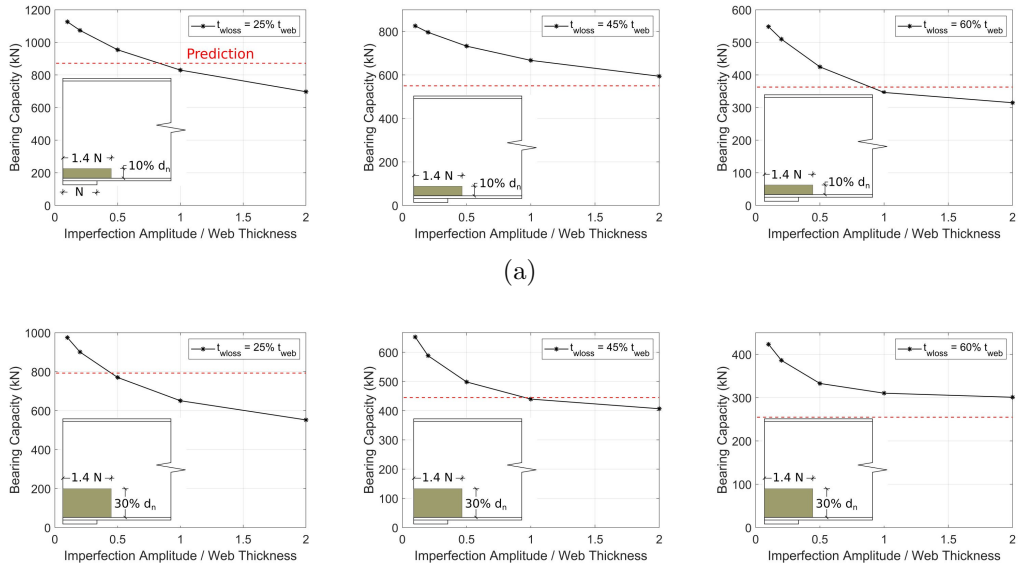

Figure 4.10: Effect of initial imperfection amplitude on the residual bearing capacity of beams with a) $CH = 10\%d_n$; and b) $CH = 30\%\ d_n$. The capacity drop due to the increasing imperfection amplitude reaches up to 43% for the examined scenarios.

between the numerical results and the current Bridge Manual procedures [7]. All captured failures are stability (crippling) related according to the current procedures, where crippling is the local buckling of the lower part of the web.

The key observation from Fig. 4.10 is the big range of capacity drop for increasing imperfection amplitude, which for the examined scenarios varies between 28% and 43%. For both corrosion heights, the capacity tends to plateau for imperfection amplitude equal to around 1 times the web thickness, t_{web}, when the thickness reduction exceeds 60% of t_{web}. For higher remaining material ($t_{wloss} = 25\%\ t_{web}$ or 45% t_{web}), the imperfection governs the failure load. An interesting finding is that it is not possible to conclude on which corrosion scenarios are overestimated by the current procedures, as the observed behavior is dependent both on section loss and damage area dimensions. Based on these inconclusive findings, three different amplitudes: 0.1 t_{web}, 0.5 t_{web} and 1 t_{web} are considered for the rest of this parametric study. This way,

a significant range of imperfection amplitudes are covered enriching the parametric analysis.

4.2.2.2 Effect of Corroded Area Dimensions

A series of numerical analysis are run to study the effect of corrosion characteristics on bearing strength. Corrosion scenarios with varying dimensions and section losses are projected on a 36WF150 girder with imperfection amplitude 0.1 t_{web}, 0.5 t_{web} and 1 t_{web}.

Fig. 4.11 provides evidence of a link between the harming effect of corrosion length and initial girder's imperfection. In detail, for imperfection amplitude 1 t_{web}, if the corrosion length (CL) exceeds the bearing length (N) more than 1.1 times ($CL = 2.1\ N$), it has no further effect on the beam's strength. However, for imperfection amplitude 0.1 t_{web}, the corresponding effective deterioration length is reduced to 0.4 times beyond the bearing length.

In Fig. 4.12, the corrosion height is related with the residual bearing capacity of girders with varying corrosion length (25%, 50%, 150% of d_w or 75%, 140%, 430% of bearing length, N). The results reveal that the harmful effect of deterioration height is inversely proportional to the initial imperfection amplitude. For beams with initial deformation 1 t_{web}, the impact of corrosion height beyond 30% of d_n is decreasing and thickness loss is dominating. However, for scenarios where the deterioration area extends beyond the bearing length and the initial web deviation tends to zero (0.1 t_{web}), the residual strength is continuously reduced for increasing damage height.

4.2.2.3 Effect of Corrosion Holes

Sensitivity analysis with respect to hole length and height (HL and HH in Fig. 4.8, respectively) is conducted for imperfection amplitude 1 t_{web}. To realistically simulate the bearing area of a deteriorated beam, in addition to the hole, 20% material

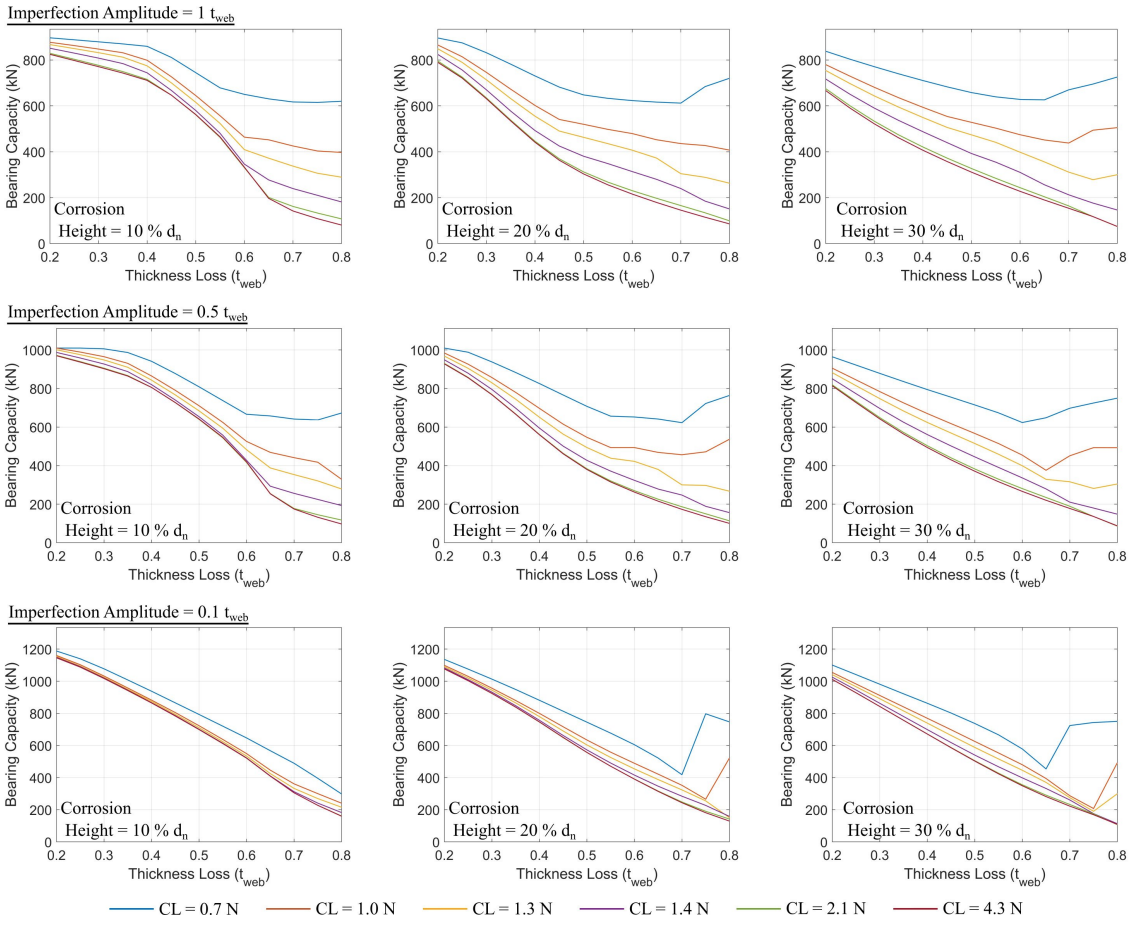

Figure 4.11: Effect of corrosion length for imperfection amplitude in the range of 0.1 to 1 t_{web} and corrosion height from 10 to 30% of depth. There is a strong association between the corrosion length and the initial web imperfection that significantly affects the bearing capacity.

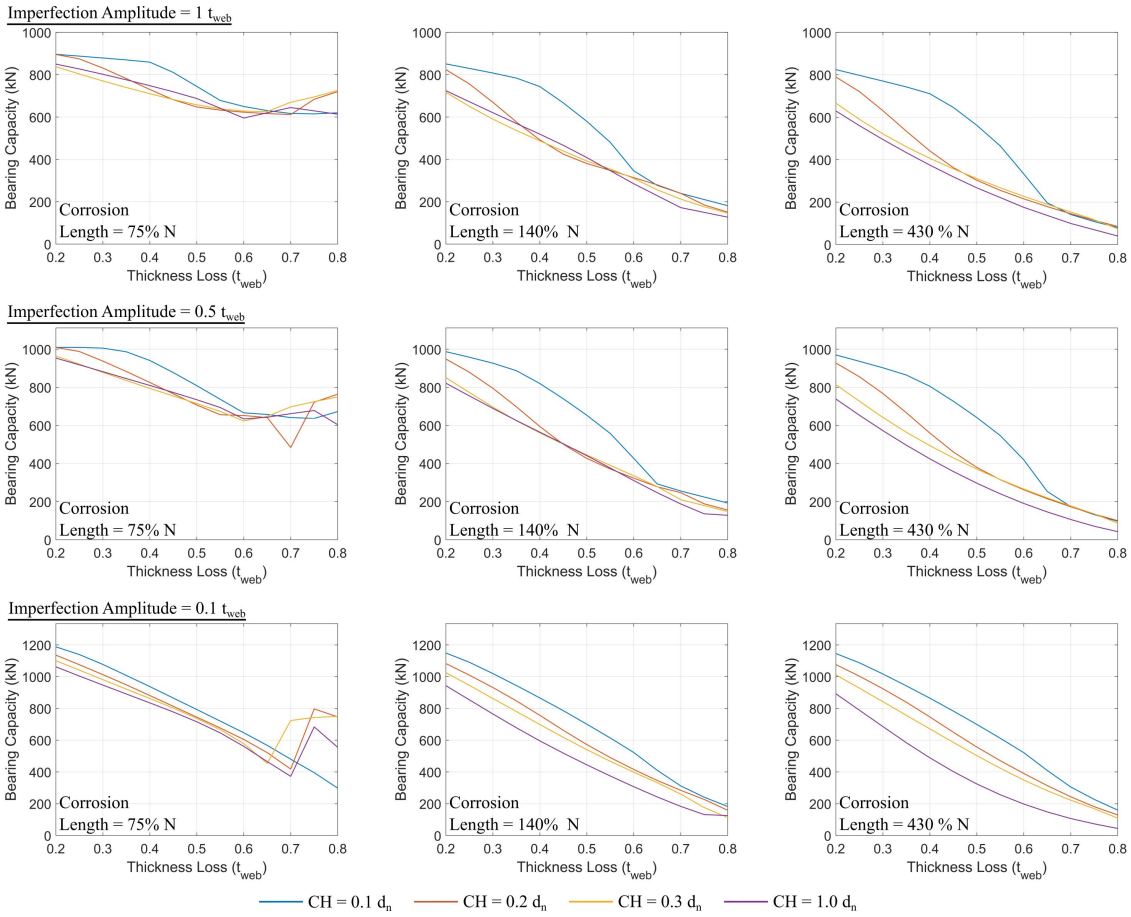

Figure 4.12: Effect of corrosion height for imperfection amplitude in the range of 0.1 to 1 t_{web} and corrosion length from 75% to 430% of the bearing length. The harmful effect of corrosion height beyond 30% of depth is reducing for increasing imperfection amplitude.

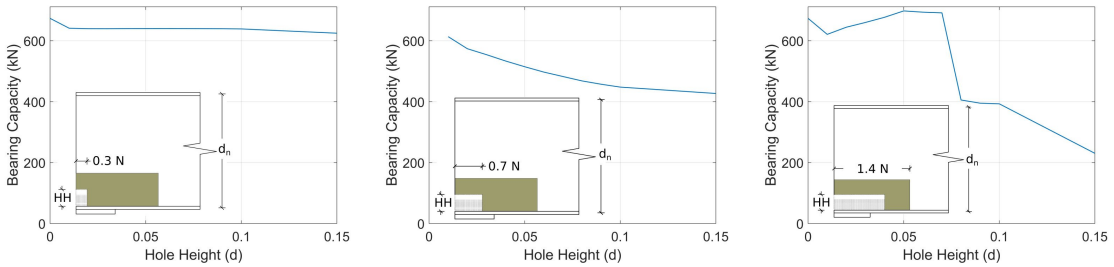

Figure 4.13: Effect of hole's dimension to bearing capacity. Hole height (HH) is examined in the range of 1 to 15% of depth for hole lengths (a) 0.3; (b) 0.7 and (c) 1.4 times the bearing length. In cases were the hole gap closes during loading and the web starts bearing on the flange, the specimen is able to undertake additional load.

reduction is considered for an area with corrosion height 30% of d_n and corrosion length 2.1 times the bearing length (25.4 cm).

In Fig. 4.13 significant correlation is revealed between the effect of hole height on the capacity and the hole length. In detail, if an area with 100% section loss is limited above the outer edge of the bearing, it has no significant effect on the capacity regardless its height, Fig. 4.13a. In the event that the hole extends close to the inner bearing edge (Fig. 4.13b), capacity tends to plateau. An interesting phenomenon is observed for the case where the hole extends beyond bearing length. The results show the counterintuitive behavior of increasing capacity for bigger holes. However this trend is attributed to the web bearing on flange. The hole gap is eliminated, and the specimen is able to undertake additional load. Ultimately a sudden capacity drop is observed, which is correlated to the web failure above the inner hole boundaries.

It is worth noting, that according to the current procedures the total of the scenarios presented in Fig. 4.13c have zero nominal capacity, while the current work reveals that even in the worst-case scenario, up to a third of the capacity corresponding to the non-hole geometry, can be developed. However, this failure mechanism can be observed under the condition of extensive downwards translation of the top flange.

A condition, that is controversial whether it is realistic or not for in-service girders due to the additional stiffness emerging from the deck as well as potential diaphragm existence. Moreover, even if it is realistic, the likelihood is that serviceability issues would result from the extensive deformation.

4.2.2.4 Failure Modes

The deformed shape of corroded beams is mainly affected by the corrosion zone dimensions as well as the thickness reduction. The general picture emerging from the failure modes is that small height damages with section loss beyond 65% of t_{web} result to local failure at the base of the web. Increased remaining material is related to a half buckling wave formulated along the whole depth.

The obtained failure modes were always combined with a web portion in the plastic regime. However, especially for the cases with extensive initial imperfection, it was not possible to justify whether the local yielding had triggered instability or not. Ultimately, the failures can be classified into two broad categories as buckling and crippling phenomena. Buckling modes are characterized by deformations developed along the whole depth, while crippling modes are related to deformations at the corrosion area.

An interesting side finding from Figs. 4.11 and 4.12 is the paradox of increasing capacity for higher material losses. This behavior is limited to cases where the corrosion length does not extend beyond the bearing length. The reduced bending stiffness in combination with the imperfect geometry, result in progressively increased lateral displacements and uplift along the slender corroded area. This uplift results in the reaction force concentration at the inner bearing edge (Fig. 4.14), where the web has experienced no loss, providing additional strength to resist load. Finally, even if the corroded part experiences extensive lateral deflection, buckling occurs only when the

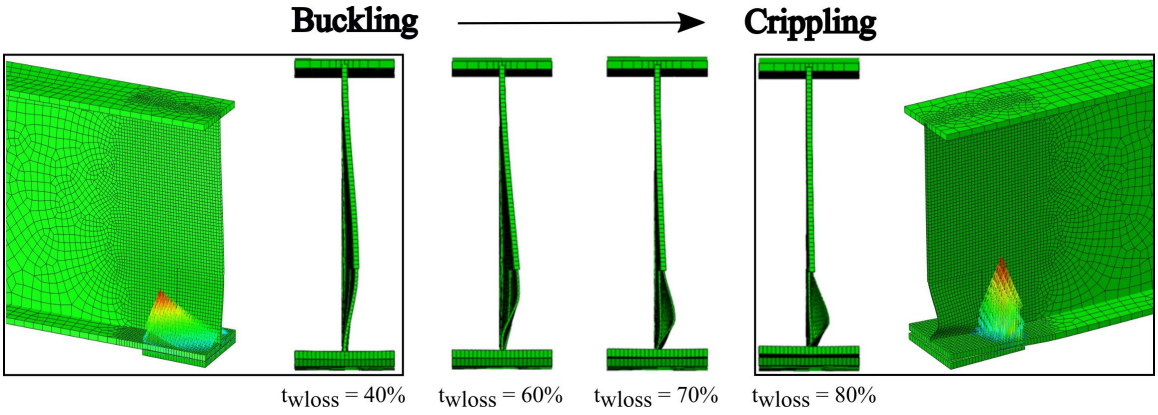

Figure 4.14: Failure modes, and reaction force development for section loss in the range of 40 to 80% of web thickness. Increasing section loss results to localized failure and higher collapse loads.

intact part fails.

4.2.2.5 Effect of Girder Configuration

This section examines whether the findings of the parametric analysis hold independently of the beam geometry and support characteristics. The effect of beam type and length are investigated as well as the length of the bearing plate.

In order to examine the effect of beam type, a series of deterioration scenarios are projected on a 30WF108 and a 36WF150 girder. Bearing lengths are selected to maintain the N/d ratio equal to 3 for both beam types, while the corrosion lengths are expressed proportional to the bearing length maintaining the CL/N constant. This approach allows the researcher to isolate the contribution of beam type on the harmful deterioration effect. The obtained failure loads for each beam type are normalized with respect to the corresponding capacity for section loss 20%. The curves for both beams in Fig. 4.15, follow an almost identical path neglecting the need for multiple beam types investigation for constant N/d ratio.

In order to examine the sensitivity of the bearing capacity on the beam length a set of analyses are performed. In Fig. 4.16 curves with common color denote common

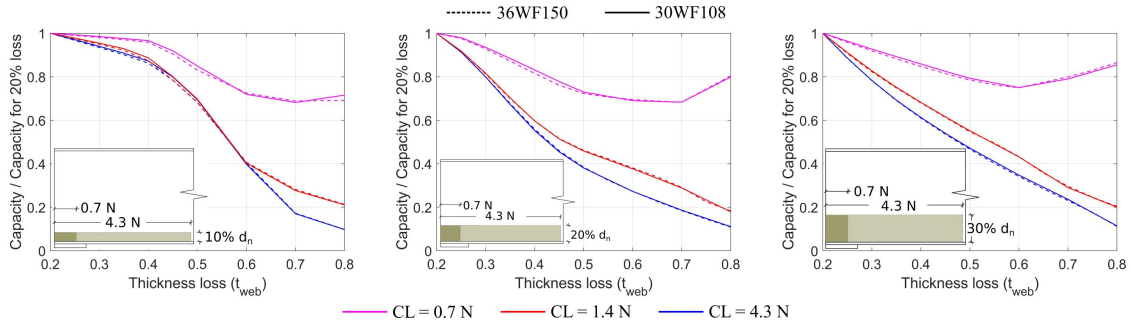

Figure 4.15: Corrosion scenarios projected on two different beam types. The relevant capacity reduction is beam type insensitive for constant N/d ratio.

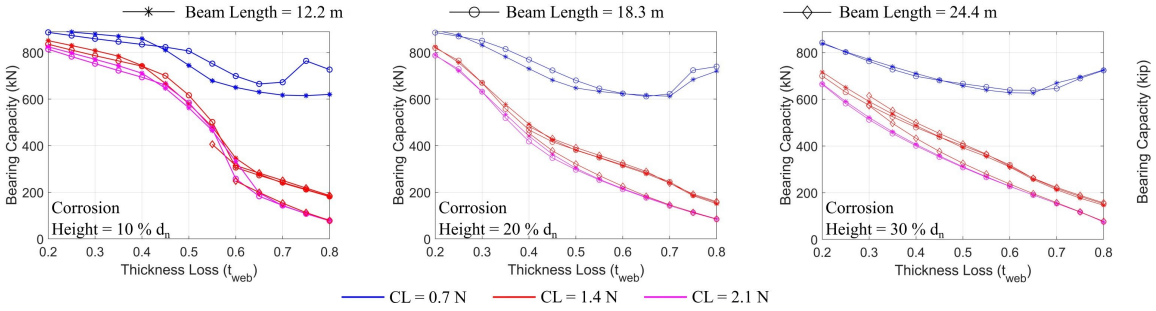

Figure 4.16: Beam length effect on capacity of deteriorated beams. Non significant correlation is observed between the girder length and the bearing capacity.

corrosion length while the marker (diamond, circle or asterisk) denotes the length of the specimen. The corrosion height varies between 10% of d_n in Fig. 4.16a up to 30% in Fig. 4.16c. Based on these figures, no significant correlations were obtained between corroded beam capacities and beam length, excluding this parameter from the upcoming analytical expression.

The last aspect of the girder configuration to examine, is the bearing length. Fig. 4.17 compares the bearing capacity of a girder simulated for consecutively increasing bearing lengths, and corroded areas which always exceed the bearing by a constant ratio (20% of the bearing). Results demonstrate the beneficial role of the bearing length, which dominates the harmful effect of the proportionally increasing corroded area.

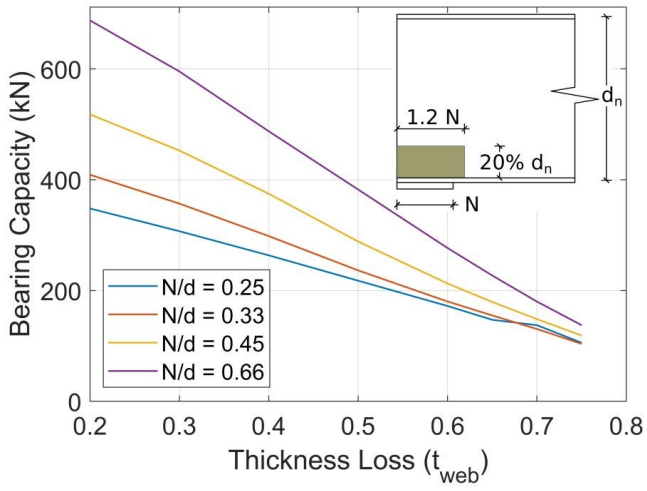

Figure 4.17: Residual capacity of a 21WF59 girder for varying bearing lengths and constant CL/N ratio. The beneficial effect of bearing length dominates the harmful impact of proportionally increasing damage area.

Taken all together, these analyses demonstrated minor impact of beam type and length to the relevant thickness reduction of corroded ends, contrary to the strong association between bearing length and support resistance.

CHAPTER 5

ANALYTICAL FRAMEWORK FOR CAPACITY EVALUATION

5.1 Equations Development

The proposed provisions emerge from the relationship between corrosion characteristics and bearing failure loads of a sample consisting of more that 2000 simulated scenarios. The considered scenarios include the data presented in Chapter 4 enriched with additional scenarios within the range of variability for the parameters describing the patterns 1, 2 and 3 in Fig. 4.8, and for three imperfection amplitudes (0.1 t_{web}, 0.5 t_{web} and 1 t_{web}). The finite element models are created by implementing an in house developed Python script, which operates through the ABAQUS software, assembling suitable meshes and applying the boundary and loading conditions described in Chapter 4.

In [7] the bearing strength assessment of un-stiffened corroded beam ends is calculated on the basis of the yielding and crippling capacities, a detailed description of the procedures can be found in Paragraph 3.5.2. It is worth noting, that for the total of models simulated and analyzed in Chapter 4 of this thesis, as well as for the 6 naturally corroded specimens presented in Chapter 3, all the predicted failure loads were governed by the crippling capacities. Thus, the goal of the third and last phase of the presented numerical work is the development of empirical relationships employing the current crippling equations as well as regression analysis to better fit the numerically obtained capacities. The efforts are focused on beams with overhang length less than $5k$, where k denotes the distance from outer face of flange to web toe

fillet, similar to the actual specimens that the numerical model was calibrated and verified from.

The proposed equations aim to create envelopes for both captured failure modes, crippling and buckling. However, the nominal ultimate bearing load should be estimated as the minimum between the proposed crippling and yielding capacity as currently is, while engineering judgement is always encouraged where section loss exceeds 65% of intact web thickness.

The proposed modifications to the current procedures, are focusing on 4 main aspects: the initial imperfection amplitude, the area over which the average web thickness is determined, and finally the crippling capacity equations for varying N/d ratios.

5.1.1 Initial Imperfection Amplitude

Given the findings described in Chapter 4, regarding the deleterious effect of initial web deviation from straightness, the proposed procedures are developed for three different imperfection amplitudes. When the author studied the deterioration condition of 93 bridges through inspection reports noticed that, in many cases beam type or depth was not reported, in contrast with the as built web thickness. Probably, inspectors were taking an extra measurement at the intact web as benchmark, to evaluate the beam condition in the field. Obviously, construction drawings are available for load rating, however it was preferred to express the imperfection with respect to the web thickness to easier incorporate the application of the proposed procedures to the empirical established inspection techniques. Consequently, the three provided imperfection amplitudes, are denoted as a, and equal to 0.1 t_{web}, 0.5 t_{web} and 1 t_{web}.

5.1.2 Average Web Thickness

The equations that are currently in use for crippling capacity estimation are based on research by Roberts [17] and Elgaaly and Salkar [36] on intact beams subjected to patch loading. The corrosion contribution is considered using an average web thickness t_{ave} instead of the nominal web thickness t_{web} to reflect the reduction in capacity anticipated from corrosion of the web. The average web thickness, according to the proposed procedure, is calculated within the bottom 10 cm of the web height and length $N + md$ (where m factor specified in Table 5.1) from the web edge, according to Eq. (7).

$$t_{ave} = \frac{(N + md - H) * t_w}{N + md} \tag{7}$$

Where:

t_w: remaining web thickness (mm)

H: length of hole along length used for capacity (here: $N + md$) (mm)

N: bearing length (mm)

d: beam depth (mm)

m: factor specified in Table 5.1.

In the event that the examined corrosion scenario does not extend along the whole area considered for the capacity estimation, the weighted average of the thickness within this area is calculated.

Table 5.1: Proposed values of factor m.

Imperfection Amplitude (a)	1 t_{web}	0.5 t_{web}	0.1 t_{web}
N / d $>$ 0.2	0.2	0.2	0.1
N / d $\leq$ 0.2	0.1	0.1	0

5.1.3 Capacity Equation for N/d > 0.2

As has been already mentioned, the current crippling equations constitute the base of the proposed provisions. For exterior supports with N/d > 0.2, the bearing failure load is given by Eq. (8).

$$R_{n,crip} = \ 0.4t_{ave}^2\ [1\ + \left(\frac{4\ (N-H)}{d} - 0.2\right)(\frac{t_{ave}}{t_f})^{1.5}]\sqrt{\frac{EF_y t_f}{t_{ave}}} \tag{8}$$

By comparison of the predicted capacities and the numerically obtained failure loads it was decided to increase the significance of corrosion length by multiplying the right hand side of Eq. (8) by the factor $(CL/(N + m/d))^h$, where CL denotes the corrosion length along length used for capacity estimation, and parameter h is specified in Table 5.2. After algebraic manipulations and the proposed modification, crippling capacity is given by Eq. (9):

$$R_{n,crip} = \ [0.4\ \sqrt{EF_y t_f}\ {t_{ave}}^{1.5} + \ 0.4\left(\frac{4\ (N-H)}{d} - 0.2\right)\frac{\sqrt{EF_y t_f}}{t_f^{1.5}}\ {t_{ave}}^3]\left(\frac{CL}{N + m\ d}\right)^h \tag{9}$$

Linear regression is performed to model the relationship between the average remaining thickness and the crippling capacity. The FEA results are used in combination with linear regression. The numerically obtained capacity of the examined beam end will be imported as $R_{n,crip}$ while the corresponding t_{ave} will be calculated for every corrosion scenario. Thus, Eq. (9) can be expressed as:

$$Y = \ A\ X_1 + \ B\ X_2 \tag{10}$$

A and B are estimated based on at least 312 simulations per imperfection ampli-

tude.

$$Y = R_n \tag{11}$$

$$X_1 = \sqrt{EF_y t_f}\ {t_{ave}}^{1.5}\ \left(\frac{CL}{N + m\ d}\right)^h \tag{12}$$

$$X_2 = [\left(\frac{4\ (N-H)}{d} - 0.2\right)\frac{\sqrt{EF_y t_f}}{t_f^{1.5}}\ {t_{ave}}^3]\left(\frac{CL}{N + m\ d}\right)^h \tag{13}$$

To statistically evaluate the fitness of the model the P-value for coefficient A and B was employed. The P-value for each term tests the null hypothesis that the coefficient is equal to zero (no effect). A low P-value (≤ 0.05) indicates that the null hypothesis can be rejected. Table 5.2 summarizes the proposed constant values as well the corresponding P-values. The values of factor h are also included.

Table 5.2: Linear regression results for beams with $N/d > 0.2$.

Imperfection Amplitude (a)	1 t_{web}	0.5 t_{web}	0.1 t_{web}
Scenarios	381	312	312
A	0.41	0.36	0.6
B	0.19	0.59	0.24
P - value for A	3e-112	2e-55	9e-89
P - value for B	2e-9	4e-29	1e-7
h	0.1	0.4	0.4

Based on comparison with numerically obtained capacities, the statistically obtained coefficients for A and B were uniformly factored by 10% for imperfection amplitude 1 and 0.5 t_{web} and 5% for 0.1 t_{web} to limit capacity overestimation. It is worth noting that the 1005 scenarios of varying corrosion characteristics and imperfection amplitudes were projected on a 36WF150 beam with 30.5 cm (12 in.) bearing

length, ($N/d = 0.33$). In order to increase the significance of the second term which includes the N/d ratio, B is raised to the power of (0.33d/N). The final coefficients for Eq. (14) are presented in Table 5.3, where not a clear pattern is observed for reducing imperfection amplitude. This behavior is attributed to the different equation (varying parameter h) and corrosion input (parameter m) for each imperfection amplitude. Both parameters where defined prior the conducted linear regression analyses. Consequently, even the same corrosion scenarios were examined, coefficients A and B, reflect a unique combination of equation form and corrosion input, for each imperfection amplitude.

$$R_n = [A\sqrt{EF_y t_f}\, {t_{ave}}^{1.5} + B^{(\frac{0.33d}{N})} \left(\frac{4\,(N-H)}{d} - 0.2\right) \frac{\sqrt{EF_y t_f}}{t_f^{1.5}}\, {t_{ave}}^{3}] \left(\frac{CL}{N + m\,d}\right)^{h} \tag{14}$$

Table 5.3: Proposed coefficients for Eq. (14).

Imperfection Amplitude (a)	1 t_{web}	0.5 t_{web}	0.1 t_{web}
A	0.37	0.32	0.57
B	0.17	0.5	0.23
h	0.1	0.4	0.4

5.1.4 Capacity Equation for N/d $\leq$ 0.2

Similarly to the previously described procedure, the base for the proposed provisions remains the crippling capacity equation, which for beams with $N/d \leq 0.2$ is given by Eq. (15).

$$R_{n,crip} = \ 0.4t_{ave}^2 \ [1 \ + 3\left(\frac{(N-H)}{d}\right)(\frac{t_{ave}}{t_f})^{1.5}]\sqrt{\frac{EF_y t_f}{t_{ave}}} \tag{15}$$

The right hand side of Eq. (15) is multiplied by $(t_{ave}/t_{web})^h$ in order to asses the overestimation of numerically obtained capacities for section loss above 60% of intact web thickness. After algebraic manipulations the capacity equation is rewritten as:

$$R_n = \ 0.4\sqrt{EF_y t_f}\ (\frac{t_{ave}}{t_{web}})^h\ (t_{ave})^{1.5} + 1.2\left(\frac{(N-H)}{d}\right)\frac{\sqrt{EF_y t_f}}{t_f^{1.5}}\ (\frac{t_{ave}}{t_{web}})^h\ (t_{ave})^3 \tag{16}$$

In addition, the exponent of t_{ave} at the first term of Eq. (16) is reduced from 1.5 to 1.2 to better fit the numerical results. Linear regression is performed to determine the values of coefficients C and D at the right hand side of Eq. (17).

$$R_n = \ C\sqrt{EF_y t_f}\ (\frac{t_{ave}}{t_{web}})^h\ (t_{ave})^{1.2} + D\left(\frac{(N-H)}{d}\right)\frac{\sqrt{EF_y t_f}}{t_f^{1.5}}\ (\frac{t_{ave}}{t_{web}})^h\ (t_{ave})^3 \tag{17}$$

The regression output is given in Table 5.4, where for imperfection amplitude 0.5 t_{web} the P-value for coefficient D is slightly higher than the acceptance standards (<0.05), but yet close to them. Both the sign and magnitude are realistic, thus ultimately the coefficient is accepted and factored by 10% to create an envelope below the FEM results. On the other hand, for imperfection amplitude equal 1 and 0.1 t_{web}, the P-values for coefficient d are out of the acceptance limits (<0.05), thus the respective second term in the parenthesis in Eq. (17) is removed as statistically insignificant, and linear regression is repeated considering only the contribution of the first one. Summarizing, the capacity of beams with corroded ends with $N/d \leq 0.2$ is given by Eq. (18).

$$R_n = [C\sqrt{EF_y t_f}\ \ (t_{ave})^{1.2} + D\left(\frac{(N-H)}{d}\right)\frac{\sqrt{EF_y t_f}}{t_f^{1.5}}\ (t_{ave})^3]\ (\frac{t_{ave}}{t_{web}})^h \qquad (18)$$

With C, D and h from Table 5.5.

Table 5.4: Linear regression results for beams with $N/d \leq 0.2$.

Imperfection Amplitude (a)	1 t_{web}	0.5 t_{web}	0.1 t_{web}
Scenarios	312	312	312
C	0.37	0.35	0.4
D	0.04	0.19	0.04
P - value for C	2e-170	3e-175	5e-163
P - value for D	0.95	0.05	0.77
h	0.4	0.2	0.15

Table 5.5: Proposed coefficients for Eq. (18).

Imperfection Amplitude (a)	1 t_{web}	0.5 t_{web}	0.1 t_{web}
C	0.33	0.32	0.38
D	0	0.17	0
h	0.4	0.2	0.15

5.2 Validation

Initially, experiments conducted by the author and Wu et al. [25] are employed to evaluate the performance of the proposed provisions (Table 5.6). The girders tested

and presented in Chapter 3 had a variety of deterioration at their ends. Out of the 6 field corroded specimens, 5 of them had holes above the support. The parametric analysis conducted in Chapter 4 explicitly investigated the effect of corrosion holes. However the observed failure mechanisms were associated with extensive vertical deformations, a behavior that is controversial whether is realistic or not on in-service girders. Thus the proposed provisions were not designed to modify the method of hole inclusion in the methodology for the residual strength evaluation, and therefore the impact of this work for these specific cases is estimated to be minimal. The only specimen which did not have a hole is Specimen 2, and consequently this is the unique specimen utilized to examine the efficiency of the proposed methodology.

Although a detailed description of Specimen 2 is included in Chapter 3, it is worth noting the flange hole at the support area as well as the out-of-plumbness condition of the web. The pre-test measured imperfection (2.7 t_{web}) significantly exceeds the imperfection bounds (0.1 - 1 t_{web}) that the proposed provisions were calibrated for. However, it can be inferred from Fig. 5.1 that they notably reduce the discrepancy between the experimental and the estimated capacity, demonstrating the improved effectiveness that they offer.

Wu et al. [25] artificially reduced the thickness at the support area of specimens with d=600 mm, t_f=16 mm, b_f=200 mm, t_{web}=10.6 mm. Finally, the distance from the outer face of flange to web toe fillet equals 31 mm. The corrosion patterns were rectangular shaped, located at the web bottom similarly with the numerically simulated scenarios by the researcher. The specimens nomenclature follows the N#-W-L#T# pattern, where N represents the bearing length, W the web corrosion, L and T denote the corroded length and thickness respectively. The corrosion height is constant to 100 mm. The instrumentation configuration allowed for recording only the applied at mid-span load, therefore the capacity is estimated as twice the capacity

of the corroded end.

The beams were manufactured according to modern fabrication techniques, thus the parameters for 0.1 t_{web} are considered to reflect the prior-test web deviation from the ideal shape. Results presented in Fig. 5.1 illustrate that the proposed procedures result in improved estimations for the six out of the seven specimens tested by Wu et al. [25]. As it has already been mentioned, to avoid overestimating predictions, the proposed provisions were calibrated to create an envelope below the numerically obtained capacities. Consequently, in some cases improved but still conservative estimations are expected. This behavior is captured for Specimens 6, 7, 8. For Specimen N80-W-L100T4 the current provisions provided a more accurate estimation.

Table 5.6: Specimens utilized for evaluation of the proposed procedures.

ID	Specimen	t_{loss}	f_y	N/d	a
		t_{web}	MPa		t_{web}
1	Specimen 2	40%	317	0.36	1
2	N80-W-L100T4	41%	365	0.13	0.1
3	N80-W-L200T4	40%	365	0.13	0.1
4	N80-W-L300T4	40%	365	0.13	0.1
5	N80-W-L200T6	59%	365	0.13	0.1
6	N160-W-L200T4	40%	359	0.27	0.1
7	N160-W-L300T4	39%	359	0.27	0.1
8	N160-W-L200T6	58%	359	0.27	0.1

The capacity predictions for both the current and the proposed methodologies are evaluated with the Mean Squared Error (MSE) defined as:

$$MSE = \frac{1}{n}\Sigma_{i=1}^{n}\left(y_i - \hat{y}_i\right)^2 \tag{19}$$

Where:

y_i: experimentally obtained capacity for the ith specimen

$\hat{y}_i$: predicted capacity according to the current or the proposed provision for the ith specimen

n: number of specimens.

Making use of Eq. (19), the predicted capacities according to the proposed procedures result to 39% reduced error compared to the current provisions. It is also worth noting that the capacity of Specimen 2 is overestimated by both methodologies, however the proposed work provides a significantly improved estimation.

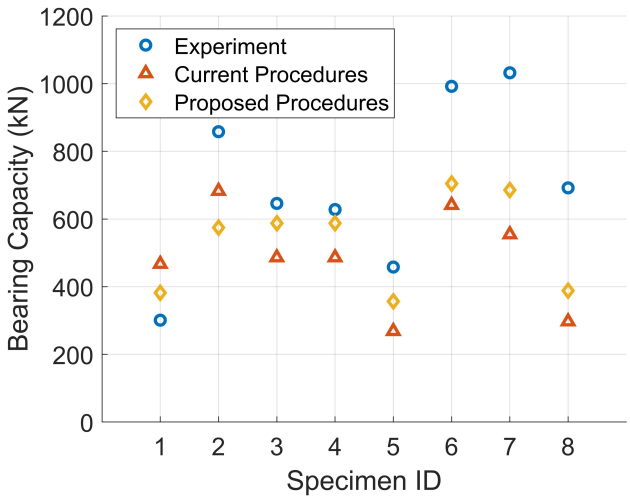

Figure 5.1: Comparison between predicted failure loads and experimental results for specimens in Table 5.6. The proposed procedures provide improved estimations in 7 out of the 8 cases.

The efficiency of the proposed closed form equations has been also demonstrated through experiments conducted by Javier E. [6], who tested 17 naturally corroded specimens. The tested girders covered a wide depth range between 20 cm and 53

cm, and the obtained capacities are presented in Fig. 5.2, alongside with prediction according to 7 different evaluation methods. Failure loads acquired making use of the prediction tools developed in this Chapter are labeled as "Tzortzinis", and they much more closely follow the experimental value trend. It is worth noting that the obtained values are located above the the diagonal line, which signifies more conservative results. On the other hand, estimations with the remaining procedures not only provide a reduced level of accuracy, but they also significantly overestimate the experimentally obtained capacities.

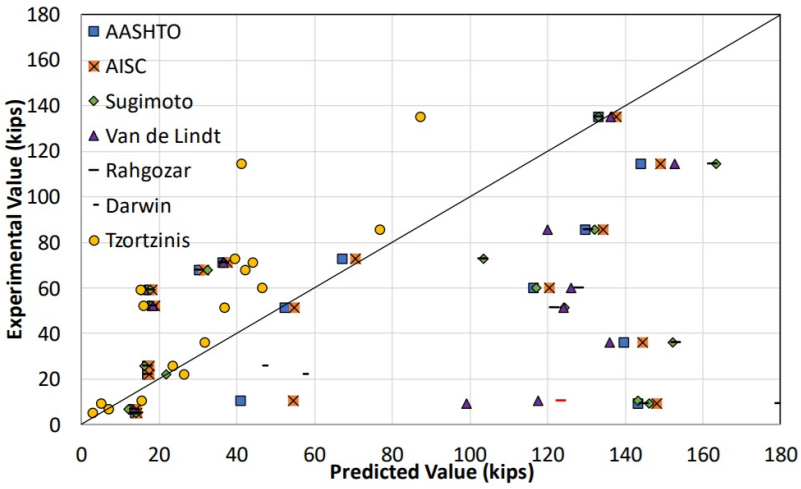

Figure 5.2: Comparison between predicted failure loads and actual capacities of specimens tested by [6]. Figure obtained from [6].

CHAPTER 6

SUMMARY, CONCLUSIONS AND FUTURE WORK: PART I

6.1 Summary and Concluding Remarks from the Experimental Work

The first part of this thesis has focused on providing analytical tools for the structural integrity evaluation of rolled un-stiffened girders with corroded ends. In this effort, experimental, computational and analytical aspects have been developed. The conducted experiments addressed a major long standing gap in the literature: the lack of real corrosion data. In total 6 girders obtained from two highway bridge rehabilitation projects in the state of Massachusetts were used, marking the first time that real field corroded rolled girders were tested in the laboratory.

- In general, steel surfaces with corrosion induced damage are topologically non-uniform and highly uncertain. To quantify the section loss, contour maps depicting the remaining thickness were developed based on a plethora of point measurements obtained with an ultrasonic thickness gauge. Observation of the derived contour maps, as well as visual inspection of the tested specimens indicated that girders retrieved from the same bridge appeared to have common web deterioration patterns due to the in-service bearing area configuration.

- Comparison between experimentally and estimated failure loads highlighted significant weaknesses regarding the efficiency of the current policies for bearing capacity evaluation. Out of the six specimens, one case was overestimated by

36% and four were significantly underestimated by the current procedures. Web holes is the common characteristic of all the underestimated specimens.

- An alternative load path at bearing was revealed for beam ends with long holes located directly above the bottom flange. In two cases, the top edge of the web hole began bearing against the bottom flange, allowing part of the applied load to be transferred to the support. However, the activation of this load path is associated usually with large vertical deflections, which in case of in-service girders could pose a serviceability problem due to potential deflection of the deck.

- One of the obtained failure modes was strongly affected by the initial lateral web imperfection. This type of imperfections is not currently considered in the manual procedures and that is the reason that the procedures significantly overestimated the capacity of this beam. This test was particularly important since it showed that this initial lateral web imperfection severely affects the capacity of the beam end. Although this finding is consistent with basic plates or shells theory, it is not part of the existing procedures or the current inspection protocol.

- Inspection reports of structurally deficient bridges in the state of Massachusetts reveal the existence of in-service girders with signs of buckling at the support area. To explore their structural behaviour, unloading - loading was performed is the post buckling regime of two specimens, with the resulting applied load - displacement curves following an almost identical path. This finding potentially explains why in-service beams in similar condition are able to undertake transient vehicular loads.

6.2 Summary and Concluding Remarks from the Computational and Analytical Work

Following the conducted experiments, the computational and analytical work aimed to clarify and ultimately to encapsulate in the form of concise closed form equations the relationship of corrosion characteristics and the remaining capacity of deteriorated beam ends. Initially, the experimentally obtained data, were implemented to verify a finite element model capable of predicting the capacity of beam ends. Making use of the model, an extensive parametric analysis was performed and numerous combinations of corrosion topologies and beam geometries were simulated and analyzed, defining the parameters with influencing effect on the residual strength of corroded ends. Finally, building on this knowledge predictions tools were fitted on the computationally obtained data points.

- The developed finite element model integrated the uneven section loss, the web deviation from planeness and the interaction between the bottom flange and the bearing plates. Comparison of numerically and experimentally obtained results provided credibility to the finite element model with the failure loads of the two simulated specimens captured with error of 3.5% and 1.1% respectively.

- The analyses output confirmed the experimental findings regarding the deleterious effect of web deviation from straightness to the load carrying capacity. The need for the initial web imperfection effect investigation emerged from measurements performed on girders obtained from bridge demolition projects.

- The effect of deterioration length exceeding the bearing was found to have reducing effect for reducing imperfection amplitude. Regarding the effect of deterioration height, its harmful effect was inversely proportional to the initial

imperfection amplitude.

- Significant correlation was revealed between the hole height and length of orthogonal shaped holes located at web bottom initiating from the outer edge. In cases where the hole exceeds the bearing, the girder was able to undertake notable load, due to the web bearing on flange. This mechanism validates the experimental observations. However, this behavior is correlated with extensive vertical displacements, which in case of in-service girders could pose a serviceability problem due to potential defection of the deck.

- The crippling equations that are currently in use for capacity assessment, were modified to create an envelope for two types of observed failures, crippling and buckling. Predicted loads according to the established and proposed procedures were compared with experimentally and numerically obtained loads, providing overall improved predictions in terms of accuracy.

6.3 Outlook and Future Work

Every aspect of Part I emerges from real corrosion data. Nevertheless, there are still some limitations as well as some open problems. The investigation efforts were focused on the girder, while the deck contribution was simulated by the applied boundary conditions. Good understanding was gained for the corroded beams' behavior. However, the physical absence of both deck and diaphragm from the experimental configuration have potentially conservatively affected the findings regarding stiffness, uplift, and reaction force distribution along the bearing. Future studies will have to examine the behavior of the corroded beams as part of the whole bridge and the potential redistribution of forces after the failure (or even the loading) of one beam end. The system behavior of the bridge is hugely important, and it is expected to

provide more capacity, although this remains to be validated.

For some specimens, the web holes were located at the bottom of the web above bearing. After the initiation of the loading process, the upper web hole edge began bearing at flanges, and the specimens were able to retain significant additional loads. However, this failure mechanism can be observed under the condition of extensive downwards translation of the top flange. This condition is considered controversial for in-service girders, due to the additional stiffness emerging from the deck as well as potential diaphragm behavior. This is an area for future study, and it also related to the system behavior of a full bridge, highlighting the need for bridge level investigation.

The developed closed form equations were validated both experimentally and numerically from the author, as well as from other researchers [6]. Even though the proposed provisions proved significantly more efficient compared to other procedures, there were not designed to modify the method of hole inclusion in the methodology currently found in [7]. A future extension of the current study should analytically address this limitation and further increase the impact of the developed closed form equations to beam ends with corrosion induced holes above the support.

Except for the above mentioned future areas of study, two open problems are addressed in this thesis. The proposed provisions consider the corrosion contribution using a unique thickness value, usually provided by a single point measurement taken by an inspector in the field. Given that section loss is not uniform along the corroded regions, the selected points where measurements are taken to be representative of the beam's condition is currently dependent on the inspectors judgment. However, to increase the efficiency of load ratings, as well as to solidify a comprehensive inspection protocol, the need of an objective methodology emerges. Part II explores the use of 3D laser scanning technology for corrosion data acquisition and post-processing.

Part I focused on un-stiffened rolled girders. Nevertheless, simple span bridges with plate girders constitute a significant fraction of the structurally deficient bridges in the State of Massachusetts. Part III applies the methodology presented in Chapters 3 to 5, to plate girders with corroded ends, developing analytical expressions for load bearing capacity evaluation.

PART II:

DEVELOPMENT OF A 3D LASER SCANNING FRAMEWORK FOR CAPACITY ASSESSMENT OF CORRODED GIRDERS

CHAPTER 7

LITERATURE REVIEW AND OBJECTIVES

7.1 Opening Remarks and Literature Review

To assess the structural condition of corroded simple span steel bridges, associated agencies require first the documentation and quantification of the phenomenon. In most cases, inspectors have to overcome accessibility challenges and trouble instrument readings of single point measurements to describe varying thicknesses over a planar surface, using mainly thickness gauges and calipers. Another challenge in this process is that the phenomenon of corrosion on steel members is topologically non uniform and highly random. Unavoidably, if this type of documentation is not combined with a plethora of measurements, it may not describe the member's condition adequately which makes it more difficult to evaluate the structural condition of the member and ultimately of the bridge superstructure.

As an alternative, 3D laser scanning technology provides rapid 3-dimensional spatial data acquisition and has the potential to address the limitations of the conventional inspection techniques. Terrestrial laser scanners (TLS), also referred to as terrestrial LiDAR (light detection and ranging) collect dense point clouds enabling a digital reconstruction of the actual surfaces. This capability enables the implementation of 3D scanners in numerous applications in engineering [37–39], ranging from the evaluation of a tunnel's deformation [40], to the extraction of sidewalk inventory [41]. In bridge engineering, point cloud data have been employed to measure deformation [42–46], to digitize the structure's geometry [46–52] or for inspection [53–59].

In detail, an early study by Zogg and Ingensand [42] proposed the use of laser scanner to estimate the vertical deflection of a bridge under load. The obtained ver-

tical displacements detected by TLS and by precise leveling were in the same range. Yang at al. [43] conducted a 3-point bending test of a concrete slab to compare the displacements captured by TLS with the deflections estimated by a finite element model, and the observed difference was less than 5%. Moreover, Park et al. [44] tested a 4 m long steel beam and the maximum deflection recorded by TLS was within 1.6% of those measured directly by a linear displacement transducer. Miśkiewicz et al. [45] employed laser scanning to examine whether vehicle impacts resulted to permanent deformations along a prestressed concrete bridge. The comparison between the struck bridge and a reference viaduct did not reveal significant displacements. Finally, Riveiro et al. [46] obtained a good agreement for the minimum underclearance magnitude estimation between laser scanners and a total station's output.

Ross et al. [47] used a laser scanner to provide the as-built records for six historic timber bridges. A comparison between digital and traditional measurements resulted to a mean error of 1.01 mm to 2.02 mm. Lubowiecka et al. [48] scanned and modeled a medieval masonry bridge, while Minehane et al. [49] performed finite element analysis to assess the as-built condition of a cast iron under-arch bridge constructed in 1851. Conde-Carnero et al. [50] presented an automated methodology to converse point clouds to a finite element model. In that study, a footbridge was modeled and assessed under design load. Moreover, Gyetvai et al. [51] introduced a workflow to generate the geometry of bridges for computational analysis. An wrought iron bridge was scanned and numerically assessed under loading scenarios based on the AASHTO [60] regulations. Bautista-De Castro et al. [52] performed laser scanning of a reinforced concrete bridge to ultimately calibrate a computational model for structural condition assessment.

For the inspection of damaged bridges, the RGB colors associated to the corresponding data points were used by Truong-Hong et al. [53] to identify the crack

pattern on concrete. Point clouds and image processing have been combined by Valenca et al. [54] in a procedure to automatically measure the orientation and the cracks dimensions. Another work on concrete bridges by Teza and al. [55] presented an automatic recognition method of surface damages related to mass loss, while a methodology by Kim et al. [56] enables the identification and quantification of spalling defects that are larger than 3 mm in both depth and length. For corrosion induced deterioration along steel members, an early study by Shen et al. [57] employed coating images to detect rust defects based on a methodology which combines color image processing and the Fourier transform. Kushwaha et al. [58] combined laser scanning and close-range photogrammetry to conduct surface analysis detecting corrosion. Finally, Hain et al. [59] employed a portable 3D scanner to create digital representations of actual corroded steel girders both in the laboratory and in the field. Although research has explored point cloud data for the detection and for the quantification of section loss due to corrosion, no study to date has validated these estimations, by comparing data obtained using different techniques, nor have 3D laser scanning data been used to improve estimates for corroded bridge beam ends rating.

7.2 Objectives and Outline

Part II aims to address the shortcoming of conventional data acquisition techniques noticed in the inspection reports of steel bridges by exploring the use of 3D laser scanning technology for bridge inspection and evaluation. As a proof of concept, in Chapter 8, 3D laser scanning is used to measure thickness losses on steel girders. A corroded un-stiffened rolled girder is scanned and the obtained point clouds are post-processed to estimate the remaining material. The developed methodology is validated with measurements taken with an ultrasonic thickness gauge. Contour maps depicting the remaining thickness along the girder are proposed as a documentation

technique that could be integrated in the inspection reports. In Chapter 9, a naturally corroded girder is scanned before it it subjected to full-scale 3 point bending to obtain the load and mode of failure. In Chapter 10 the experimentally obtained results constitute the benchmark to assess capacity estimations derived from finite element modeling and closed form equations. In both cases, the corrosion condition is taken into account by extending the methodology developed in Chapter 8, demonstrating the high potential utility of 3D laser scanning technology for inspecting corroded steel bridges. Finally, Chapter 11 summarizes the research accomplishments of Part II, presents the conclusion and provides suggestions for research directions in the field of bridge inspections making use of 3D laser scanning technology.

CHAPTER 8

MAPPING CORROSION INDUCED SECTION LOSS

8.1 Equipment

Measurements were collected employing a RIEGL VZ-2000 LiDAR [61]. This instrument integrates three primary components: the LiDAR sensor, the precise positioning system, and the camera system. The LiDAR sensor is used to acquire the point cloud that generates up to 400,000 points/sec. The integrated precise positioning system (GPS/IMU) is used to acquire accurate coordinates from a global positioning system (GPS) and an inertial measurement unit (IMU). The camera system is used to capture video log images which are calibrated and integrated with the LiDAR sensor that captures high-resolution imagery.

In the framework of 3D laser scanning two main technologies are found, laser scanners and structured laser scanners. Explicitly analyzing the differences of these two technologies is out of the scope of this work. However it is worth mentioning that while laser scanners operate by projecting a laser point onto the object and measure its reflection, structured laser scanners project a pattern of light. Commercially available portable structured light scanners can provide up to sub-millimeter point accuracy. Nevertheless, due to the sensitivity to the lighting conditions, as well due to the limitations of the working distance, these instruments were not preferred in the current work.

A desktop computer with i7-7700 CPU at 3.60GHz and 32 GB RAM memory was employed for the post-processing of the acquired data. A discrete graphic card that is dedicated for 3D rendering is recommended for point cloud processing.

8.2 Data Collection

The 3D laser scanning experiment was conducted with a naturally corroded steel girder which was acquired from a decommissioned bridge, referred as Bridge B in this thesis, built in 1939 in the state of Massachusetts. A detail description of the structure, as well as construction drawings can be found in Chapter 3. Briefly, it is worth saying that the superstructure was comprised of rolled 53 cm deep WF beams spanning approximately 6.1 m over a single span.

To scan the web surface, the girder was placed in simply supported conditions at 90 cm from the strong floor in the Brack Structural Laboratory at UMass. A unique scan from each one of the two ground stations capturing both sides of the web, was performed. Each scan lasted approximately 5 minutes capturing a 360° view of the field. The laser scanner provides the ability to perform scans without the use of a laptop or external storage device, by storing the acquiring data at an internal memory.

To resemble the actual challenges that inspectors have to face in the field, even though the whole beam was scanned, specific criteria for the selection of the web area that would be employed to evaluate the thickness estimations were set. In detail, the followings requirements should be satisfied:

- The web region should contain mixed areas having intact and corroded regions.
- The web region should contain mixed areas with and without coating.
- The web region should have areas with steel delamination.
- The web region should exhibit different levels of section loss.

Based on these defined criteria, after scanning the whole beam a rectangular web area with dimensions 45.7 cm by 35.6 cm was selected close to midspan. Fig. 8.1

depicts its location as well as the actual condition of both web faces before and after mud, coating and rust were removed.

8.3 Post Processing

Following the points extraction from the scanner, various processing steps followed. Initially, to improve the workability of the obtained files, points capturing irrelevant objects were manually selected and removed. Making use of automated cleaning, isolated points commonly found close to objects edges were erased. Then, non-co-planar reflective and corner points distributed across the lab were used to register the two point clouds in one local coordinate system. The procedure up to this point was carried out using the free source software CloudCompare [62].

Having registered the data from the two scan positions, points which fell into the domain of interest were isolated. The number of points along the web surface is determined based on two parameters; the angular resolution of the LiDAR (horizontal and vertical) and the distance from the measured surface. For each web surface, around 10,000 points were ultimately utilized for the area of interest. A mesh was built and then smoothed for each web face based on Delaunay triangulation. Subsequently, one side acts as the reference and the other as the compared mesh. The distances between the vertices of the compared mesh with respect to the reference mesh were computed and the obtained values, which correspond to the thickness of the section, were extracted as a scalar field associated to the reference mesh's points.

In order to scale down the problem by reducing the number of the involved parameters from 4 (x coordinate, y coordinate , z coordinate, thickness) to 3 (x coordinate, y coordinate, thickness), a plane was fitted to the reference side. To avoid manually selecting points that may not reflect the best fitting plane the least squares solution was preferred. The mesh is rotated in space to position the newly introduced plane

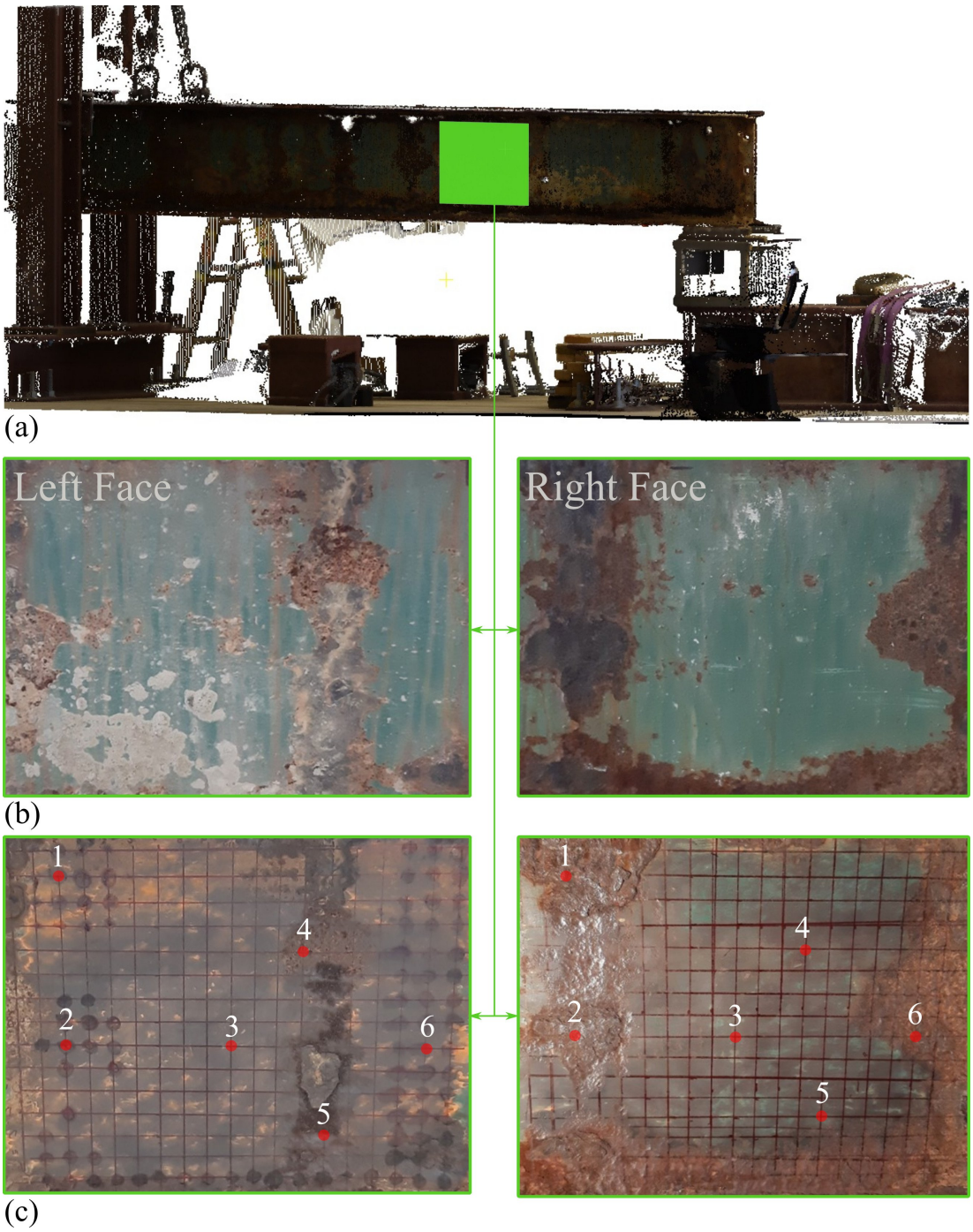

Figure 8.1: a) The scanned girder obtained from Bridge A. The rectangular area (in green) selected for thickness measurements is illustrated b) prior and c) after steel was exposed. Thickness estimations for points 1 to 6 are presented in Fig. 8.3.

in parallel to the xy plane originally set by the laser scanner orientation, and the z coordinate of each point was replaced by the previously calculated corresponding thickness. The resulting x, y, z data were employed to create contour maps depicting the remaining material along the examined domain, Fig. 8.3b. A visual representation of the method is depicted in Fig. 8.2.

8.4 Validation

Detailed thickness measurements were performed in the selected region to determine the section loss using a thickness gauge (D-meter) with a resolution of 0.025 mm, by GE Inspection Technologies [31]. This equipment is widely used by bridge inspectors in general, and its operation is based on measuring the speed of an ultrasonic sound pulse which travels through the material. This process requires a coupling layer to be applied directly on the steel. Consequently, a hammer is usually employed in the field to locally reveal the metal at the positions where measurements are obtained. A grinder was used to remove loose scale and paint in the area where data points were taken with the D-meter.

Even though the thickness gauge is placed on a clean surface, a challenge of this method is varying instrument readings. A common aftermath of the uneven section loss is bumpy steel surfaces which result in a significant variation of the measured thickness. To eliminate problems with local surface imperfections, and for reference to the thickness loss data, a grid with 2.5 cm spacing was drawn on both web faces, and combined measurements from both faces were obtained from 283 locations, Fig. 8.1c.

Since the two approaches study the same area of the web, the acquired data points were used to create contours (Fig. 8.3a), which can be directly compared with the point clouds output (Fig. 8.3b). In addition to the visual comparison, there was

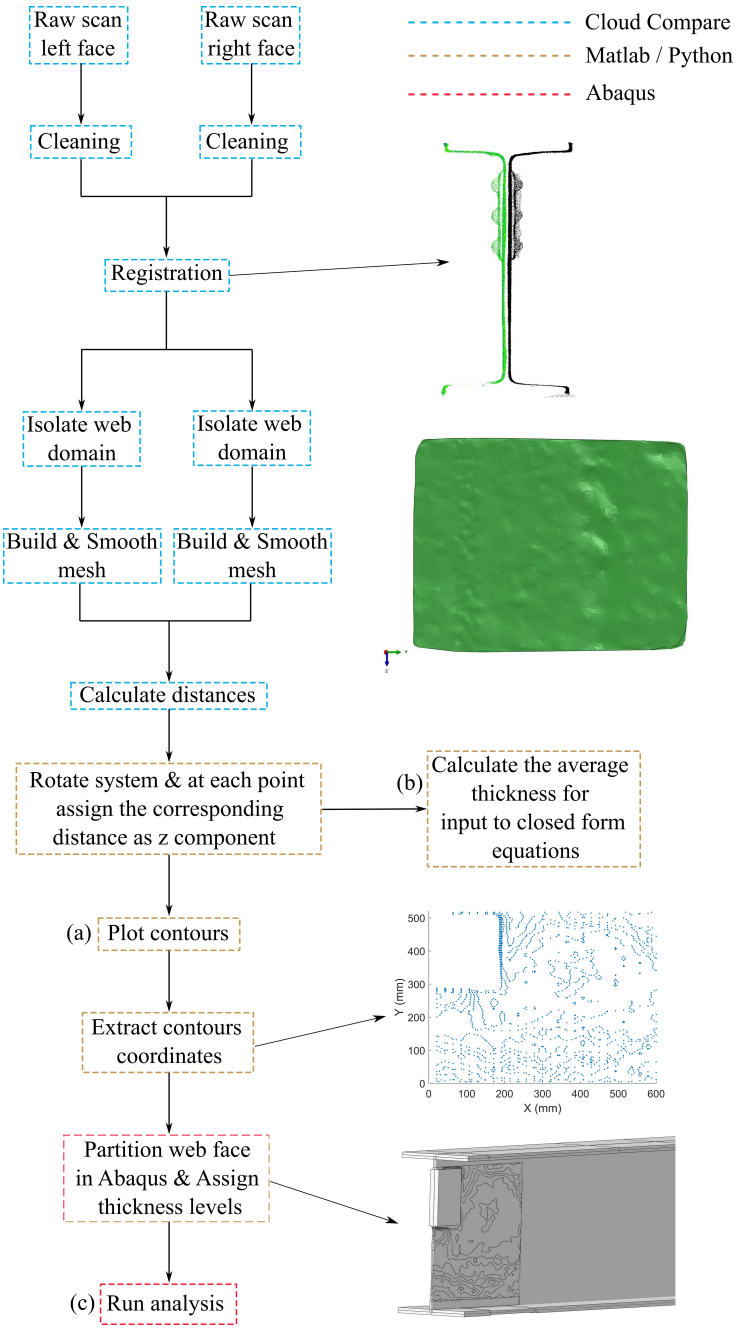

Figure 8.2: Point cloud data processing methodology for a) thickness estimation, b) analytical and b) computational capacity assessment.

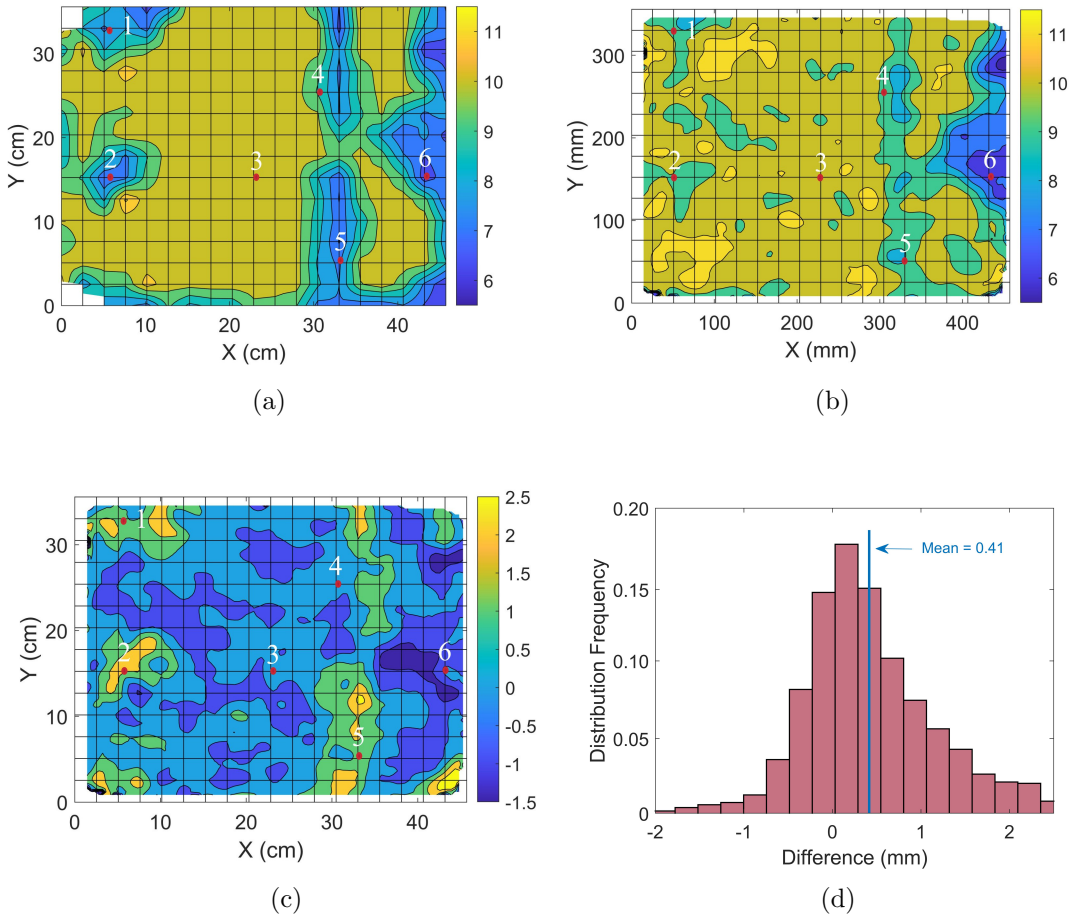

Figure 8.3: Contour maps illustrating a) the remaining thickness estimation based on ultrasonic thickness gauge and b) point cloud data. c) Difference between (b) and (a), and d) the corresponding statistical distribution. The displayed thickness values are in mm.

also in quantifying the variation between the two methodologies. A surface was constructed based on the data points of each contour, and their difference was calculated similarly to the procedure described in the "Post-Processing" subsection. A contour presenting the obtained discrepancy is found in Fig. 8.3c. Considering the thickness gauge output as a benchmark, positive and negative values denote that the post-processed point cloud data overestimates or underestimates the remaining thickness, respectively, from the benchmark. The distribution frequency of the discrepancy

Table 8.1: Comparison of thickness estimations derived by post processed point clouds and measurements obtained with a D-meter at 6 locations with different levels of delamination. Points 1, 2 and 5 are in areas with extensive delamination.

Point ID	D-meter	LiDAR	Difference	Difference
	mm	*mm*	*mm*	%
1	7.6	9.1	1.5	+20
2	7.1	9.9	2.8	+39
3	10.4	10.6	0.2	+2
4	10.0	9.5	-0.5	-5
5	7.6	8.9	1.3	+17
6	6.4	6.8	0.4	+6

between the two surfaces is presented in Fig. 8.3d, with 56% of the corroded area captured with thickness variation less than $\pm$ 0.5 mm between the two methodologies. The mean difference is equal to 0.41 mm.

To better interpret the comparison output, thickness estimations are presented in Table 8.1 at six representative locations (Figs. 8.1 and 8.3). Point 3 which represents the intact web condition, has been captured with just 2% discrepancy, depicting an excellent agreement between the two methodologies. Point 6 is located in a region with section loss detected only at the right face of the web (Fig. 8.1c). The residual thickness estimation between the two methodologies varies only by 0.4 mm or 6%. Points 4 and 5 are located in the corroded area crossing vertically the left web face (Fig. 8.1c). At Point 4 where the beam surface is similar to Point 6, the thickness estimations by the two instruments vary only by 5%. On the other hand, it can be seen in Fig. 8.1b that points 1, 2 and 5 are located in areas where deposits and extensive delamination were covering the web faces, prior to removal of paint and scale, when the specimen was scanned. Their discrepancy with the measurements obtained by the gauge over the exposed steel rises up to 39%, highlighting the importance of a clean surface.

It is also worth noting, that the surface representation of the remaining web thickness based on the 283 thickness gauge data points provides reduced resolution compared to the LiDAR output which was meshed based on 6851 points. Consequently the LiDAR might provide a more accurate representation of the actual web condition between the grid lines, which are spaced every 2.5 cm. Considering both the provided accuracy of the proposed methodology and shortcomings in current field measurements when using conventional acquisition techniques, 3D laser scanning shows significant potential for future adoption in evaluation of corroded steel girders .

CHAPTER 9

EXPERIMENTAL TESTING

9.1 Specimen Description

In this Chapter a naturally corroded girder was scanned, before it was subjected to full scale experimental testing to measure its failure load and mode. Preliminary finite element analysis revealed that the previously described and scanned specimen from Bridge B would most likely result in a flexural failure due to the extensive flange section loss. Therefore a girder from a third bridge, referred to as Bridge C in this thesis, is utilized to experimentally explore the validity of the proposed methodology.

Bridge C was a three span steel bridge built in 1937 in the northern part of the state. The design of the bridge contained continuous 24CB120 (Table 9.1) un-stiffened rolled girders. The two piers divided the total length into three equal spans of 18.5 m long each. The bridge was deconstructed in 2019 due to the critical condition of the deck, which contained a number of large holes throughout its surface. According to the inspection reports, the deck underside had widespread leakages, which potentially led to widespread surface rust with areas of heavy corrosion damage in the girders.

Table 9.1: Nominal dimensions of the naturally corroded girders. The girder from Bridge B was used in the scanning proof-of-concept experiment (Chapter 8) and the girder from Bridge C was used for the mechanical testing.

Beam Type	Depth	Web Thick.	Flange Width	Flange Thick.	Fillet Radius
	d	t_{web}	b_f	t_f	R
	mm	mm	mm	mm	mm
21WF73 (Bridge B)	539.5	11.6	210.7	18.8	12.7
24CB120 (Bridge C)	617.5	14.1	307.1	23.6	17.8

For testing, a girder with localized areas of moderate to severe section loss above

Figure 9.1: The deterioration condition of the specimen obtained from Bridge B was characterized by section loss close to the support.

the support was selected . For transportation purposes as well as well due to the limitations of the testing facility, the girder was cut in the field, and a 7.6 m long segment containing the corroded end was transported for testing in the Brack Structural Laboratory at UMass.

While in service, the beam ends were connected transversely with 30 cm deep C beams diaphragms attached to riveted plates located at the upper half of the webs. After the bridge demolition, the steel diaphragms were removed but the plates at both web faces remained on the girder, Fig. 9.1. The girders were delivered with the sole plate welded to the bottom flange, which was later removed in the lab.

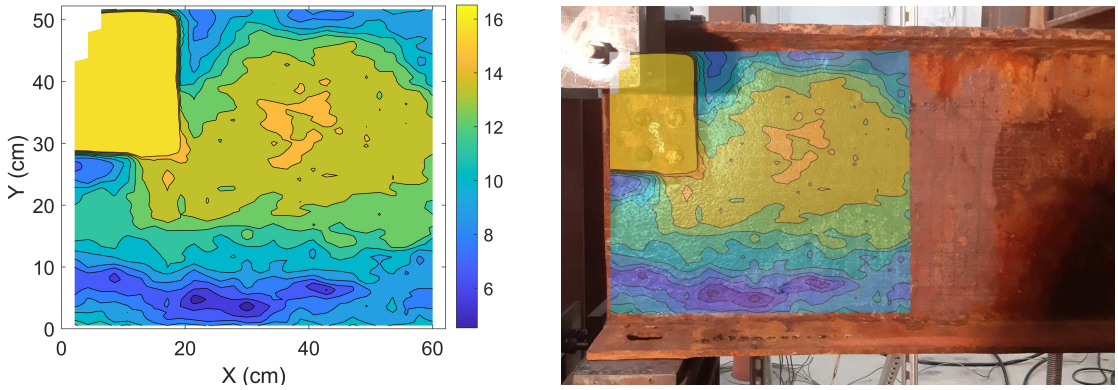

(a) (b)

Figure 9.2: a) Contour map from laser scanning illustrating the remaining web thickness along the web of the tested specimen. b) The same contour map projected on the actual geometry. The illustrated thickness values are in mm.

9.2 Section Loss Estimation

In contrast to the previously studied girder from Bridge B, no extensive delamination or deposits like mud are observed at the web faces of the girder from Bridge C. To estimate the remaining web thickness at the corroded web end,the same LiDAR equipment was utilized to scan both web faces. The acquired point clouds were processed following the procedure described in Chapter 8 of this thesis, and the derived thickness contours are presented in Fig. 9.2a. In Fig. 9.2b, these colored thickness contours are overlain on the actual specimen. Two areas with extensive section loss are observed. The first one is approximately 8.5 cm long by 3.0 cm high located below the remaining riveted plates. The second area of distinct section loss extends longitudinally directly above the bottom flange with dimensions 47.0 cm long up to 10.0 cm high. Reduced thickness is also observed towards the top flange and along the inner edge of the remaining plates.

9.3 Laboratory Testing

9.3.1 Testing Configuration

The testing configuration presented in Part I (Paragraph 3.1.4) was slightly modified to increase the applied load capacity. Loading was applied using two 980 KN hydraulic jacks, located under the bearing of the tested end of the specimen. The jacks applied an upward vertical force simulating the reaction at the tested end, FIg. 9.3. The force from each jack acted on a spreader beam that supported the bridge bearing on its top flange. A cross beam anchored to the laboratory strong floor by means of 4.6 cm threaded rods was retained from the previous configuration to hold the specimen down. Similar to the nomenclature of Part I, the beam end where the load is applied is referred to as the tested end while the other end is referred as the far end.

9.3.2 Instrumentation

In comparison with the instrumentation configuration described in Part I, an additional potentiometer was installed to measure vertical displacements developed close to load application area, Fig. 9.3. The exact location of the potentiometers measuring lateral deflections is included in the same figure.

9.4 Experimental Results

The beam failed by web buckling at an applied load of 478 KN, while the tested end's vertical displacement was 12.2 mm as shown in Fig. 9.4a. Visualizing the data recorded by the two potentiometer arrays, Fig. 9.4b depicts the lateral deformation profile of the web, for two different loads, 0.75 and 1.0 F_u, where F_u is the peak applied load. Given that the black line represents the initial web position assuming

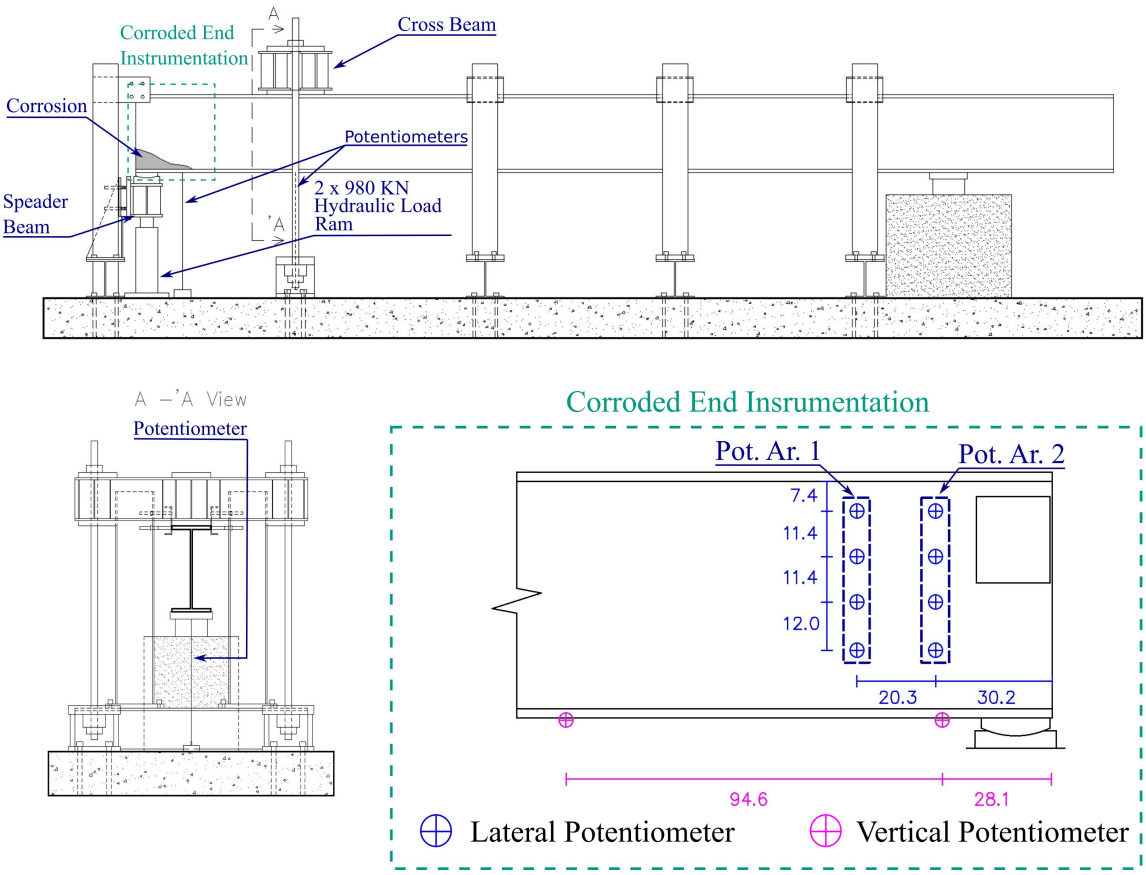

Figure 9.3: Experimental and instrumentation configuration. The illustrated values are in mm.

no deviation from straightness prior to load application, a sudden failure is captured with instantly developed lateral displacements. This behavior is in compliance with the sudden capacity drop observed in Fig. 9.4a.

Fig. 9.5 illustrates the developed displacements at peak load as they were captured from the two cameras recording the experimental procedure. A buckling wave was formed at the bottom part of the web with maximum magnitude at the outer web edge just above the bearing. The maximum lateral displacements profile is developed diagonally along the longitudinal axis of the beam, aligned to the region of the extensive section loss presented in Fig. 9.2b.

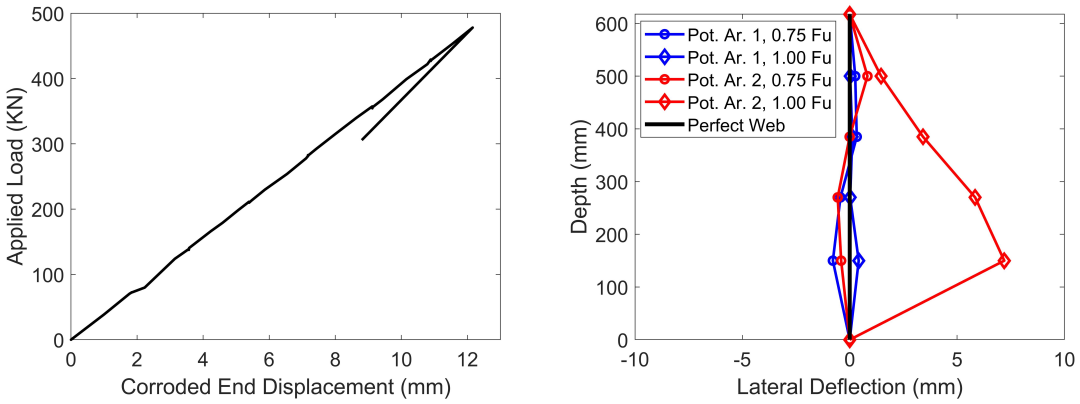

(a) (b)

Figure 9.4: a) Applied load versus vertical displacement. b) Lateral displacement profile as it was recorded from the potentiometer configuration in Fig. 9.3. The profiles are presented for two different loads, 0.75 and 1 Fu, where Fu is the peak measured load.

(a) (b)

Figure 9.5: a) Side and b) front view of the specimen at peak load. Large displacements were developed along the diagonal domain with extensive section loss, Fig. 9.2.

CHAPTER 10

FROM POINT CLOUDS TO CAPACITY ASSESSMENT

10.1 Computational Evaluation

10.1.1 Mechanical model

A methodology was designed to integrate point cloud data into a three dimensional geometrical model discretized with finite elements. In detail, ten levels of remaining material thickness between the minimum and the maximum recordings were derived (Fig. 9.2), and a Matlab script is employed to extract the coordinates of the points that constitute the contour lines, Fig. 8.3. Subsequently, a script in Python, was used to partition the web face of the simulated geometry by connecting the points on these lines. Having defined the deterioration boundaries, each one of the ten thickness values determined using 3D laser scanning was assigned to the corresponding areas

The material properties of steel were determined through tensile testing of coupons performed and presented in Paragraph 4.

10.1.2 Finite Element Model

Most of the computational model's aspects have been developed, validated and presented in Chapter5 of this thesis. Once again, the commercial finite element software ABAQUS [33] was utilized for simulation and analysis of the laboratory experiment. Shell elements were used to approximate a three-dimensional continuous body with a surface at the middle of the section. The actual thickness is taken into account, and assigned as a parameter to the corresponding elements.

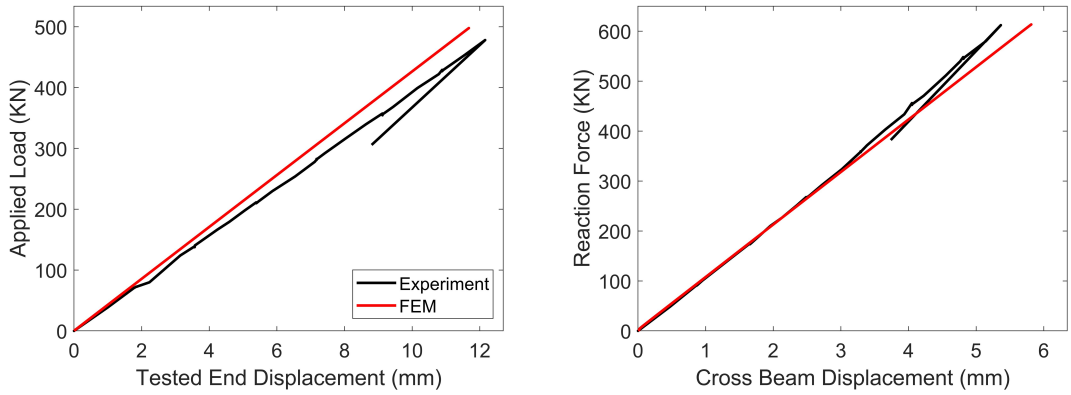

(a) (b)

Figure 10.1: Comparison between experimental and numerical results for a) applied load versus corroded end displacement and b) reaction force developed at the cross beam versus the recorded displacement at the same area.

A particular aspect of the finite element model that was studied is the effect of the beam-rod assembly flexibility at the cross beam location. Due to the reaction force magnitude developed at the anchor rods, the cross beam is essentially a non-fixed boundary support for the corroded girder. The experimentally captured stiffness of the area (104 KN/mm), presented in Fig. 10.1b was used to simulate this behavior. The constraints derived by the anchor rods - cross beam system were taken into account by introducing a spring, with its bottom end tied to the specimen's top flange and its top end clamped, Fig. 10.2. The out of plane displacement along the top flange was also restrained at the locations of the cantilevered braces. Finally, both bearings were simulated as hinges.

A two step quasi-static analysis was performed to simulate the dead as well as the incrementally applied load. Even-though this type of analysis is terminated once instability phenomena occur, the experimentally obtained data depict a global failure, thus expanding the analysis to the post-buckling regime would serve no purpose for the scope of this work. In order to capture instability phenomena, a geometric

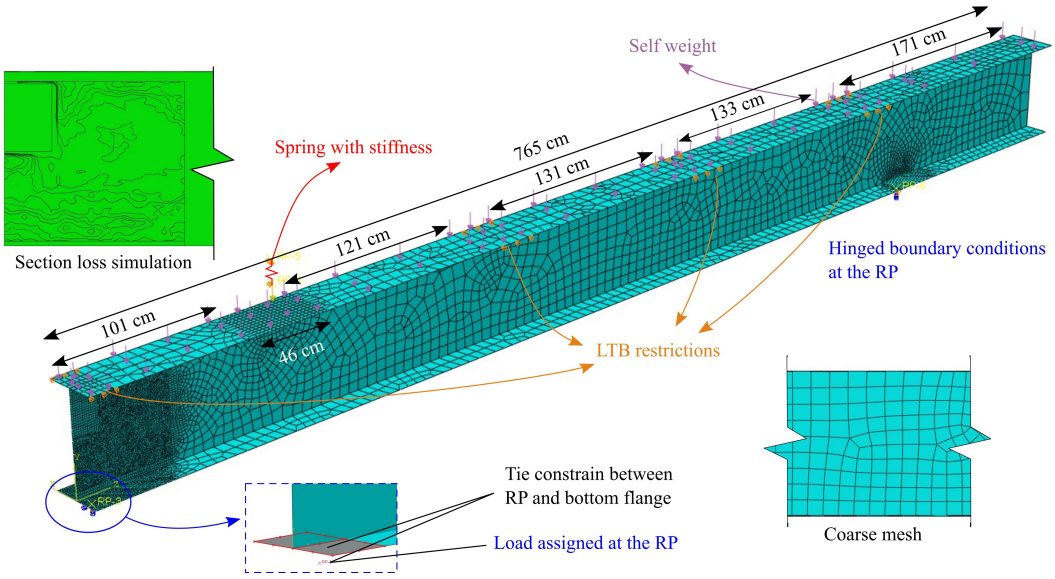

Figure 10.2: Developed finite element model for simulating the conducted experiment. The deterioration condition of the corroded end was integrated in the model by partitioning the web region and assigning the thickness levels illustrated in the contour map of Fig. 10.2.

non linear solution needs to be applied accounting geometric imperfections. This has been achieved by initially conducting a buckling eigenvalue analysis, and the first eigenmode was introduced as an initial geometric imperfection for the quasi-static analysis. Since no deviation from straightness was observed at the pre-testing condition of the web, the amplitude of the first eigenmode was scaled to the ten percent of the intact web thickness. Finally, the hydraulic jacks operation is idealized as a concentrated force applied upwards at the hinge located below the tested end.

10.1.3 Numerical Results

The applied load - vertical displacement relationship presented in Fig. 10.1 depicts a good agreement between the numerical and the experimental results. Regarding the peak load, the numerical model predicts failure at 497.7 KN of applied load, while the experimental value is 478.0 KN (overestimated by 4.1%). Fig. 10.3a presents

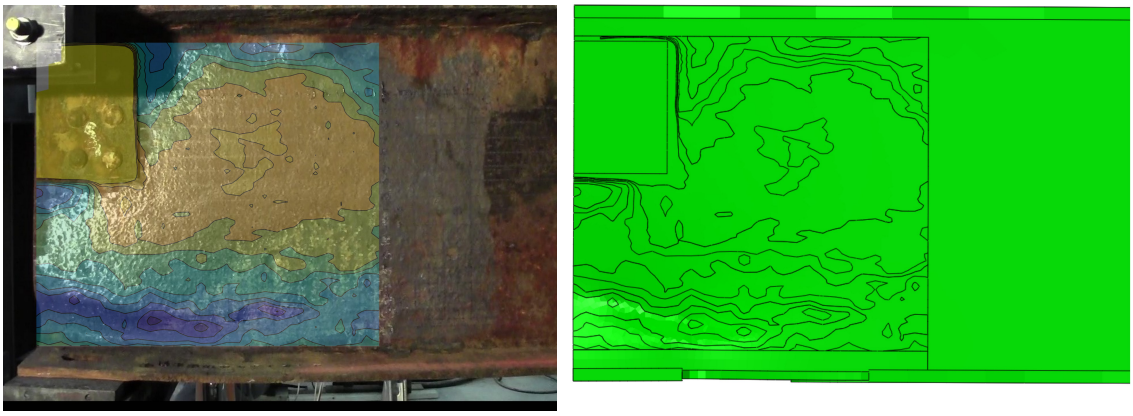

(a) (b)

Figure 10.3: a) Thickness contour map projected on the specimen after buckling failure. b) Displacements profile at peak load obtained from finite element simulation. In both cases large displacements are captured approximately in the same location.

the failure mode as it was captured by the video camera recording the experimental procedure. In Fig. 10.3 the section loss contours are projected on the failed specimen, while Fig. 10.3b presents the numerically obtained failure mode. Observation of the figure reveals that the failure mode is also satisfactorily captured. It is also worth noting that the section loss topology defined the developed displacements at failure. An important first finding from this analysis is that the 3D laser scanning procedure provides an accurate framework for the estimation of the capacity of corroded girders.

10.2 Analytical Evaluation

According to the Massachusetts DOT (MassDOT) Bridge Inspection Handbook [13] the live-load carrying capacity of bridges should be evaluated on a decade-basis unless concern occurs due to the critical condition of an asset. In that case, the inspectors can warrant a load rating request. In the state of Massachusetts, the remaining bearing capacity for aging steel bridges with deteriorated ends is estimated by provisions included in the MassDOT LRFD Bridge Manual [7]. The rating proce-

dures contained in MassDOT LRFD Bridge Manual are based on approximate closed form equations that only use a single value of remaining web thickness to grossly account for corrosion deterioration present at beam ends. To estimate the remaining web thickness, inspectors perform point measurements, in the area of interest, typically the corroded end region. Given that section loss is not uniform in the area of deterioration, the selected points where measurements are taken to be representative of the beam's condition is currently dependent on the inspectors judgement.

On the other hand, the closed form expressions developed by the author in Chapter 5 is dependent on the geometric characteristics of the girder. By taking into account the negligible web deviation from straightness which in general does not exceed 10% of the intact web thickness, as well as the N/d ratio, where N denotes the bearing length and the d the beam depth, the bearing capacity estimation is calculated by Eq. (20):

$$R_n = \left[0.6\sqrt{EF_y t_f}\; {t_{ave}}^{1.5} + 0.24^{\left(\frac{0.33d}{N}\right)} \left(\frac{4\ N}{d} - 0.2\right) \frac{\sqrt{EF_y t_f}}{t_f^{1.5}}\; {t_{ave}}^{3}\right] \left(\frac{CL}{N + 0.1\ d}\right)^{0.4} \tag{20}$$

where, E is the Young's Modulus, F_y is the steel yield stress, and CL is the length of the corroded region within the bottom part of the web bound by a rectangle with a base equal to $N + 0.1d$ and a 10 cm height, Fig. 10.4a. Finally, t_{ave} denotes the average remaining web thickness calculated according to Eq. 21.

$$t_{ave} = \frac{(N\ + 0.1d\ - H) * t_w}{N\ + 0.1d} \tag{21}$$

where H is the length of holes (if present) within the control rectangular area, and t_w the remaining web thickness.

According to the MassDOT LRFD Bridge Manual [7], Eq. 22 and Eq. 23 are used to estimate the remaining capacity of corroded beam ends based on governing failure mode. Considering the N/d ratio as well as the overhang length, the nominal resistance of the end is calculated on the basis of its yielding capacity as:

$$R_{n,yield} = \ f_y \ t_{ave} \ (2.5k + N) \tag{22}$$

and its crippling capacity is based on:

$$R_{n,crip} = \ 0.4t_{ave}^2 \ [1 \ + \left(\frac{4 \ (N - H)}{d} - 0.2\right) (\frac{t_{ave}}{t_f})^{1.5}] \sqrt{\frac{EF_y t_f}{t_{ave}}} \tag{23}$$

where k denotes the distance from outer face of the flange to web toe fillet. In this case t_{ave} is estimated within the bottom region of the web bound by a rectangle with a base equal to $N + 2.5k$ and a 10 cm height as:

$$t_{ave} = \ \frac{(N \ + 2.5k \ - H) * t_w}{N \ + 2.5k} \tag{24}$$

where, H is the holes length (if present) and t_w the remaining thickness within this rectangle, Fig. 10.4b.

Due to the absence of holes ($H = 0$), t_{ave} equals to t_w both in Eq. 21 and Eq. 24. For the particular specimen and by averaging the scanned cloud data on the areas of interest as defined by the two different specifications (10 cm by $N + 0.1d$ or 10 cm by $N + 2.5k$), the t_w for the proposed in Chapter 5 method is 8.5 mm and the t_w for the [7] method is 8.4 mm. Using these thickness values in Eqs. 20 and 23, would result to capacities of 558 kN for the proposed method and 412 kN for the [7] method showing a clear discrepancy between the capacity predictions and a measured capacity of 478kN during the test.

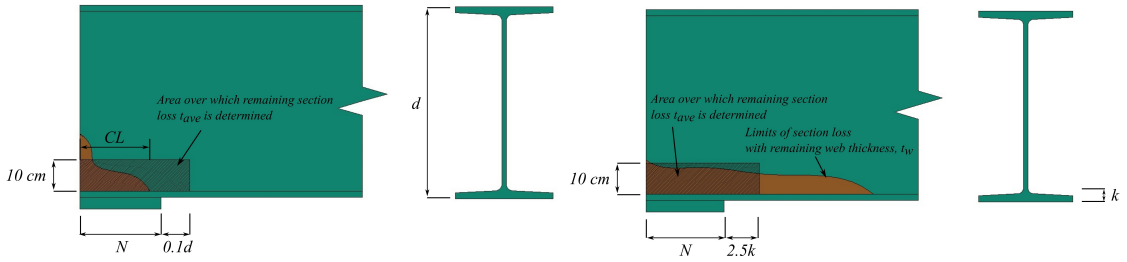

Figure 10.4: Parameters involved in the analytical evaluation process according to a) the proposed procedures in Chapter 5 and b) [7]. The corrosion condition of the beam is taken into account with the value of the remaining thickness t_w.

The source of this difference between the predicted values and the experimentally obtained capacity is attributed to the simplistic definition of the parameter t_w. One could expect that by scanning a corroded area and by averaging the measured values within this area would lead to a more accurate prediction of the capacity of the beam, but in reality the non-uniformity of the corrosion must be taken into account for a correct prediction. For the specimen under study, the average thickness of 8.5 mm for the previously proposed method is the source for a significant overestimation of the predicted capacity, because the nonuniformity of corrosion is dictating the capacity. The capacity is governed by buckling of a region within the 10 cm by N+0.1d area of interest in which the remaining thickness is less than the average of the area of interest. This would mean that in case a laser scanner is to be used to obtain measurements for predicting the capacity of corroded ends, a calculation of the remaining thickness in the 10cm by N+0.1d area by averaging the the measurements is a faulty calculation. In reality, this calculation needs to account for the non-uniformity of the corroded area and depending on the level of non-uniformity, perform a weighted average calculation. In this case, if only the lower 76% of the measurements is used (Fig. 10.5), the predicted capacity is 478 KN which corresponds to the experimental value.

On the other hand, the under-prediction of the current [7] method can be at-

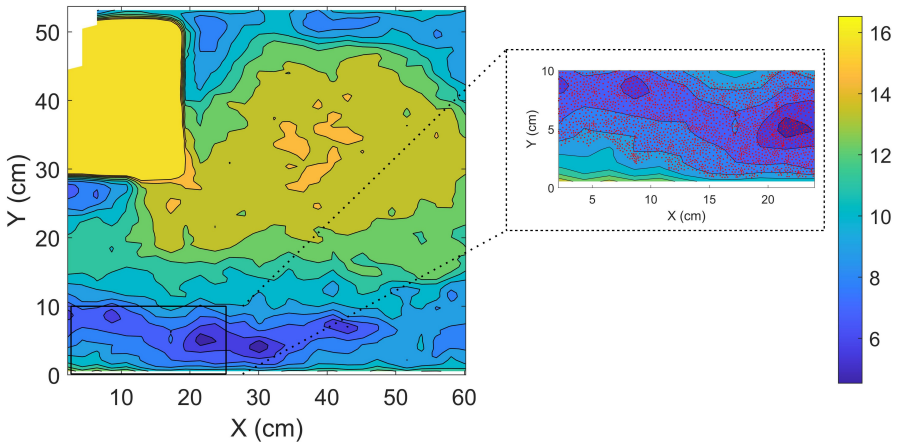

Figure 10.5: For the provisions proposed in Chapter 5, the failure load is analytically captured by calculating the average thickness of points (red dots) located manly along the diagonal domain which governed the failure mode. The remaining thickness values are in mm.

tributed to a significantly more conservative approach which also fails to capture the effect of non-uniform thicknesses on strength. Using this method for this particular case, the prediction was under the experimental value which is considered safe, but this cannot be attributed to the accuracy of the method, it is a rather over-conservative prediction overall.

The main finding from using laser scanning measurements with current or proposed analytical calculations is that there should be significant attention and more research on the calculation of the t_w. A weighted average method should be developed which would account for the non-uniformity of the corrosion. In terms of today's practice of obtaining limited values of the remaining material, the strategy of most inspectors to obtain values at the worst locations (lowest values of remaining materials) seems to be very important and should be continued to be followed.

10.3 Discussion

The second part of this thesis validated the reliability and the efficiency of 3D laser scanning as a potential technology for bridge inspections. LiDARs can address the shortcomings of conventional data acquisition techniques while at the same time abolish the sensitivity of ultrasonic thickness gauges along bumpy surfaces. Thickness estimations resulting 3D laser scanning post-processing were verified, and subsequently employed for capacity estimations. The proposed automated procedure can enable engineers to create finite element models which encapsulate the exact corrosion condition of damaged girders. This methodology provides a game-changing tool for dealing with the uncertainty that usually comes along with the analytical evaluation of beams presenting varying levels of corrosion-induced thickness losses, which currently results in conservative estimates of remaining capacity.

Nowadays, a typical bridge inspection report includes a text description of the corrosion induced damages. This description is usually supplemented with sketches and occasionally with photographs. Pictures may provide an excellent overview of the extent of damage, while sketches of varying levels of detail include the locations of usually a unique or two point measurements. On the other hand, the development of thickness contours based on 3D laser scanning techniques allows better capturing the remaining thickness field efficiently and accurately. Furthermore, the provided methodology not only captures the corrosion characteristics with remarkable accuracy but it also enables the quantification of section loss evolution in time if measurements from different periodic time intervals are compared.

It is worth noting, that the proposed methodology can be applied to any type of point cloud regardless of the instrument or method by which it was created. In particular, during the last years many DOTs in the country have explored or even

introduced the Unmanned Aerial Vehicles (UAVs) for visual inspection of bridges. UAVs implementation decreases the the number of inspectors, speeds up the process and increases the accessibility to bridge components, while at the same time prevents the inspectors exposure to danger. Given the recent advances in portable LiDARs, data could be also collected by aerial scanners mounted on drones, combining the advantages of both technologies.

Within these Chapters the need for cleaning the steel surfaces prior to scanning was highlighted. This task does not constitute necessarily an additional work task for inspectors, given that a hammer is nowadays used to expose the steel for thickness measurements obtained with the conventional methods anyway. It is worth noting though, that the use of another tool could be introduced considering that scanning requires the cleaning of a larger surface.

The last aspect regarding the applicability of the current work is the post processing time. Providing thickness input for the analytical provisions requires data manipulation that lasts approximately one to two hours, depending on the file size. In three to four additional hours, capacity estimation from a finite element model can be obtained, making use of the automated procedure and scripts. It is worth noting that the mentioned time can be further reduced through experience over time or more automated procedures.

CHAPTER 11

SUMMARY, CONCLUSIONS AND FUTURE WORK: PART II

11.1 Summary and Concluding Remarks

The goal of the present study was two-fold, first to explore the use of LiDAR technology for section loss quantification in deteriorated steel beams, and second to implement the post processed data both analytically and numerically for capacity evaluation of rolled I girders.

- A naturally corroded beam from a decommissioned bridge in MA was scanned and the obtained point clouds were processed to determine the remaining material distribution along part of the web. The efficiency of the proposed methodology was validated by measurements taken with an ultrasonic thickness gauge which is common practice in today's inspection techniques. The provided accuracy was found strongly related to the condition of the web surface. In detail, the mean error along the 1626 cm^2 surface was equal to 0.41 mm, while it was varying between 2% and 39% of the actual thickness for areas with coating and heavy delamination.

- Contours were used as a two-dimensional representation of the remaining thickness profile along the deteriorated area. This approach is easily processed from inspectors and engineers, it provides an overall description of the examined area, and it can be integrated in the inspection reports to upgrade the corrosion mapping.

- Post processed point cloud data can be used for the assessment of the remaining capacity of deteriorated beam ends. A numerical study included the creation of computational meshes which integrate the exact condition of corroded girders. This approach was validated with full scale experimental testing of a naturally corroded girder. Comparison of numerically and experimentally obtained results provided credibility to the proposed automated methodology, since the failure load of the simulated specimen was captured with an error of 4.1%.

- The analytical provisions consider the corrosion condition of a steel girder by integrating a unique thickness value representative of the remaining material above the support. Given the non uniformity of corrosion phenomenon, the LiDAR implementation enabled to investigate the physical meaning of the thickness which analytically captures the failure load. A key finding, is that inspectors should identify, within the bottom 10 cm of the web, the subdomain which based on engineering judgment is in critical condition, and average thickness measurements along this area. Furthermore, identification of these subdomains can be facilitated by LiDAR implementation and weighted average techniques should be developed. In any case, a generalised average along the whole web bottom should be avoided.

11.2 Outlook and Future Work

Despite the promising results emerging from the proposed thesis, the actual question lies in its applicability. Regarding the portability of the equipment, the employed scanner of this paper is a terrestrial LiDAR with weight that exceeds 9 kg. Point clouds need to be captured on both sides of the web limiting the use of this instrument to relatively accessible field conditions. Consequently, scanning in the field

could be performed exclusively from a man bucket. The snooper truck implementation wouldn't reduce the exposure of the user - inspector to potential danger neither would avoid the traffic delays. In addition, methodology modification might be required to address the noise due to man bucket's movement during scanning. However, even under these conditions it could provide more objective and accurate thickness estimations in a much shorter time, when compared to distinct point measurements. In addition, the rapid improvement of LiDARs is expected to make this technology much more accessible and implementable in the near future.

A semi-automated procedure for the creation of contour maps depicting the remaining material along corroded steel members was developed and validated. However, this procedure demands data manipulation and exchange between a point clouds post-processing software and scrips in two programming languages. For the examined beams, approximately two hours post-processing time was required for the integration of the final data in a three dimensional finite element model. To be widely adopted, however, the proposed methodology should require less labor, by fully automating the processing framework. Artificial intelligence techniques can be employed for section loss detection and quantification.

As it was previously mentioned 3D laser scanning implementation allowed to investigate the physical meaning of the thickness that analytically captures the failure load. However, beam end corrosion is a multi-parametric problem and more data points are required to extract definitive conclusions. Scanning and testing addition girders with corroded ends will shed light to the thickness that should be considered for analytical capacity evaluation.

PART III:

CAPACITY EVALUATION OF PLATE GIRDERS WITH CORRODED ENDS

CHAPTER 12

LITERATURE REVIEW AND OBJECTIVES

12.1 Opening Remarks and Literature Review

Aging bridges are prone to malfunctioning expansion joint deck joints, mainly because these components are periodically subjected to impact tools by passing vehicles, as well as to environmental factors. These conditions induce damage allowing leaking water to penetrate into the bridge superstructure, triggering corrosion of the steel girders ends which are typically located below the bridge expansion joints.

Depending on the severity of thickness loss, the load bearing capacity of steel girders might be significantly reduced. In order to ensure public safety but at the same time avoiding posting bridges, efficient tools for capacity evaluation are required. In Part II of the current study, the author developed a methodology employing 3D laser scanning for quantification of section loss along corroded girders. The acquired point cloud data were processed to develop contour maps that could be integrated in inspection reports providing a sophisticated overview of the girders section loss. Scripts were also written to combine the derived thickness maps with three dimensional finite element models to computationally evaluate the remaining girder capacity. Furthermore, post processed point cloud data can be used as input in concise closed form equations developed in Part I, of this study, for capacity assessment of un-stiffened rolled girders. However, except of rolled girders, plate girders with stiffeners constitute a significant fraction of the steel bridge population in the Northern States and in the state of Massachusetts.

Researchers have studied the beam end corrosion problem for plate girders both experimentally and numerically. Even though the work of Sugimoto et al. [20] focuses

on railway bridges, it is worth noting that experimental testing was conducted, of both on decommissioned riveted plate girders as well as on girders with artificial section loss. Eventually, they proposed analytical expressions describing a linear relationship between the shear strength and thickness loss ratios. Kim et al. [63] experimentally explored the shear behavior of corroded web panels, concluding that deterioration results in larger failure regions. From the same research group, Ahn et al. [64] conducted experiments representing web panels with pitting and through-thickness corrosion damage, reporting their significant impact on the shear buckling behavior when they extend to a critical corrosion damage level in the diagonal tension field. In a previous work [65] focusing on both computational and experimental research, a reduction factor to estimate the residual shear strength of plate girders with web damage was proposed. A study by Khurram et al. [66] explored the effect of local corrosion damage along the bearing stiffeners as well as the end panel both experimentally and computationally, indicating that the minimum thickness within any damage height may be used to simulate the corrosion damage in a computational analysis.

In an exclusively computational work Ahn et al. [11] concluded that the damage shape (triangular or rectangular) affects the plate girder's capacity only when it intersects with the tension field of the web panel. Usukura et al. [67] employed the finite element method to a sensitivity analysis to explore the capacity and the collapse mechanism of plate girders with corroded ends. Liu et al. [68] analytically examined the effect of four different corrosion shapes, pointing out the harmful impact of the corrosion induced damage height compared to corrosion length. Finally, Yamaguchi and Akagi [69] highlighted the effect of the web corrosion pattern on the shear capacity of edge panels.

It is worth noting that the majority of the previously mentioned research studies

focused on the panel shear failure by accounting for strong bearing stiffeners without corrosion. Data acquired by the author from inspection reports as well as inspectors observations in Massachusetts, however, indicate that stiffeners most often undergo severe section loss due to corrosion. Another point of concern emerges from the fact that except for the work of [20] on railway bridges, the available studies experimentally studied the corrosion effect by assuming a uniform reduction of thickness in the girder web and, sometimes, the stiffeners. However, given the corrosion topological non-uniformity in the field, this approach might not be able to capture failure mechanisms related to the variability of the corrosion phenomenon.

12.2 Scope and Outline

To address the previously mentioned limitations, this Part applies the knowledge built in Parts I and II of the current thesis to develop analytical tools for the load bearing capacity of plate girders with corroded ends. Following a similar methodology, in Chapter 13 a naturally corroded specimen is tested to study its load and mode of failure. In Chapter 14 the obtained experimental data are combined with data from the literature, to computationally validate the composite action of beams with shear studs along the top flange. Subsequently, the numerical study is extended to a series of simulations conducted to investigate the performance of varying girder types under numerous geometry and corrosion scenarios. In Chapter 5, empirical relationships are built to describe the relationship between corrosion characteristics and capacities of a sample consisting of more than 1000 scenarios. Finally, the newly developed procedures are combined with 3D laser scanning to analytically evaluate the tested girder.

CHAPTER 13

EXPERIMENTAL TESTING

13.1 Specimen Description

In this Chapter the failure mechanism of a corroded stiffened girder is experimentally examined. For this purpose, a naturally deteriorated girder was used and stiffeners were welded prior to testing. The specimen, a 24CB120 girder (Table 13.1), was obtained from a demolished bridge, previously described in Chapter 9 and referred to as Bridge C. It is worth noting that the bridge was rehabilitated due to the critical condition of the deck, which contained a number of large holes throughout its surface. According to the inspection reports, the deck underside had widespread leakages, which potentially led to widespread surface rust with areas of heavy corrosion damage in the girders.

Table 13.1: Nominal dimensions of the naturally corroded girder used for the mechanical testing.

Beam Type	Depth	Web Thick.	Flange Width	Flange Thick.	Fillet Radius
	d	t_{web}	b_f	t_f	R
	mm	mm	mm	mm	mm
24CB120	617.5	14.1	307.1	23.6	17.8

The decommissioned girders had exhibited corrosion damage which was characterized by localized areas of moderate to severe section loss above the supports. The test specimen was obtained by cutting beams in the field to fit within the testing facility, resulting in a 7.65 m long segment containing the corroded end. While in service, a steel diaphragm consisting of 30 cm deep C beams was attached to riveted plates located at the upper half of the specimen's web, Fig. 13.1a. For testing purposes,

both the steel diaphragms and the plates were removed prior to welding full-depth stiffeners to the beam on the test end, Fig. 13.1b and c.

A detailed study of inspection reports indicated that a typical failure of girders with corroded ends includes out of plane displacements developed at the web and the stiffeners located above the support. To prevent flexural strength from governing the failure mode during the test, two 12.8 mm thick cover plates were welded to the top and bottom flanges along the first 2.3 m of the beam, Fig. 13.2. Moreover, to resemble a deteriorated stiffened beam end, stiffeners with varying dimensions were welded along the specimen, introducing two web panels above the corroded support. To account for the reduced thickness of a corroded end, the bearing stiffeners thickness was set equal to 6.4 mm, while the thickness of the adjacent pair was increased to 12.8 in. corresponding to the dimensions of an intact stiffener, Fig. 13.1c.

13.2 Section Loss Estimation

To quantify the remaining thickness on the deteriorated beam end, the beam was scanned making use of a Riegl VZ-2000 laser scanner, [61]. Scans were performed from both sides of the specimen and the acquired point clouds were referenced to a unique coordinate system making use of reflective targets placed in the laboratory. Following a methodology previously developed by the author in Part II, contour maps capturing the remaining material along the web were created and presented in Fig. 13.2c. An area with extensive section loss extended diagonally from the end to the bottom flange, while initial web deviation is noticed at the outer part of the web, with maximum magnitude of 1.1 cm, Fig 13.1b.

(a)

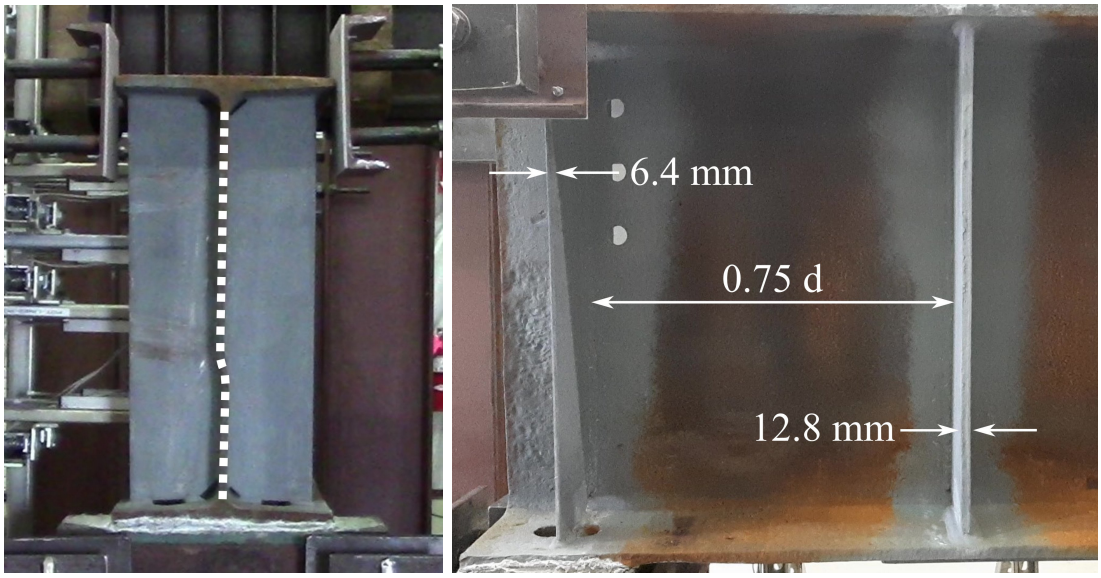

(b) (c)

Figure 13.1: a) The tested specimen as it was retrieved from the decommissioned bridge. b) Front and c) side view of the corroded end after stiffener welding. The imperfect web profile is highlighted with a white dashed line.

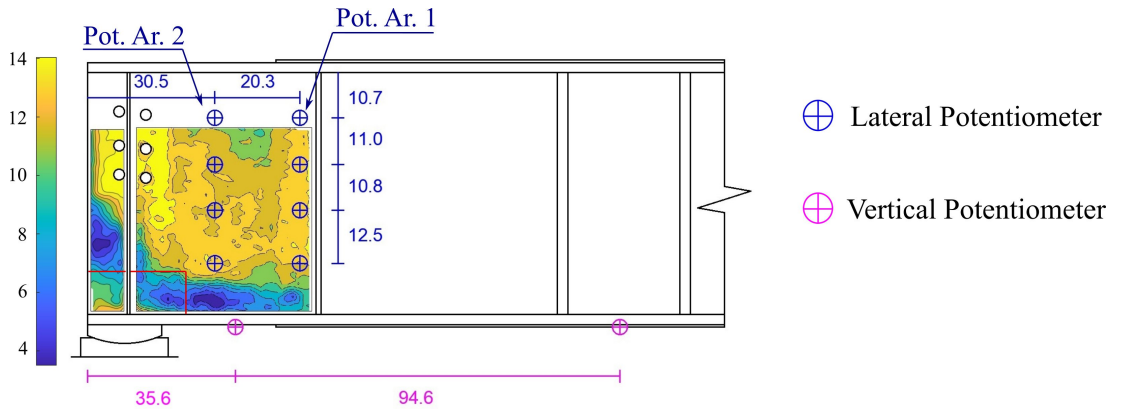

Figure 13.2: Contour maps from laser scanning illustrate the remaining web thickness along the corroded end. The illustrated length and thickness values are in cm and mm, respectively. The red lines at the web bottom denote the borders of the area of interest defined in Chapter (ADD) of the current study.

13.3 Test Conditions

Similar to the experimental configuration presented in Chapter 9 and in Fig. 9.3, a force controlled loading protocol was followed using two 980 kN hydraulic jacks. The load was applied vertically upward at the test end support through a load transfer beam, on the top of which a 17.8 cm long bridge bearing was welded. The bearing consists of two curved plates accommodating rotational and translational displacements, while the far end was resting on a 30.5 cm long rectangular steel plate. To hold the test beam down during loading, a heavy cross beam was placed and anchored to the laboratory strong floor at a section located 1.2 m from the beam support. To prevent failure modes related to later-torsional buckling, the top flange was laterally supported by 4 pairs of cantilevered braces along the length of the girder. Both the applied load as well as the reaction forces were measured using 3 load cells. Eight potentiometers were also used to capture lateral deformations within the first web panel; their arrangement is shown in Fig. 13.2. All the instrumentation data was recorded every 3 sec. using a data acquisition system.

13.4 Experiment Results

The beam failed by web buckling at an applied load of 996 KN, corresponding to the tested end's vertical displacement of 22.6 mm as shown in Fig. 13.4a. Visualizing the data recorded by the two potentiometer arrays, Fig. 13.4b depicts the lateral deformation profile of the web, for two different loads, 0.90 and 1.0 F_u, where F_u is the peak applied load. A vertical black line represents the initial web position assuming no deviation from straightness prior to load application, It can be observed that large lateral displacement of the web occurred during the last steps approaching the failure load. The same figure also reveals that the deformations were concentrated only in parts of the web panel located close to the bearing stiffeners (Pot. Ar. 2 in Fig. 13.2c). This behavior is in compliance with Fig. 13.3 which illustrates the displacements developed at peak load as they were captured from the two cameras recording the experimental procedure. Visual observation indicates that lateral deformations mainly occurred at the outer part of the web governed by the initial web deviation from straightness at this area.

Therefore, an assertion that the failure mode is solely governed by the web characteristics (deviation from straightness and section loss profile) would be inaccurate given that the welded bearing stiffeners were thinner than is common for this type of bridge to artificially simulate loss of section in the stiffeners as well. The effect of smaller stiffener thickness likely also contributed to the observed failure mode in the test.

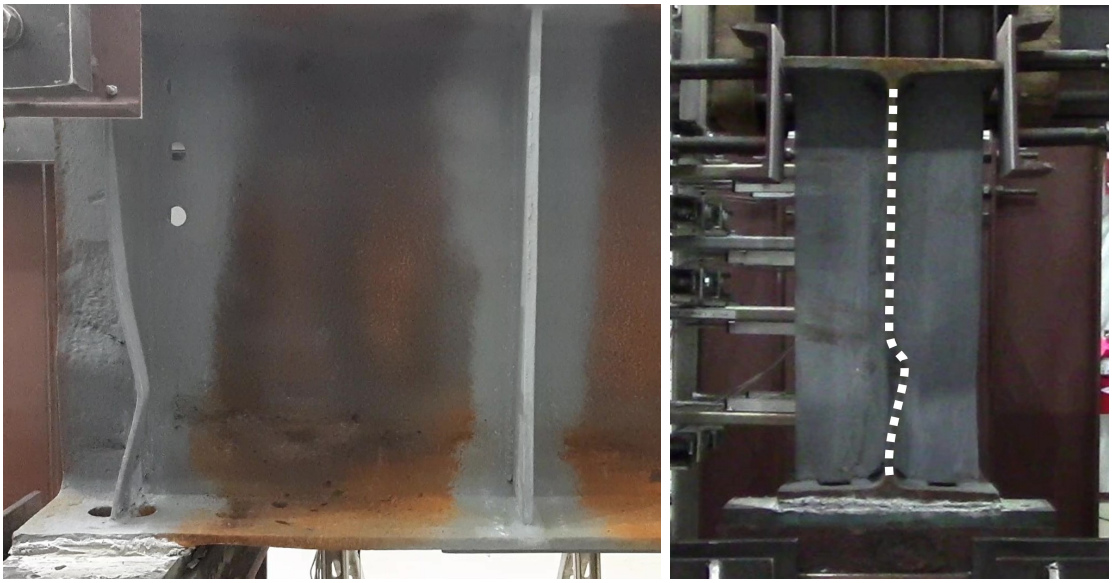

(a) (b)

Figure 13.3: Experimental a) side and b) front view of the specimen at peak load.

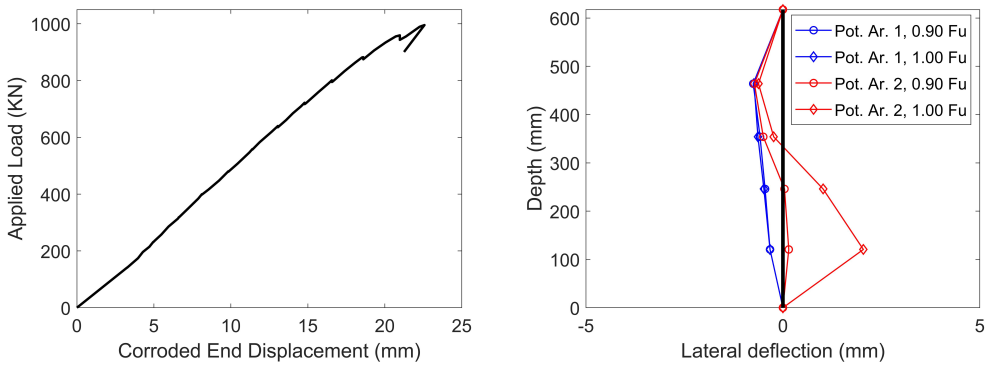

(a) (b)

Figure 13.4: Results from the conducted experiment: a) applied load versus corroded end displacement. b) Lateral displacement profiles as they were recorded from the potentiometer configuration in Fig. 13.2. The profiles are presented for loads equal to 0.9 and 1.0 F_u, where F_u is the peak measured load.

CHAPTER 14

COMPUTATIONAL EVALUATION OF CORRODED PLATE GIRDERS

14.1 FEM Validation

14.1.1 Mechanical Model

To validate the efficiency of the derived finite element model to capture the failure mode and load of stiffened girders with corrosion induced end damage, the experiment presented in Chapter 13 was simulated. The nominal dimensions of the specimen are given in Table 13.1 and the remaining thickness profile in Fig. 13.2. The material properties for the specimen were derived through tensile testing performed in Chapter 3, and presented in Fig. 4.3. For the welded members, a bi-linear constitutive law with hardening based on experimental data provided by the supplier is assumed, with 330 MPa and 400 MPa, yield and ultimate stress, respectively.

14.1.2 Finite Element Model

The computational model initially developed in Chapter 4 to capture the failure mechanism of rolled girders, was modified in Chapter 10 to integrate accurate representations of the remaining thickness derived by post-processed point cloud data. In this Chapter, aspects from both models are combined to capture the failure load and mode of plate girders with corroded ends. Once again, the commercial finite element software ABAQUS [33] is employed. An adaptive mesh with element size in the range of 1.3 cm to 6.5 cm was used. Both bearings were simulated as hinges, by applying the tie constraint between the simulated bearing plates and reference points

introduced to the centers of rotation of each bearing. The interaction between the bottom flange and the bearing plates was idealized by introducing contact.

The test setup configuration included a stiff cross beam that held the specimen down by anchoring it to the strong floor using two large diameter threaded rods. To capture the flexibility of this restraint system, the experimentally measured displacements of the cross beam were used to determine the stiffness of the hold down system (135 kN/mm). Fig. 14.1 illustrates how the flexibility of the hold down system was introduced into the finite element model. The stiffness determined for the hold down system was taken into account by introducing a spring, with its bottom end tied to the top flange of the model. The deterioration condition of the tested end was taken into account by incorporating the derived thickness maps (Fig. 13.2) in the model with ten different levels of remaining thickness based on a procedure described in Part II.

To capture the experimentally obtained instability related failure mode, the eigenmode which satisfactorily captures the pre-test imperfect beam shape was introduced as geometric imperfection for the quasi-static analysis. Finally, the load is applied in two steps, accounting both for the dead as well as the applied load, respectively. The dead load is applied as uniform pressure along the top flange, and the jacks load as a concentrated force applied to the reference point below the tested end, Fig. 14.1.

14.1.3 Numerical Results

Figs. 14.2a and b, depict a good agreement between the experimental and finite element results, capturing both the stiffness as well as forces at the test end and hold down beam positions between the tested end and the cross beam area. The peak load determined numerically was 1025 kN, which is only 3% higher than the measured force in the laboratory experiment. In addition, visual observation of the

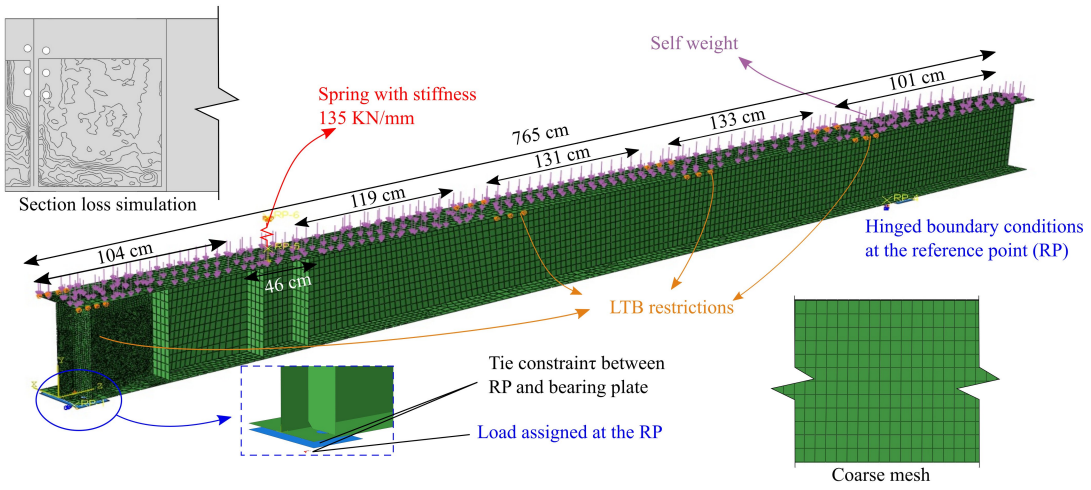

Figure 14.1: Developed finite element model for simulating the experiment.

failure modes (Fig. 14.3) indicates that in both cases large out of plane displacements were mainly developed at the domain between the bearing stiffener and the beam's end, governed by the initial web imperfection highlighted in Fig. 13.1b. It is also worth noting that same area exhibits significant section loss (Fig. 13.2).

14.2 Composite Action

The ability of the developed finite element model to capture the failure mode and load of stiffened girders with corroded ends provided confidence in its accuracy. However, to better capture in-service behavior of beams with corroded end, the effect of a composite concrete deck was included in the finite element model. Construction drawings of the time of construction describe most bridges as being built compositely with the deck by including shear studs welded to the top flange and embedded in the concrete deck.

The composite behavior was incorporated in the finite element model by introducing shear studs and a concrete deck simulated with a multi point constraint (MPC) and shell elements with 7 Gauss quadrature integration points, respectively. Similar

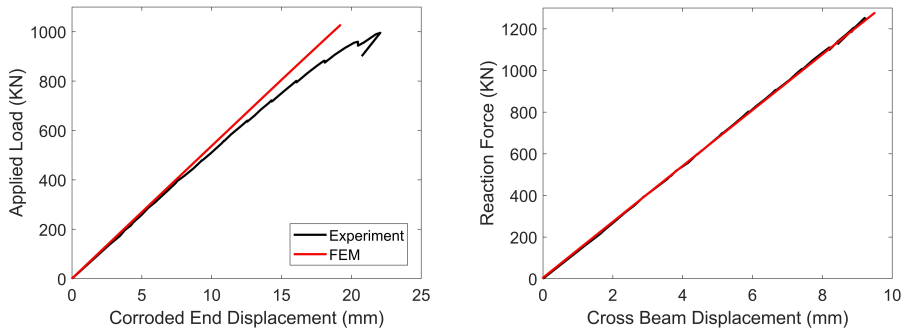

(a) (b)

Figure 14.2: Comparison between experimental and numerical results for a) applied load versus corroded end displacement and b) reaction force versus displacements developed at the cross beam area, for the conducted experiment.

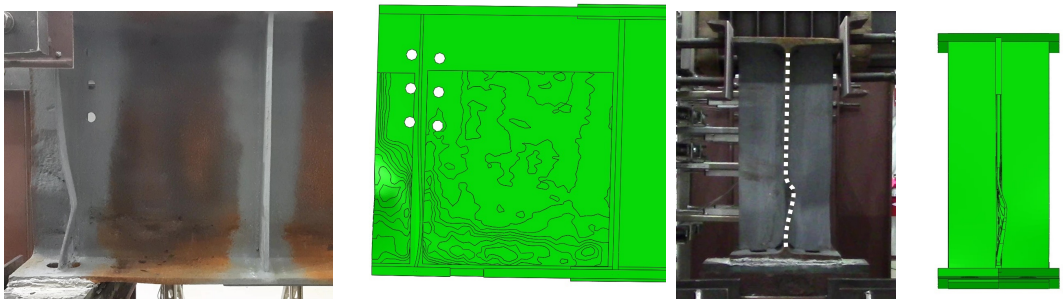

(a) (b) (c) (d)

Figure 14.3: a) Experimental and b) numerical side view of the specimen at peak load. c) Experimental and d) numerical front view of the specimen at the same load. The developed model is able to capture the failure mode of the tested girder.

modeling assumptions have been validated by Barth and Wu [70], who analyzed 3-point bending of two laboratory tests employing simply supported composite girders conducted by Mans [8]. Both studies were carried out until the crushing of the concrete slabs. Deck was modeled assuming linear-elastic material properties because the loading conditions of the current study are intended to generate high shear close to the corroded support. Consequently, concrete failure related to the compression of the slab due to high moment is not expected to occur.

Under these assumptions, Fig. 14.5d depicts a comparison between numerical

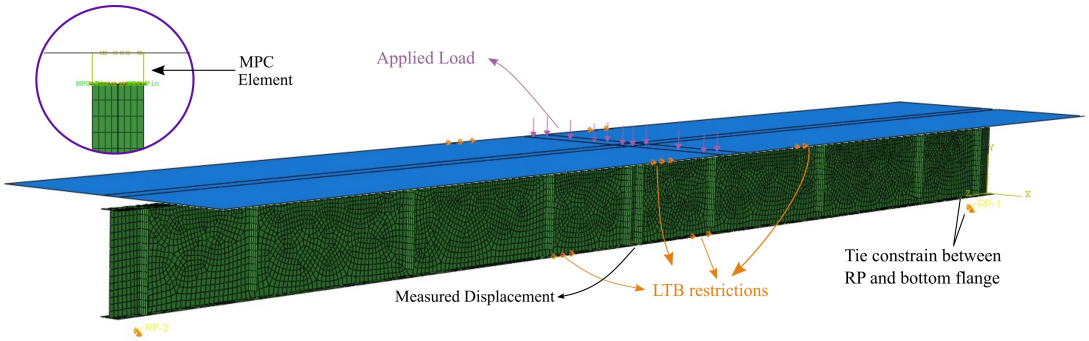

Figure 14.4: Finite element model developed to validate the composite action simulation by simulating the experiment conducted by [8].

end experimental results for the specimen "POS2" (Fig. 14.4) tested by [8]. The presented finite element model is able to capture the stiffness of the girder even after the bottom flange yielding, for vertical displacement equal to 75 mm. The analysis was not continued beyond the applied load of 1380 kN, where initiation of the concrete slab failure governed the behavior of the specimen during the laboratory experiment.

By combining aspects from the two modeling approaches, one validated using a laboratory experiment of a beam with corroded end (this study), and a second one with a validated modeling approach of a composite beam test reported by Mans [8], both the composite action as well as the failure of girders with deteriorated stiffened ends cab be captured.

14.3 Parametric Analysis

Initially a space for a sensitivity analysis is designed, and subsequently the validated composite beam-level model was employed in a series of simulations to establish a fundamental understanding of the impact of numerous deterioration parameters on stiffened girders.

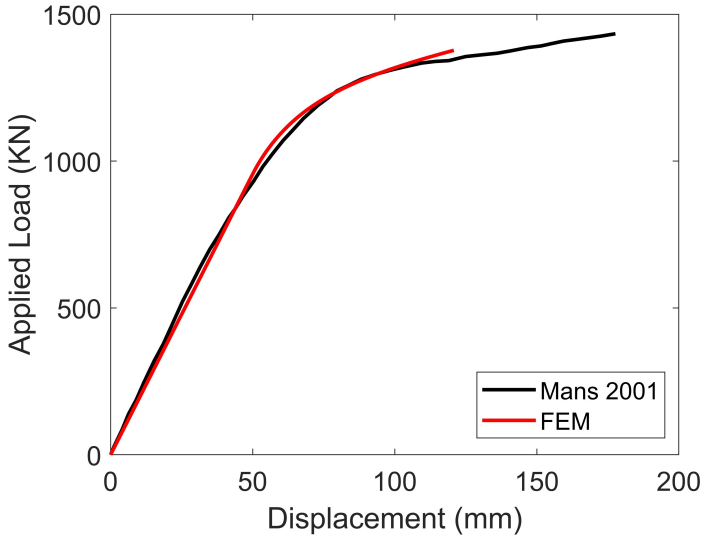

Figure 14.5: Comparison between experimental and numerical results for the experiment conducted by [8].

14.3.1 Analysis Set-up

14.3.1.1 Corrosion Scenarios

Both the topology and the intensity of the corrosion phenomenon consist the most critical aspects of the upcoming computational analyses. To accurately identify and quantify the parameters describing the corrosion morphology, numerous inspection reports provided by MassDOT, were reviewed. Based on a methodology that was initially introduced in [16], the problem was categorized through the development of general corrosion patterns describing the vast majority of the deterioration topologies observed at the available inspection reports, Fig. 14.6. Each pattern was combined with parameters defining the extent of the damage domain, as well as the remaining web thickness under the assumption of uniform section loss. After relating the deterioration condition of 210 independent corroded beam ends included in 30 inspection reports with one of the general patterns, the range of variation of the recorded parameters quantifying the bounds for the most common corrosion topologies, was defined.

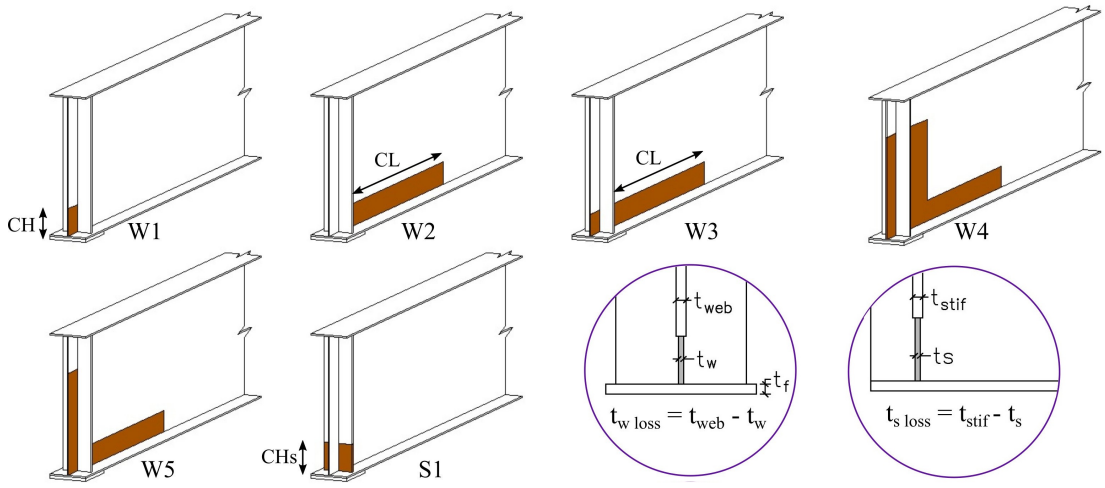

Figure 14.6: General patterns describing the most common corrosion topologies for stiffened beams. The range of variation for the parameters describing patterns 1 to 4 are given in Table 14.1.

In this thesis, the web corrosion patterns W1, W2 and W3 in combination with the stiffener corrosion pattern S1 in Fig. 14.6 are employed to study the deterioration effect to the bearing capacity of stiffened girders. For each one of the chosen patterns, the associated metrics describing the damage extension are presented in Table 14.1.

The corrosion scenarios were projected on a girder spanning 16 m and labelled as Geometry I in Fig. 14.7.The first two stiffener spaces at the ends of the beams are placed at intervals equal to half the web depth, while for the remaining length of the girder the spacing of stiffeners is doubled. This stiffener spacing is in compliance with the recommendations by [71] which was the bridge design standard used when the majority of bridges with stiffened ends were built in the state. Along the top flange, 32 pairs of shear studs are uniformly spaced, bonded to a 2.4 m wide concrete slab.

14.3.1.2 Boundary and Loading Conditions

To simulate in service conditions, out of plane plane displacement restrictions are applied along the slab sides. Additionally to the translational degree of freedom,

Table 14.1: Analytical description of the examined corrosion patterns, nomenclature is defined in Fig. 14.6.

No.	Pat.	CH (d)	CL (d)	$\frac{t_{wloss}}{t_{web}}$	CHs (d)	$\frac{t_{sloss}}{t_{stif}}$
1	W1	0-20%	-	0-10%, 50-90%	-	-
2	W1	100%	-	30-80%	-	-
3	W2	0-20%	0-130%	20-80%	-	-
4	W3	0-16%	0-85%	40-80%	-	-
5	S1	-	-	-	0-25%, 100%	10-90%

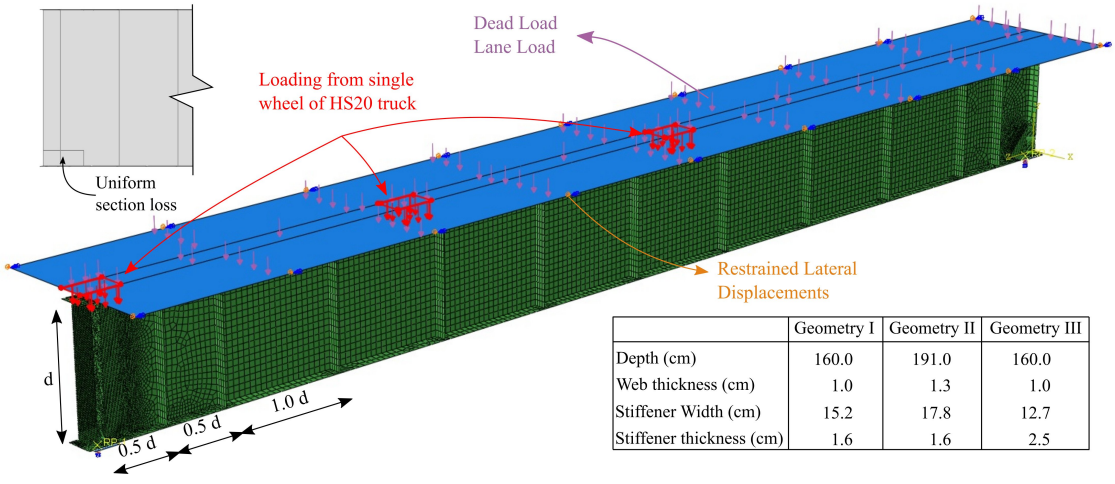

	Geometry I	Geometry II	Geometry III
Depth (cm)	160.0	191.0	160.0
Web thickness (cm)	1.0	1.3	1.0
Stiffener Width (cm)	15.2	17.8	12.7
Stiffener thickness (cm)	1.6	1.6	2.5

Figure 14.7: Finite element model developed for the parametric analysis.

torsional rotations along the longitudinal axis of the beam are also restricted. At the support areas, the same provisions [71] dictate that beams spanning more than 15 m shall be provided with a type of bearing employing a hinge, curved bearing plates or pin arrangement for deflection purposes. Consequently, the supports were modeled under the assumptions presented in earlier in this Chapter.

A dead load equal to 8 KPa is applied on the slab to account for the selfweight of the beam as well as the contribution of the deck. Live load is subsequently applied based on the HL-93 load check. The HL-93 consists of a three-axle truck (HS20) placed for maximum shear developed at the corroded end, plus the design lane load that is equal to 9.3 kN/m. The lane load is applied as a uniform pressure on the slab, similarly to the dead load. The truck load tire contact areas are located on the slab, covering the full flange width and 51 cm longitudinally. Live load is sequentially increased until the loading carrying capacity of the deteriorated end is reached. To ensure a uniform load transfer between the deck and the top flange, a contact interaction is introduced between the two surfaces. Finally, a 2.5 cm thick cover plate is also considered for the bottom flange. A representation of the model as well the characteristics of the three examined geometries are given in Fig. 14.7.

14.3.2 Results

14.3.2.1 Effect of Geometric Imperfection

Both the experimental and the computational aspects of Part I of this thesis have revealed the deleterious effect of web imperfections on the capacity of unstiffened girders with corroded ends. Specifically, it was highlighted that the corrosion-induced web deviation from straightness is a critical parameter that can significantly reduce the load bearing capacity of deteriorated beams. Building on this experience, and based on inspection reports as well as on inspectors observations it was concluded that

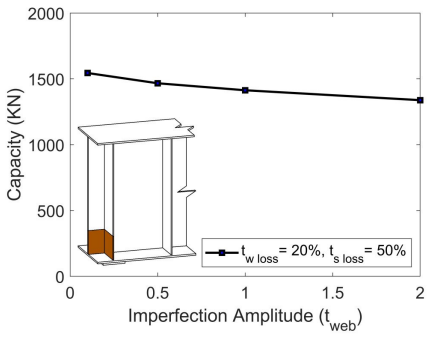

Figure 14.8: Effect of imperfection amplitude on the residual bearing capacity, for the examined scenarios.

similar imperfections are also present on stiffened beams. Consequently, analyses were carried out to evaluate the effect of geometric non linearities to the residual strength of stiffened ends. The pre-loading web deviation was incorporated in the simulated geometries by introducing and scaling imperfections based on the eigenmode shapes. Each scenario was initially solved using the eigenvalue buckling analysis algorithm and the eigenmode that involved at the damaged end was introduced as geometric imperfection for the quasi-static analysis.

A general result that emerged the finite element study was that, in contrast with un-stiffened beams, the results were in general insensitive to geometric imperfections with magnitude in the range of $0.1t_{web}$ to $0.2t_{web}$, where t_{web} is the intact web thickness. Fig. 14.8 computed maximum loads for increasing imperfection amplitude. It is worth noting that among 170 examined scenarios the most significant capacity reduction did not exceed 23%. Based on these findings, the most aggressive imperfection amplitude equal to 1.0 t_{web} is considered for the rest of the parametric study.

14.3.2.2 Effect of Stiffener Corrosion Topology

A series of analysis were run to study the effect of the stiffener corrosion characteristics to the girder's strength. In Fig. 14.9 the stiffener section loss is related to the residual

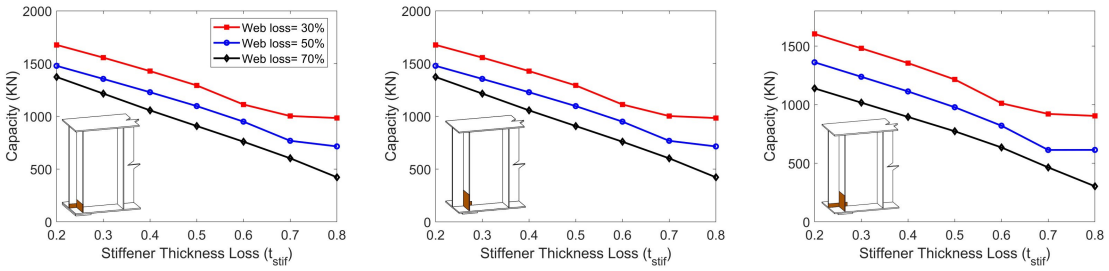

(a) (b) (c)

Figure 14.9: Effect of stiffener section loss related to a) W1, b) W2 and c) W3 patterns. The relationship between the bearing capacity and the stiffeners thickness could be idealized as linear.

bearing capacity for three different levels of web section loss (30%, 50% and 70% of t_{web}) for scenarios according to the three examined corrosion patterns, W1, W2, and W3. The key observation from this figure is that there is a link between the remaining web and stiffener thicknesses. In detail, for limited web section loss ($t_{wloss} = 30\%$) and extensive stiffener damage ($t_{sloss} > 0.7$) the capacity tends to plateau, highlighting the web's contribution. On the other hand, for increased web damage a linear relationship between the capacity and stiffener section loss is observed.

To evaluate the impact of stiffener damage height to the bearing capacity, analyses were run for corrosion height (CHs) in the range of 5% to 100% of the stiffener depth (Fig. 14.10). For the presented results, stiffener section loss equal to 50%, 30% and 40% has been considered for the patterns W1, W2 and W3, respectively. A general picture emerging from Fig. 14.10 is that the remaining section within the bottom 10% of the stiffeners depth defines the residual bearing capacity.

14.3.2.3 Effect of Web Corrosion Topology

In addition to the effect of stiffener damage, sensitivity analysis with respect to web section loss (t_{wloss}), as well as to the web corrosion length (CL) and height (CH) was conducted. Fig. 14.11 provides evidence that the relationship between capacity

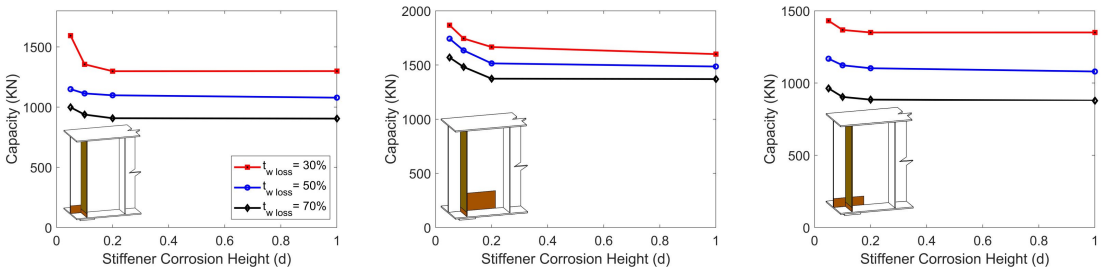

Figure 14.10: Effect of stiffener corrosion height related to a) W1, b) W2 and c) W3 patterns. The stiffeners condition at the bottom 10% is critical for the remaining bearing capacity.

and web thickness loss is related both to the stiffener condition as well as to the corrosion location and dimensions. In detail, in Fig. 14.11a the damage area within the web is limited between the end of the beam and the pair of bearing stiffeners (W1 pattern). For this case, the capacity tends to plateau for a combination of extensive web damage ($t_{wloss} > 0.5$) and limited section loss along the stiffeners ($t_{sloss} = 20\%$). This behavior highlights the load bearing contribution of stiffeners in combination with the intact web part located within the panel. However, for increasing stiffeners damage the capacity tends to linearly reduce. For the scenarios presented in Fig. 14.11b, where the web damage is exclusively located within the first panel (W2 pattern), the capacity curves plateau for web section loss higher than 40%, regardless of the stiffeners condition. For web section loss in the range of 20% to 80% the capacity reduction does not exceed the 28%. On the other hand, for the presented scenario in Fig. 14.11c where the web damage extends along both sides of the bearing stiffeners (W3 pattern), capacity drop exceeds 50% for remaining web thickness in the range of 80% to 20%. Taken all together, no clear relationship could be inferred between web section loss and remaining capacity, since it seems to be also linked with other parameters.

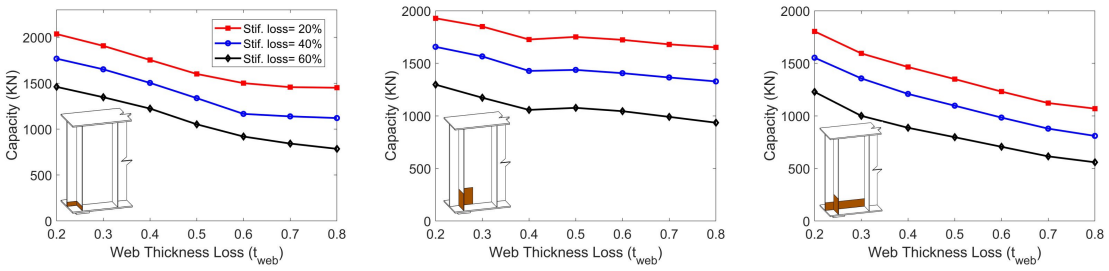

Figure 14.11: Effect of web section loss for scenarios related to a) W1, b) W2 and c) W3 patterns. In some cases, stiffeners contribution minimizes the aftermath of web section loss. The dark and light brown shades represent the minimum and maximum bounds of the examined scenarios.

Corrosion pattern W1 has been created based on the assumption of uniform section loss along the whole domain between the bearing stiffener and the web region toward the end of the beam. Consequently, in order to examine the effect of corrosion length on capacity, corrosion patterns W2 and W3 are exclusively employed. Fig. 14.12a provides strong evidence that if the corrosion length (CL) exceeds the bearing more than 10% of the web depth, it does not have any further effect on the beam's strength. In Fig. 14.12b and c the corrosion pattern which characterized by section loss along both sides of the bearing stiffeners seems to dominate the failure with the corrosion length within the panel not affecting the remaining capacity regardless of its extent. The same trends were observed for different levels of stiffener section loss.

In Fig. 14.13, the corrosion height is related to the residual capacity of beams with W1, W2 and W3 web corrosion patterns. For each case the maximum corrosion height is defined in Table 14.1. Results highlight a common characteristic of the three examined patterns, the negligible impact of damage height (CH) beyond 10% of the depth. Another finding is that, the corrosion height has reducing effect for increasing web section loss. Finally, similarly to the effect of corrosion length, the observed trends are consistent for varying stiffener section loss.

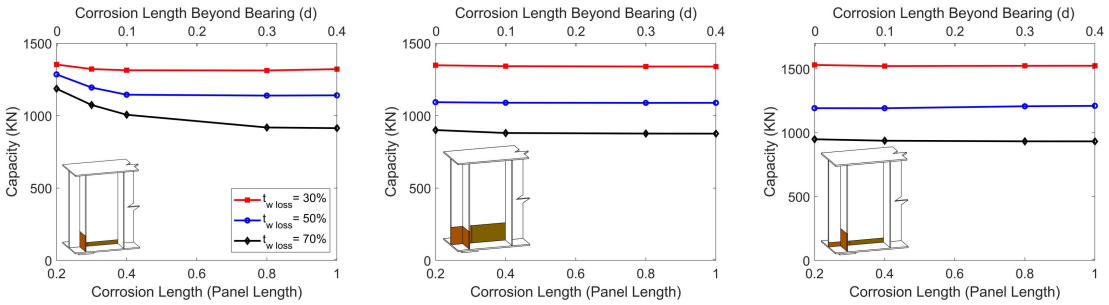

(a) (b) (c)

Figure 14.12: Effect of corrosion length for scenarios related to a) W2 and b-c) W3 patterns. The corrosion length has no effect to the bearing capacity when exceeding the bearing length more than 10% of the depth. The dark and light brown shades represent the minimum and maximum bounds of the examined scenarios.

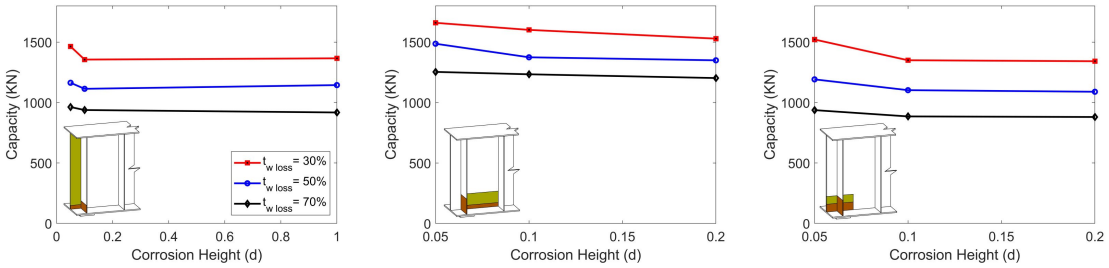

(a) (b) (c)

Figure 14.13: Effect of corrosion height for scenarios related to a) W1, b) W2 and c) W3 patterns. The corrosion height has no effect to the bearing capacity when exceeding the bearing length more than 10% of the depth. The dark and light brown shades represent the minimum and maximum bounds of the examined scenarios.

Notably, conclusions extracted from the results are representative trends for the behavior of corroded stiffened girders belonging to each one of the W1, W2, or W3 corrosion patterns. However, individual cases may deviate from this behaviour, considering that beam end corrosion is a multi-parametric problem.

CHAPTER 15

ANALYTICAL FRAMEWORK FOR CAPACITY EVALUATION

15.1 Equations Development

In this Chapter empirical equations were developed to describe the relationship between corrosion characteristics and capacities of a sample consisting of more than 1000 scenarios. The data presented in Phase III was enriched with additional scenarios in the range of variability for the general corrosion patters W1, W2 and W3, presented in Table 14.1. The simulated girder configuration on which the damage scenarios were projected on is illustrated in Fig. 14.7. The efforts are focused on beams with overhang length less than 5k, where k denotes the distance for the face of flange to web toe fillet, similar to the experimentally tested specimen for which the finite element mode was validated for. Regarding material properties, even though structural steel type with 250 MPa yield stress was mainly used for steel bridge applications up to 1970s, when the vast majority of the corroded stiffened girders in the state of Massachusetts were built, analyses have been also carried out for steel with yield stress equal to 330 MPa. To account for corrosion induced web or stiffener deviation from straightnes imperfection amplitude equal to 1 t_{web} was considered for each scenario. The finite element models were created by implementing an in house developed Python script, which operates through the ABAQUS software. For each scenario, files both for the eigenvalue as well as the quasi-static analyses were created. Python scrips have been also developed for the post processing of the results.

15.1.1 Equation Formulation

According to the load rating procedures that are currently contained in the Massachusetts Department of Transportation (MassDOT) LRFD Bridge Manual [7], the residual bearing capacity of corroded stiffened girders is calculated on the basis of the yielding capacity, as follows:

$$R_{n,yield} = \ f_y \ A_g \tag{25}$$

where f_y is the steel yield stress and A_g the gross area remaining at bearing. For beams without corrosion induced holes at the bearing, as well as with overhang length less than $5k$, where k denotes the distance from the face of flange to web toe fillet, Ag is given by the Eq. 26:

$$A_g = \ t_{rem} \ (2.5k + N) \ + \ \sum Bearing \ Stiffener \ Areas \tag{26}$$

where t_{rem} consists the corrosion input to the equation, and represents the remaining web thickness within the bottom 10 cm of the web height and length $N + 2.5k$ from the outer bearing edge, where N denotes the bearing length.

Given that the failure modes observed in Chapter 14 of the current thesis initiated with localized yielding along the damaged locations, the current procedures constitute the starting point for the development of empirical equations which capture the residual bearing failure load. Figs. 14.9 and 14.11 highlight that stiffeners section loss has a more deleterious effect compared to web section loss. Consequently, the first change modifies the assumption of the current provisions that both the web and the flange equally contribute to the residual capacity. Analytically, this is expressed by separating the contributions from the yield strength of web and stiffeners into two

two distinct terms as expressed in the following:

$$R_n = \ a\ f_y\ A_{stif}\ + b\ \ f_y\ A_{web} \tag{27}$$

where, a and b are newly introduced constants, and A_{web} and A_{stif} denote the gross section of the web and stiffeners, respectively. Another point emerging from Fig. 14.9 is the relatively linear capacity response to stiffener section loss compared to the non-linear relationship between strength and web section loss. This observation is encapsulated in Eq.

$$R_n = \ a\ f_y\ A_{stif}\ +\ b\ (f_y\ A_{web})^c \tag{28}$$

where c is a newly added constant.

15.1.2 Corrosion Input

A key observation emerging from the computational work presented in Chapter 14 was the dimensions of the damage area that significantly affect the remaining capacity of the corroded girders. In particular, a corroded area that extends beyond the 10% of the web height or beyond 10% of the bearing length does not further decrease the girder strength. To incorporate these findings, the length of the web over which the A_{web} is calculated is modified from $N + 2.5k$ to $N + 0.1d$. Furthermore, the girder's condition at the bottom 10 cm of the web is evaluated for capacity estimations. In terms of this study, the web region that is located at the bottom 10 cm and extends between the outer bearing edge and 10% beyond the bearing length is referred to as the area of interest.

Finally, the deterioration condition constitutes the last and most critical aspect for strength assessment of stiffened ends with corrosion induced damage. In detail, for the examined general web corrosion patterns, damage might be located along a

unique (W1 and W2) or both (W3) sides of the bearing stiffeners. These topologies, result in many cases to the existence of both intact as well as corroded regions within the area of interest. To facilitate the applicability of the proposed provisions, the developed equations were fitted considering as input the remaining thickness of the damage region (brown shaded areas in Fig. 14.6) within the area interest, regardless of its extent. Regarding the stiffeners condition, all the computational models were run under the assumption that both bearing stiffeners have exhibited identical and uniform section loss along their whole width. Taken all together, Eq. 28 can be rewritten as following:

$$R_n = \ a \ f_y \ A_{stif} \ + \ b \ (f_y \ t_w \ (N \ + 0.1d))^c \tag{29}$$

For the examined scenarios, A_{stif} is equal to $2t_s b_s$, where b_s denotes the stiffener width.

15.1.3 Training of the Proposed Procedures

Least squares analysis was performed to fit the computationally obtained data points to the non-linear model in Eq. 28. In this framework, the obtained capacities were set as the dependant variable, while $f_y A_{web}$ and $f_y A_{stif}$ were considered as the independent variables. Three different sets of the constants a, b, and c were derived and presented in Table 15.1 for each one of the general corrosion patterns W1, W2, and W3. Furthermore, Fig. 15.1 illustrates the predicted versus the computationally obtained capacities for the employed training sets, highlighting that for the three studied patterns the predicted capacities lie close to the solid diagonal line which represents the perfect estimation. Within the same figure, capacities obtained making use of the current procedures are also included. A general remark is that the proposed

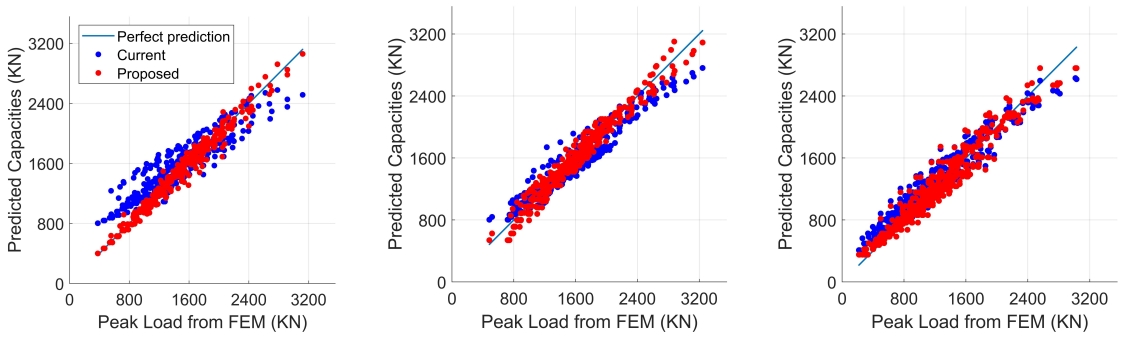

(a) (b) (c)

Figure 15.1: Comparison between the predicted and computationally obtained capacities for a) W1, b) W2 and c) W3 general corrosion patterns. The blue line represents the perfect prediction, estimations lying above this line overestimate the actual capacities.

Table 15.1: Non linear regression results for Eq. 28.

Pattern	W1	W2	W3
a	1.33	1.46	1.00
b	0.55	1.16	0.21
c	1.48	0.93	1.23

provisions significantly improve the response for the W1 general pattern, while they provide more accurate estimations for W2, and W3 patterns.

Interesting observations can be also drawn from the derived parameters values presented in Table 15.1. In detail, for the proposed provisions and the general patterns W1 and W2 where the actual web condition is analytically underestimated by considering the remaining web thickness (t_w) of the damaged area representative for the whole area of interest, the stiffeners contribution is significantly increased with a values in the range between 1.33 and 1.46. On the other hand, for the W3 pattern where the damage extends along both sides of the bearing stiffeners, t_w reflects the actual web condition and a is equal to unit.

Other equation forms were also examined but did not result in significant gains

with respect to accuracy, so the proposed equation was adopted for its simplicity and direct relationship to the parameters contributing to strength (deteriorated web and stiffeners).

15.2 Validation

To validate the efficiency of the proposed provisions, a series of numerical scenarios that have not been part of the training set were employed. In detail, for the W1 general corrosion pattern, analyses were run for 250 MPa steel and the beam configuration labeled as Geometry II in Fig. 14.7c. For the W2 pattern, the same beam configuration was used but the 330 MPa steel was preferred. Finally, for the W3 general corrosion pattern, Geometry II was combined with 250 MPa steel. The examined corrosion scenarios as well as the obtained capacities are presented in Fig. 5.1. Results highlight the efficiency of the proposed equations for the three examined corrosion patterns. It is worth noting that for most of the cases the current procedures overestimate the actual capacity. On the other hand, the developed equation provides significantly improved estimations. To quantify the predictions deviation from the actual capacities, both procedures are evaluated with the Mean Squared Error (MSE).

To quantify the predictions deviation from the actual capacities, the Mean Squared Error (MSE) was calculated for the entire range of thickness losses for each one of the general corrosion patterns. The predicted capacities according to the developed equation resulted in an 89% error reduction for patterns W1 and W3 when compared with current rating equations. For corrosion scenario W2, even though the proposed equation provided more accurate estimations for the 30% and 50% stiffener section loss, the overall MSE value was increased by 73% due to the conservative estimations for stiffener section loss equal to 70% (black lines in Fig. 15.2b).

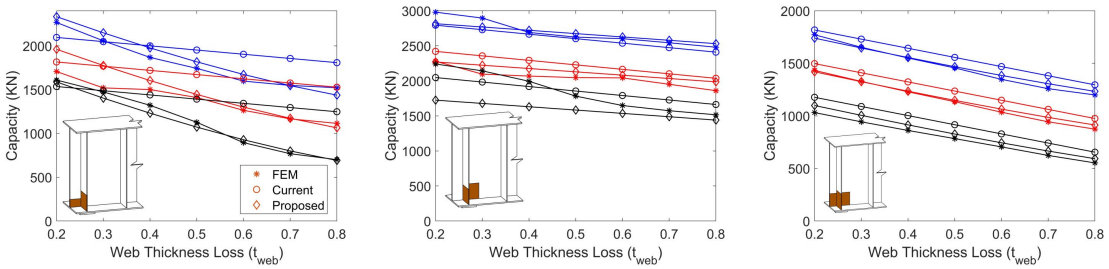

(a) (b) (c)

Figure 15.2: Comparison between predicted failure loads and numerical results for a) W1, b) W2 and c) W3 general corrosion patterns. The blue, red, and black colors denote 30%, 50%, and 70% stiffener thickness loss, respectively.

Having demonstrated the efficiency of the developed closed form equations, the conducted experiment is used to investigate, how 3D laser scanning can be implemented to define the remaining thickness value for the analytical tools. Even though Fig. 13.2c depicts thickness contour maps fitted on the thickness values of more than 80.000 points emerging from the post processing of point cloud data, both the proposed and the current analytical tools use a single value of remaining web thickness to grossly account for deterioration present at beam ends. However, given the non-uniformity of the remaining section profile, a challenge to select the suitable corrosion input rises.

Regarding the use of the proposed procedures and given that the web has experienced at least 25% section loss at both sides of the bearing stiffeners, the W3 general pattern and the associated parameters presented in Table 15.1 are selected to describe the girder's condition. By averaging the scanned data on the area of interest (10 cm by $N + 2.5k$ or 10 cm by $N + 0.1d$), the remaining thickness is equal to 9.0 mm for both provisions. Regarding material properties, the minimum experimentally obtained yield stress for each component, web or stiffeners, is used. Assigning these values in Eqs. 25 and 29, would result to capacities of 1236 kN and 802 kN for the

current and proposed procedures, respectively. However, while the current procedures overestimate the girder's strength by 24%, the proposed equation provides a conservative estimation with 20% error, not only providing credibility to the developed equation but also constitute a first sign of its robustness since it was developed for plate girders with at least twice the depth of the examined specimen.

It should be noted that for the presented calculations, bearing width equal to 10.5 cm has been assumed, neglecting the part over the flange fillet that is not in contact with the flange.

15.3 Implementation with 3D Laser Scanning

Even though the previously mentioned results demonstrate a significantly improved response of the developed procedures, researchers and engineers should be very cautious regarding 3D laser scanning implementation with analytical provisions. The work presented in Part II of this thesis revealed that averaging all the points within the area of interest may result to optimistic capacity predictions. This behavior is attributed to the fact that if a subdomain in critical condition is present within the area of interest, it can potentially define the beam ends failure. Thus, by taking into account the whole area it is possible to underrate its deleterious effect.

Nevertheless, that does not seem to be the case for the examined specimen. In particular, observation of the remaining thickness profile within the area of interest (Fig. 13.2) indicates that maximum section loss is observed at the right side of the bearing stiffener. However, the failure mode was governed by large displacements developed at the outer part of the web, following the pre-loading web deviation from straightness at that location. These observations provide strong evidence that the significantly overestimating prediction obtained by the current provisions does not emerge from the remaining thickness input but is in compliance with the overall

overestimating tendency noticed in Fig. 15.1.

In short, the current experiment provides additional data to the argument that the critical feature of a corroded end defines its failure mode and load. Consequently, engineering judgement is always a requirement for the equations implementation regardless of the employed equipment for the remaining thickness estimation.

CHAPTER 16

SUMMARY, CONCLUSIONS AND FUTURE WORK: PART III

16.1 Summary and Concluding Remarks

The prime interest of this thesis was to provide tools for corrosion quantification and mapping, as well as to shed light on the deleterious effect of corrosion-induced damage to the structural integrity of steel girder bridges. The third part of the dissertation delved into the correlation between the corrosion characteristics of deteriorated plate girders and their remaining capacity. In view of this, a full scale experimental testing was conducted on a naturally corroded girder, obtained from a bridge demolition project. The experimentally obtained data was combined with data from the literature to develop and validate a finite element mode able to capture the failure mode and load of composite plate girders with end damage. Having provided credibility to the finite element model an extensive parametric analysis was conducted to study the effect of numerous deterioration parameters to the residual bearing capacity. The corrosion induced damage was portrayed as uniform section loss along the web and the bearing stiffeners. Finally, simplified closed form equations were developed to analytically express the previously found observation.

- The failure mode of the tested girder was governed by the corrosion condition of both web (the initial web deviation from straightness and section loss profile) and stiffeners (uniformly reduced thickness).

- Comparison of experimentally and numerically obtained results provided credibility to the developed finite element model with the failure load being captured

with 3% error. The corrosion condition of the web was integrated to the model based on post-processed point cloud data, highlighting that 3D scanning can be used to better define the corrosion field.

- Results emerging from the sensitivity analysis revealed that the beam end capacity is influenced linearly and non-linearly by stiffener and web strength, respectively. On the other hand, if corrosion induced damage extends above the 10% of the beam's depth and beyond 10% far from the bearing, it does not significantly affect the remaining bearing capacity.

- Prediction tools were developed for three general corrosion patterns, defined from studying MassDOT inspection reports of structurally deficient bridges. Numerical evaluation of the developed closed form equations resulted to 89% reduced mean squared error, compared to the current procedures, for the two out of the three general corrosion patterns. For the third case, the mean square error MSE was increased by 70% due to the conservative estimations for a small part of the test set. Finally, applying both the current and the proposed provisions to the tested specimen resulted to error +24% and -20%, respectively, highlighting the improved efficiency of the developed equations.

16.2 Outlook and Future Work

The findings of this study aspire to stimulate and intensify further research on the field of aging bridges evaluation, setting new and broad objectives for future projects. Even though the proposed provisions proved significantly more efficient compared to the current procedures, there were not designed to modify the method of hole inclusion in the methodology currently found in the MassDOT Bridge Manual[7]. A future extension of the current study should analytically address this limitation and

further increase the impact of the developed closed form equations to stiffened beam ends with corrosion induced holes above the support.

Towards the development of the proposed closed form equations, a four-step methodology involving the following aspects was presented: Experimental testing of naturally corroded specimens, validation of a computational model, parametric analysis, and, finally, analytical tools developed to fit in computationally obtained capacities. It is worth noting, that the developed workflow is not tied to steel girder bridges, consequently the same approach can be applied to other bridge types to address the decaying effect of deterioration.

Overall, the current dissertation focused on the evaluation of girders with corrosion induced-damage. In case the estimated residual load carrying capacities do not serve the traffic requirements or the bridge condition threatens the public safety, repairs are needed. Conventional repair methods locally address deficiencies by welding new steel plates at the corroded regions. However, this approach is combined with extensive labor, and costs. Novel innovative methods deem as the next step towards more efficient standard procedures to repair corroded steel girder ends.

REFERENCES

[1] G. Tzortzinis, B. T. Knickle, A. Bardow, S. F. Breña, S. Gerasimidis, Strength evaluation of deteriorated girder ends. i: Experimental study on naturally corroded i-beams, Thin-Walled Struct. 159 (2021) 107220. doi:https://doi.org/10.1016/j.tws.2020.107220.

[2] G. Tzortzinis, B. T. Knickle, A. Bardow, S. F. Breña, S. Gerasimidis, Strength evaluation of deteriorated girder ends. ii: Numerical study on corroded i-beams, Thin-Walled Structures 159 (2021) 107216. doi:https://doi.org/10.1016/j.tws.2020.107216.

[3] G. Tzortzinis, C. Ai, S. F. Breña, S. Gerasimidis, Using 3d laser scanning for estimating the capacity of corroded steel bridge girders: Experiments, computations and analytical solutions, (under Review).

[4] G. Tzortzinis, S. F. Breña, S. Gerasimidis, Experimental testing, computational analysis and analytical formulation for the remaining capacity assessment of bridge plate girders with naturally corroded ends, Under Review.

[5] J. M. Kulicki, Z. Prucz, D. F. Sorgenfrei, D. R. Mertz, W. T. Young, Guidelines for evaluating corrosion effects in existing steel bridges, 1990.

[6] E. M. Javier, Methods for evaluation of the remaining strength in steel bridge beams with section losses due to corrosion damage, Master's thesis, Virginia Tech (2021).

[7] MassDOT, Draft LRFD Bridge Manual Part I, Boston, MA (2019).

[8] P. H. Mans, Full scale testing of composite plate girders constructed using 70-ksi high performance steel, Master's thesis, University of Nebraska (2001).

[9] C. Seim, Why bridges have failed throughout history, Civil Engineering Magazine 78 (2008). doi:https://doi.org/10.1061/ciegag.0000172.

[10] NTSB, Collapse of a suspended span of inter- state route 95 highway bridge over the mianus river, Tech. rep., National Transportation Safety Bord, Washington, DC (1984).

[11] J.-H. Ahn, S. Kainuma, I.-T. Kim, Shear failure behaviors of a web panel with local corrosion depending on web boundary conditions, Thin-Walled Structures 73 (2013) 302–317.

[12] F. Mars G, Corrosion Engineering, McGraw-Hill Book Company, 1987.

[13] MassDOT, Bridge inspection handbook, The Massachusetts Department of Transportation Highway Division Bridge Section (2015).

[14] ASCE, Infrastructure report card (2021).
URL https://www.infrastructurereportcard.org/

[15] G. Tzortzinis, B. Knickle, S. Gerasimidis, A. Bardow, S. Breña, Experiments and computations on steel bridge corroded beam ends, in: Proceedings of the Annual Stability Conference, St. Louis, Missouri, Structural Stability Research Council, 2019.

[16] G. Tzortzinis, S. Gerasimidis, S. F. Breña, B. Knickle, Development of load rating procedures for deteriorated steel beam ends: Deliverable 4, Tech. Report 19-008, MassDOT (2019).

[17] T. Roberts, Slender plate girders subjected to edge loading, Proc Inst Civ Eng 71 (2) (1981) 805–819.

[18] J. R. Kayser, A. S. Nowak, Capacity loss due to corrosion in steel-girder bridges, J. Struct. Eng. 115 (6) (1989) 1525–1537. doi:https://doi.org/10.1061/(ASCE)0733-9445(1989)115:6(1525).

[19] J. W. van de Lindt, M. Ahlborn Theresa, Development of steel beam end deterioration guidelines, Tech. rep., MDOT Research Report RC-1454 (2005).

[20] I. Sugimoto, Y. Kobayashi, A. Ichikawa, Durability evaluation based on buckling characteristics of corroded steel deck girders, Quarterly Report of RTRI 47 (3) (2006) 150–155.

[21] S. Tohidi, Y. Sharifi, Load-carrying capacity of locally corroded steel plate girder ends using artificial neural network, Thin-Walled Structures 100 (2016) 48–61.

[22] J.-H. Ahn, S. Kainuma, F. Yasuo, I. Takehiro, Repair method and residual bearing strength evaluation of a locally corroded plate girder at support, Engineering Failure Analysis 33 (2013) 398–418. doi:https://doi.org/10.1016/j.engfailanal.2013.06.015.

[23] T. Miyashita, M. Nagai, D. Wakabayashi, Y. Hidekuma, A. Kobayashi, Y. Okuyama, N. Koide, W. Horimoto, Repair method for corroded steel girder ends using cfrp sheet, in: IABSE-JSCE Joint Conference on Advances in Bridge Engineering-III, 2015, pp. 21–22.

[24] H. Ogami, K. Fujii, T. Yamada, H. Iwashaki, Renovation of corroded girder end in plate girder bridge with resin and rebars, Implementing innovative ideas in structural engineering and project management (2015) 1–6.

[25] B. Wu, J.-L. Cao, L. Kang, Influence of local corrosion on behavior of steel i-beams subjected to end patch loading: Experiments, Journal of Constructional Steel Research 135 (2017) 150–161. doi:https://doi.org/10.1016/j.jcsr.2017.04.020.

[26] B. Wu, J.-L. Cao, L. Kang, End patch loading behavior and strengthening of locally corroded steel i-beams, Journal of Constructional Steel Research 148 (2018) 371–382. doi:https://doi.org/10.1016/j.jcsr.2018.05.029.

[27] K. M. Zmetra, K. F. McMullen, A. E. Zaghi, K. Wille, Experimental study of uhpc repair for corrosion-damaged steel girder ends, Journal of Bridge Engineering 22 (8) (2017) 04017037. doi:https://doi.org/10.1061/(ASCE)BE.1943-5592.0001067.

[28] D. Kruszewski, K. Wille, A. E. Zaghi, Design considerations for headed shear studs embedded in ultra-high performance concrete as part of a novel bridge repair method, Journal of Constructional Steel Research 149 (2018) 180–194. doi:https://doi.org/10.1016/j.jcsr.2018.07.015.

[29] D. Kruszewski, K. Wille, A. E. Zaghi, Push-out behavior of headed shear studs welded on thin plates and embedded in uhpc, Engineering Structures 173 (2018) 429–441. doi:https://doi.org/10.1016/j.engstruct.2018.07.013.

[30] D. Kruszewski, A. E. Zaghi, K. Wille, Durability evaluation of headed shear studs embedded in ultrahigh-performance concrete via electrochemical corrosion, Journal of Bridge Engineering 24 (5) (2019). doi:https://doi.org/10.1061/(ASCE)BE.1943-5592.0001401.

[31] PocketMIKE, Operating Manual, GE Inspection Technologies, Lewistown, PA (2004).

[32] ASTM, Standard test methods for tension testing of metallic materials, ASTM International, West Conshohocken, PA (2011).

[33] SIMULIA, Providence, RI, Abaqus user's manual (2014).

[34] W. M. Haynes (Ed.), CRC handbook of chemistry and physics., CRC press, 2014.

[35] G. Tzortzinis, B. Knickle, S. Gerasimidis, A. Bardow, S. Breña, Identification of most common shapes and locations for beam end corrosion of steel girder bridges, in: Proc., 98th Annual Meeting of the Transportation Research Board, 2019.

[36] M. Elgaaly, R. Salkar, Web crippling under edge loading, in: Proceedings of AISC National Steel Construction Conference, 1991.

[37] M. Rashidi, M. Mohammadi, S. Sadeghlou Kivi, M. M. Abdolvand, L. Truong-Hong, B. Samali, A decade of modern bridge monitoring using terrestrial laser scanning: Review and future directions, Remote Sensing 12 (22) (2020). doi:10.3390/rs12223796.

[38] S. Abu Dabous, S. Feroz, Condition monitoring of bridges with non-contact testing technologies, Automation in Construction 116 (2020) 103224. doi:https://doi.org/10.1016/j.autcon.2020.103224.

[39] C.-Z. Dong, F. N. Catbas, A review of computer vision–based structural health monitoring at local and global levels, Structural Health Monitoring 0 (0) (2020) 1475921720935585. arXiv:https://doi.org/10.1177/1475921720935585, doi:10.1177/1475921720935585.

[40] Q. Jiang, S. Zhong, P.-Z. Pan, Y. Shi, H. Guo, Y. Kou, Observe the temporal evolution of deep tunnel's 3d deformation by 3d laser scanning in the jinchuan

no. 2 mine, Tunnelling and Underground Space Technology 97 (2020) 103237. doi:https://doi.org/10.1016/j.tust.2019.103237.

[41] Q. Hou, C. Ai, A network-level sidewalk inventory method using mobile lidar and deep learning, Transportation Research Part C: Emerging Technologies 119 (2020) 102772. doi:https://doi.org/10.1016/j.trc.2020.102772.

[42] H.-M. Zogg, H. Ingensand, Terrestrial laser scanning for deformation monitoring. load tests on the felsenau viaduct (ch), in: In Proceedings of the The International Archives of the Photogrammetry, Remote Sensing and Spatial Information Sciences, Beijing, China, Vol. XXXVII, ISPRS, 2008, pp. 555 – 562. doi:10.3929/ethz-b-000011210.

[43] H. Yang, X. Xu, I. Neumann, The benefit of 3d laser scanning technology in the generation and calibration of fem models for health assessment of concrete structures, Sensors 14 (11) (2014) 21889–21904. doi:10.3390/s141121889.

[44] H. S. Park, H. M. Lee, H. Adeli, I. Lee, A new approach for health monitoring of structures: Terrestrial laser scanning, Computer-Aided Civil and Infrastructure Engineering 22 (1) (2007) 19–30. arXiv:https://onlinelibrary.wiley.com/doi/pdf/10.1111/j.1467-8667.2006.00466.x, doi:https://doi.org/10.1111/j.1467-8667.2006.00466.x.

[45] M. Miśkiewicz, D. Bruski, J. Chróścielewski, K. Wilde, Safety assessment of a concrete viaduct damaged by vehicle impact and an evaluation of the repair, Engineering Failure Analysis 106 (2019) 104147. doi:https://doi.org/10.1016/j.engfailanal.2019.104147.

[46] B. Riveiro, H. González-Jorge, M. Varela, D. Jauregui, Validation of terrestrial laser scanning and photogrammetry techniques for the measurement of vertical

underclearance and beam geometry in structural inspection of bridges, Measurement 46 (1) (2013) 784–794. doi:https://doi.org/10.1016/j.measurement.2012.09.018.

[47] R. J. Ross, B. K. Brashaw, S. J. Anderson, Use of laser scanning technology to obtain as-built records of historic covered bridges, USDA Forest Service, Forest Products Laboratory, Report Paper, FPL-RP-669, 2012; 21 p. 669 (2012) 1–21.

[48] I. Lubowiecka, J. Armesto, P. Arias, H. Lorenzo, Historic bridge modelling using laser scanning, ground penetrating radar and finite element methods in the context of structural dynamics, Engineering Structures 31 (11) (2009) 2667–2676. doi:https://doi.org/10.1016/j.engstruct.2009.06.018.

[49] M. Minehane, R. O'Donovan, K. Ruane, B. O'Keeffe, The use of 3d laser scanning technology for bridge inspection and assessment, Structural Health Monitoring (SHM) 13 (2014) 14.

[50] B. Conde-Carnero, B. Riveiro, P. Arias, J. C. Caamaño, Exploitation of geometric data provided by laser scanning to create fem structural models of bridges, Journal of Performance of Constructed Facilities 30 (3) (2016) 04015053. doi:10.1061/(ASCE)CF.1943-5509.0000807.

[51] N. Gyetvai, L. Truong-Hong, D. F. Laefer, Laser scan-based structural assessment of wrought iron bridges: Guinness bridge, ireland, Proceedings of the Institution of Civil Engineers-Engineering History and Heritage 171 (2) (2018) 76–89.

[52] A. Bautista-De Castro, L. J. Sánchez-Aparicio, L. F. Ramos, J. Sena-Cruz, D. González-Aguilera, Integrating geomatic approaches, operational modal analysis, advanced numerical and updating methods to evaluate the current safety conditions of the historical bôco bridge, Construction and Building Materials

158 (2018) 961–984. doi:https://doi.org/10.1016/j.conbuildmat.2017.10.084.

[53] L. Truong-Hong, H. Falter, D. Lennon, D. F. Laefer, Framework for bridge inspection with laser scanning, in: in Proceedings of the EASEC-14 Structural Engineering and Construction, Ho Chi Minh City, Vietnam, 2016.

[54] J. Valença, I. Puente, E. Júlio, H. González-Jorge, P. Arias-Sánchez, Assessment of cracks on concrete bridges using image processing supported by laser scanning survey, Construction and Building Materials 146 (2017) 668–678. doi:https://doi.org/10.1016/j.conbuildmat.2017.04.096.

[55] G. Teza, A. Galgaro, F. Moro, Contactless recognition of concrete surface damage from laser scanning and curvature computation, NDT & E International 42 (4) (2009) 240–249. doi:https://doi.org/10.1016/j.ndteint.2008.10.009.

[56] M.-K. Kim, H. Sohn, C.-C. Chang, Localization and quantification of concrete spalling defects using terrestrial laser scanning, Journal of Computing in Civil Engineering 29 (6) (2015) 04014086. doi:10.1061/(ASCE)CP.1943-5487.0000415.

[57] H.-K. Shen, P.-H. Chen, L.-M. Chang, Automated steel bridge coating rust defect recognition method based on color and texture feature, Automation in Construction 31 (2013) 338–356. doi:https://doi.org/10.1016/j.autcon.2012.11.003.

[58] S. K. P. Kushwaha, S. Raghavendra, H. Pande, S. Agrawal, Analysis and integration of surface and subsurface information of different bridges, Journal of the Indian Society of Remote Sensing 48 (2) (2020) 315–331.

[59] A. Hain, A. E. Zaghi, A. Kamali, R. P. Zaffetti, B. Overturf, F. E. Pereira, Applicability of 3-d scanning technology for section loss assessment in corroded steel beams, Transportation Research Record 2673 (3) (2019) 271–280. doi:10.1177/0361198119832887.

[60] AASHTO, AASHTO LRFD bridge design specifications, American Association of State Highway and Transportation Officials, Washington, D.C (2012).

[61] Riegl, Riegl VZ-2000 brochure (2020).

[62] CloudCompare, CloudCompare Version 2.6. 1 User Manual (2019).

[63] I.-T. Kim, M.-J. Lee, J.-H. Ahn, S. Kainuma, Experimental evaluation of shear buckling behaviors and strength of locally corroded web, Journal of Constructional Steel Research 83 (2013) 75–89. doi:https://doi.org/10.1016/j.jcsr.2012.12.015.

[64] J.-H. Ahn, J.-H. Cheung, W.-H. Lee, H. Oh, I.-T. Kim, Shear buckling experiments of web panel with pitting and through-thickness corrosion damage, Journal of Constructional Steel Research 115 (2015) 290–302. doi:https://doi.org/10.1016/j.jcsr.2015.08.032.

[65] J.-H. Ahn, I.-T. Kim, S. Kainuma, M.-J. Lee, Residual shear strength of steel plate girder due to web local corrosion, Journal of Constructional Steel Research 89 (2013) 198–212.

[66] N. Khurram, E. Sasaki, H. Katsuchi, H. Yamada, Experimental and numerical evaluation of bearing capacity of steel plate girder affected by end panel corrosion, International Journal of Steel Structures 14 (3) (2014) 659–676. doi:http://dx.doi.org/10.1007/s13296-015-3018-0.

[67] M. Usukura, T. Yamaguchi, Y. Suzuki, Y. Mitsugi, Strength evaluation for a corroded damaged steel girder end considering its collapse mechanism, in: Proceedings of the Thirteenth East Asia-Pacific Conference on Structural Engineering and Construction (EASEC-13), The Thirteenth East Asia-Pacific Conference on Structural Engineering and ..., 2013, pp. D–2.

[68] C. Liu, T. Miyashita, M. Nagai, Analytical study on shear capacity of steel i-girders with local corrosion nearby supports, Procedia engineering 14 (2011) 2276–2284.

[69] E. Yamaguchi, T. Akagi, Degradation of load-carrying capacity of steel i-girder end due to corrosion, in: Proceedings of the Thirteenth East Asia-Pacific Conference on Structural Engineering and Construction (EASEC-13), The Thirteenth East Asia-Pacific Conference on Structural Engineering and ..., 2013, pp. D–2.

[70] K. E. Barth, H. Wu, Efficient nonlinear finite element modeling of slab on steel stringer bridges, Finite Elements in Analysis and Design 42 (14) (2006) 1304–1313. doi:https://doi.org/10.1016/j.finel.2006.06.004.

[71] AASHTO, Standard Specifications for Highway Bridges, American Association of State Highway and Transportation Officials (1973).